

Advances in Meteorology

Climate Modeling for Renewable Energy Applications

Guest Editors: Huei-Ping Huang, Brent C. Hedquist, Taewoo Lee,
and Soe W. Myint





Climate Modeling for Renewable Energy Applications

Advances in Meteorology

Climate Modeling for Renewable Energy Applications

Guest Editors: Huei-Ping Huang, Brent C. Hedquist,
Taewoo Lee, and Soe W. Myint



Copyright © 2014 Hindawi Publishing Corporation. All rights reserved.

This is a special issue published in “Advances in Meteorology.” All articles are open access articles distributed under the Creative Commons Attribution License, which permits unrestricted use, distribution, and reproduction in any medium, provided the original work is properly cited.

Editorial Board

P. Artaxo, Brazil
Guy Brasseur, USA
Mladjen Ćurić, Serbia
Raymond Desjardins, Canada
Klaus Dethloff, Germany
Panuganti C. S. Devara, India
Julio Diaz, Spain
Luis Gimeno, Spain

Sven-Erik Gryning, Denmark
Ismail Gultepe, Canada
Hiroyuki Hashiguchi, Japan
Didier Hauglustaine, France
Ivar S A Isaksen, Norway
Yasunobu Iwasaka, Japan
Charles Jones, USA
Hann-Ming H. Juang, USA

George Kallos, Greece
Harry D. Kambezidis, Greece
Richard Leitch, Canada
Monique Leclerc, USA
Gwo-Fong Lin, Taiwan
Kyaw T. Paw, USA
Jorge Pey, France
Sara C. Pryor, USA

Contents

Climate Modeling for Renewable Energy Applications, Huei-Ping Huang, Brent C. Hedquist, Taewoo Lee, and Soe W. Myint

Volume 2014, Article ID 354862, 2 pages

Changes in Surface Wind Speed over North America from CMIP5 Model Projections and Implications for Wind Energy, Sujay Kulkarni and Huei-Ping Huang

Volume 2014, Article ID 292768, 10 pages

Generalized Scaling of Urban Heat Island Effect and Its Applications for Energy Consumption and Renewable Energy, T.-W. Lee, Heung S. Choi, and Jinoh Lee

Volume 2014, Article ID 948306, 5 pages

Climate Change Impact on Photovoltaic Energy Output: The Case of Greece, Ioanna S. Panagea, Ioannis K. Tsanis, Aristeidis G. Koutroulis, and Manolis G. Grillakis

Volume 2014, Article ID 264506, 11 pages

WRF Model Methodology for Offshore Wind Energy Applications,

Evangelia-Maria Giannakopoulou and Regis Nhili

Volume 2014, Article ID 319819, 14 pages

A Subgrid Parameterization for Wind Turbines in Weather Prediction Models with an Application to Wind Resource Limits, B. H. Fiedler and A. S. Adams

Volume 2014, Article ID 696202, 6 pages

Editorial

Climate Modeling for Renewable Energy Applications

Huei-Ping Huang,¹ Brent C. Hedquist,² Taewoo Lee,¹ and Soe W. Myint³

¹*School for Engineering of Matter, Transport, and Energy, Arizona State University, Tempe, AZ 85281, USA*

²*Department of Physics and Geosciences, Texas A&M University-Kingsville, Kingsville, TX 78363, USA*

³*School of Geographical Sciences and Urban Planning, Arizona State University, Tempe, AZ 85281, USA*

Correspondence should be addressed to Huei-Ping Huang; hp.huang@asu.edu

Received 27 November 2014; Accepted 27 November 2014; Published 22 December 2014

Copyright © 2014 Huei-Ping Huang et al. This is an open access article distributed under the Creative Commons Attribution License, which permits unrestricted use, distribution, and reproduction in any medium, provided the original work is properly cited.

The exploration of environmentally friendly energy resources is one of the major challenges facing society today. The last decade has witnessed rapid developments in renewable energy engineering. Wind and solar power plants with increasing sizes and technological sophistication have been built. Amid this development, meteorological modeling plays an increasingly important role, not only in selecting the sites of wind and solar power plants but also in assessing the environmental impacts of those plants. The permanent land-use changes as a result of the construction of wind farms can potentially alter local climate (Keith et al. [1], Roy and Traiteur [2]). The reduction of wind speed by the presence of wind turbines could affect the preconstruction estimate of wind power potential (e.g., Adams and Keith [3]). Future anthropogenic greenhouse gas emissions are expected to induce changes in the surface wind and cloudiness, which would affect the power production of wind and solar power plants. To quantify these two-way relations between renewable energy production and regional climate change, mesoscale meteorological modeling remains one of the most efficient approaches for research and applications.

The construction of large-scale wind or solar power plants will change the physical properties of the surface such as surface roughness, albedo, and emissivity for longwave radiation. Wind turbines are momentum sinks for the atmospheric flow in the boundary layer. The physical basis for incorporating these processes in an atmospheric model is clear. Nevertheless, individual wind turbines, or even a wind farm as a whole, could be too small for a typical weather or climate model to resolve. A parameterization scheme for the subgrid-scale effect of wind farms on the velocity field is much needed

and has been actively developed. For example, a scheme developed by Fitch et al. [4] has recently been incorporated into the widely used weather research and forecasting (WRF) model (Skamarock et al. [5]). The scheme is formulated as an extension of the boundary layer parameterization scheme which is already implemented in many weather and climate models. The environmental impacts of wind farms and solar power plants can also be treated using the schemes for modeling the effects of land-use and land-cover changes. Such schemes have been actively developed especially in the form of urban canopy models (e.g., Kusaka et al. [6]). For example, if solar panels are classified as a distinctive surface type with specific surface albedo and emissivity, their effects can be calculated by using an existing urban parameterization scheme given the fractional area coverage of a solar power plant over a grid box of the model. Thus, the development of the parameterization schemes for the effects of wind and solar power plants is not an isolated activity but constitutes part of the important trend of incorporating multiscale physical processes into the framework of environmental prediction.

The large-scale jet streams in the global atmosphere that provide the reservoir of wind energy are projected to change on multidecadal and longer time scales under the influence of anthropogenic greenhouse gas emissions (e.g., Yin [7]). The shifts of jet streams and the accompanying changes in regional weather patterns (e.g., Seager et al. [8]) can lead to an increase or decrease of local cloud cover, thereby affecting the gain of solar power plants. Those large-scale climate changes have been systematically projected using global climate models with relatively coarse spatial resolutions (Taylor et al. [9]). Extensive efforts are underway to “downscale” the climate

information obtained by the global model to regional and urban scales. Nevertheless, only a few of the existing studies used the approach of climate downscaling to project the local changes in wind or solar power potential (e.g., Ren [10], Pryor and Barthelmie [11]). Progresses in this direction will not only help refine the estimate of global and regional wind and solar power potential but also aid the siting of wind and solar power plants, based on the premise that an optimal site today may not be optimal in one or two decades.

Climate modeling for renewable energy applications is an exciting emerging research topic for both climate scientists and renewable energy engineers. We conclude by suggesting the following four particularly promising directions for future research towards climate and energy applications: (1) further developments of the techniques for multiscale climate downscaling to transfer climate information from global to urban and wind-farm scales, (2) quantification of the mechanical and thermodynamic effects of wind or solar power plants on the microscale atmospheric environment and climate, (3) further developments of parameterization schemes for the subgrid-scale effects of wind and solar power plants in regional and global climate models, and (4) systematic classifications of wind farms and solar power plants as distinctive surface types for research of the impacts of land-use and land-cover changes on local climate.

Huei-Ping Huang
Brent C. Hedquist
Taewoo Lee
Soe W. Myint

References

- [1] D. W. Keith, J. F. DeCarolis, D. C. Denkenberger et al., "The influence of large-scale wind power on global climate," *Proceedings of the National Academy of Sciences of the United States of America*, vol. 101, no. 46, pp. 16115–16120, 2004.
- [2] S. B. Roy and J. J. Traiteur, "Impacts of wind farms on surface air temperatures," *Proceedings of the National Academy of Sciences of the United States of America*, vol. 107, no. 42, pp. 17899–17904, 2010.
- [3] A. S. Adams and D. W. Keith, "Are global wind power resource estimates overstated?" *Environmental Research Letters*, vol. 8, no. 1, Article ID 015021, 2013.
- [4] A. C. Fitch, J. B. Olson, J. K. Lundquist et al., "Local and mesoscale impacts of wind farms as parameterized in a meso-scale NWP model," *Monthly Weather Review*, vol. 140, no. 9, pp. 3017–3038, 2012.
- [5] W. C. Skamarock, J. B. Klemp, J. Dudhia et al., "A description of the advanced research WRF version 3," NCAR Technical Note NCAR/TN-475+STR, Boulder, Colo, USA, 2008.
- [6] H. Kusaka, H. Kondo, Y. Kikegawa, and F. Kimura, "A simple single-layer urban canopy model for atmospheric models: comparison with multi-layer and slab models," *Boundary-Layer Meteorology*, vol. 101, no. 3, pp. 329–358, 2001.
- [7] J. H. Yin, "A consistent poleward shift of the storm tracks in simulations of 21st century climate," *Geophysical Research Letters*, vol. 32, no. 18, article 28, 2005.
- [8] R. Seager, M. Ting, I. Held et al., "Model projections of an imminent transition to a more arid climate in southwestern North America," *Science*, vol. 316, no. 5828, pp. 1181–1184, 2007.
- [9] K. E. Taylor, R. J. Stouffer, and G. A. Meehl, "An overview of CMIP5 and the experiment design," *Bulletin of the American Meteorological Society*, vol. 93, no. 4, pp. 485–498, 2012.
- [10] D. Ren, "Effects of global warming on wind energy availability," *Journal of Renewable and Sustainable Energy*, vol. 2, no. 5, Article ID 052301, 2010.
- [11] S. C. Pryor and R. J. Barthelmie, "Assessing climate change impacts on the near-term stability of the wind energy resource over the United States," *Proceedings of the National Academy of Sciences of the United States of America*, vol. 108, no. 20, pp. 8167–8171, 2011.

Research Article

Changes in Surface Wind Speed over North America from CMIP5 Model Projections and Implications for Wind Energy

Sujay Kulkarni and Huei-Ping Huang

School for Engineering of Matter, Transport, and Energy, Arizona State University, Tempe, AZ 85281, USA

Correspondence should be addressed to Sujay Kulkarni; sskulka8@asu.edu

Received 14 March 2014; Accepted 12 August 2014; Published 1 September 2014

Academic Editor: Taewoo Lee

Copyright © 2014 S. Kulkarni and H.-P. Huang. This is an open access article distributed under the Creative Commons Attribution License, which permits unrestricted use, distribution, and reproduction in any medium, provided the original work is properly cited.

The centennial trends in the surface wind speed over North America are deduced from global climate model simulations in the Climate Model Intercomparison Project—Phase 5 (CMIP5) archive. Using the 21st century simulations under the RCP 8.5 scenario of greenhouse gas emissions, 5–10 percent increases per century in the 10 m wind speed are found over Central and East-Central United States, the Californian Coast, and the South and East Coasts of the USA in winter. In summer, climate models projected decreases in the wind speed ranging from 5 to 10 percent per century over the same coastal regions. These projected changes in the surface wind speed are moderate and imply that the current estimate of wind power potential for North America based on present-day climatology will not be significantly changed by the greenhouse gas forcing in the coming decades.

1. Introduction

The rapid technological developments in the past decade have established wind energy as one of the major alternatives to fossil-fuel based energy. The potential of wind power generation in the United States alone, including off-shore and on-shore capacity, is estimated to be about 15000 GW (e.g., Lopez et al. [1]). This estimate generally does not take into account future climate changes which may alter the pattern and strength of near-surface wind at desirable locations for wind farms (Freedman et al. [2], Ren [3]). Worldwide, long-term projections of decadal-to-centennial climate changes due to anthropogenic emission of greenhouse gases (GHG) have been systematically carried out by climate modeling groups that participate in the Climate Model Intercomparison Project-Phase 5 (CMIP5, Taylor et al. [4], cmip5-pcmdi.llnl.gov/cmip5), in close association with the Intergovernmental Panel on Climate Change (IPCC) of the United Nations (IPCC [5]). While climate model outputs from CMIP5 and its predecessors have been widely used to project regional changes in temperature and hydrological cycles (e.g., Seager et al. [6], Baker and Huang [7]), few studies have used the datasets to project future changes in surface wind. Notably, Pryor and Barthelmie [8] analyzed the regional

model simulations in NARCAAP (Mearns et al. [9]), constrained by the global model projections from CMIP3 (Meehl et al. [10]), to conclude that GHG-induced climate change will not significantly affect wind power potential in the United States in the coming decades. As a contribution to this underexplored area of research, this study will use a subset of the newer CMIP5 model data to construct the GHG-induced trends in the near-surface wind speed over North America.

The horizontal resolution of the global climate models in CMIP5 is typically around 100–150 km in midlatitudes. It is understood that this is not fine enough to resolve detailed topography in the mesoscale and submesoscale, which can have nontrivial influences on the low-level wind field. Nevertheless, the information from the global models provide the first-order picture of the changes in the large-scale flow, which will form the basis for future efforts to downscale the global model output to regional and urban scales. The CMIP5 simulations for the 21st Century are driven by the radiative forcing deduced from different scenarios of anthropogenic emissions of GHG and industrial aerosols. Regional climate changes due to land-use changes (e.g., urbanization) or even the influence of large-scale wind farms (e.g., Keith et al. [11] and Adams and Keith [12]) are not covered by the 21st century scenarios in CMIP5 and are not considered in this work.

TABLE 1: List of the CMIP5 models used in this study.

Model	Institution	Resolution
EC-Earth	EC-Earth consortium (multiple)	$320 \times 160/T159$ (L62)
IPSL-CM5-LR	Institut Pierre-Simon Laplace (France)	96×96 (L39)
GISS-E2-H	NASA Goddard Institute for Space Studies (USA)	144×90 (L40)
CSIRO-MK 3.6.0	Commonwealth Scientific and Industrial Research Organisation (CSIRO) and Queensland Climate Change Centre of Excellence (Australia)	$192 \times 96/T63$ (L31)
ACCESS 1.0	CSIRO and Bureau of Meteorology (Australia)	192×145 (L38)

2. Datasets

Five models, from CMIP5, EC-Earth, IPSL-CM5-LR, GISS-E2-H, CSIRO-MK 3.6.0, and ACCESS 1.0 (listed in Table 1), are used in this study. By first examining the scatter plots of the indices of large-scale wind fields (in the manner of Paek and Huang [13]) over the Pacific-North American sector, the five models were selected as a subset that at least reflects the diversity (in terms of model resolution and biases) of the over 30 models in CMIP5. For example, IPSL-CM5-LR and GISS-E2-H substantially underestimate and CSIRO-MK 3.6.0 overestimates the Low Level Jet over North America, while the other two models produce only small biases in that feature (not shown). For our purpose of deducing trends, the historical runs for the 20th Century and the corresponding 21st century runs under the representative concentration pathways (RCP) 8.5 scenario are used. As a brief background, the RCP8.5 scenario imposes 8.5 W/m^2 of radiative forcing, induced by the projected increase in GHG concentration, to the atmosphere towards the end of the 21st Century. It produces an increase in global mean surface air temperature which ranges from $+2.6$ to $+4.8^\circ\text{C}$ over the 21st Century from the projections by the majority of CMIP5 models (IPCC [5]).

The global models in CMIP5 typically have very few vertical levels within the planetary boundary layer. Given that wind turbines are usually at 80–100 m height, at which there is no direct model output, the closest standard output variables that we can use from CMIP5 are the surface wind speed and the vector wind field at 10 m height as calculated from boundary layer parameterization schemes. We will use the standard monthly mean archives of those variables from CMIP5. It is worth noting that, consistent with our purpose, the monthly mean of surface wind speed in the archive is the monthly average of the wind speed calculated at daily or subdaily frequency. While the wind speed at 10 m is generally less than that at 80–100 m height, the two are highly correlated and can be related by the Hellman exponent and wind gradient equation used for wind turbines (e.g., Kaltschmitt et al. [14]). Thus, we analyze the 10 m wind as a close proxy of the actual wind at the turbine height.

The simulations from the last two decades of the historical and RCP8.5 runs are used to deduce the trends. More precisely, the centennial trend is defined as the climatology of 2079–2099 minus the climatology of 1979–1999. Winter and summer will be analyzed separately. The 10 m wind data from the NCEP-DOE reanalysis-2 (Kanamitsu et al. [15], data obtained from the archive at <http://www.esrl.noaa.gov/psd/>)

for 1979–1999 will also be used to cross validate the CMIP5 historical runs.

3. Surface Wind Speed in Present and Future Climate

Figure 1 shows the climatology of the surface (10 m) wind speed over North America for the winter season (December–February) constructed from the last two decades of the 20th century historical runs (Figure 1(a)) and the last two decades of the 21st century RCP 8.5 runs (Figure 1(b)) using five different models in CMIP5. Figure 2 is similar to Figure 1 but for summer (June–August). For the 20th century simulations, the models produce the common first-order features with the highest wind speed over the oceans and relatively higher wind speed over the Great Plains compared to the Rockies and the Southeastern USA. The wind speed is higher in winter than in summer overall. These first-order features are also produced by the 21st century runs, giving the first indication that the GHG-induced climate change does not dramatically alter the surface wind field. Within either group of the 20th or 21st century runs, notable differences exist among the models. For example, in winter, GISS-E2-H and ACCESS 1.0 produce considerably stronger surface wind off the East Coast of the USA than other models; IPSL-CM5-LR and EC-Earth produce a more distinctive local maximum of surface wind over North-Central USA which is less visible in the simulations by the other three models. It is also interesting to note that only EC-Earth produces local surface wind maximum over the Great Lakes. This is because the model has the highest resolution among the five (see Table 1), high enough to partially resolve the lakes. The fine structures mentioned above that are unique to an individual model tend to exist in both the 20th and 21st century simulations by that model. This indicates that the model bias remains similar under the GHG forcing in the 21st century. In other words, if one defines the trend as the difference between the 21st century climatology and 20th century climatology, both from the same model, the bias would cancel itself. Thus, the trend so deduced can still be meaningful even if the model has biases.

Figure 3 shows the trends in the surface wind speed, defined as the 2079–2099 climatology minus the 1979–1999 climatology, over North America for winter (Figure 3(a)) and summer (Figure 3(b)), based on the simulations by the five models shown in Figures 1 and 2. The models produce

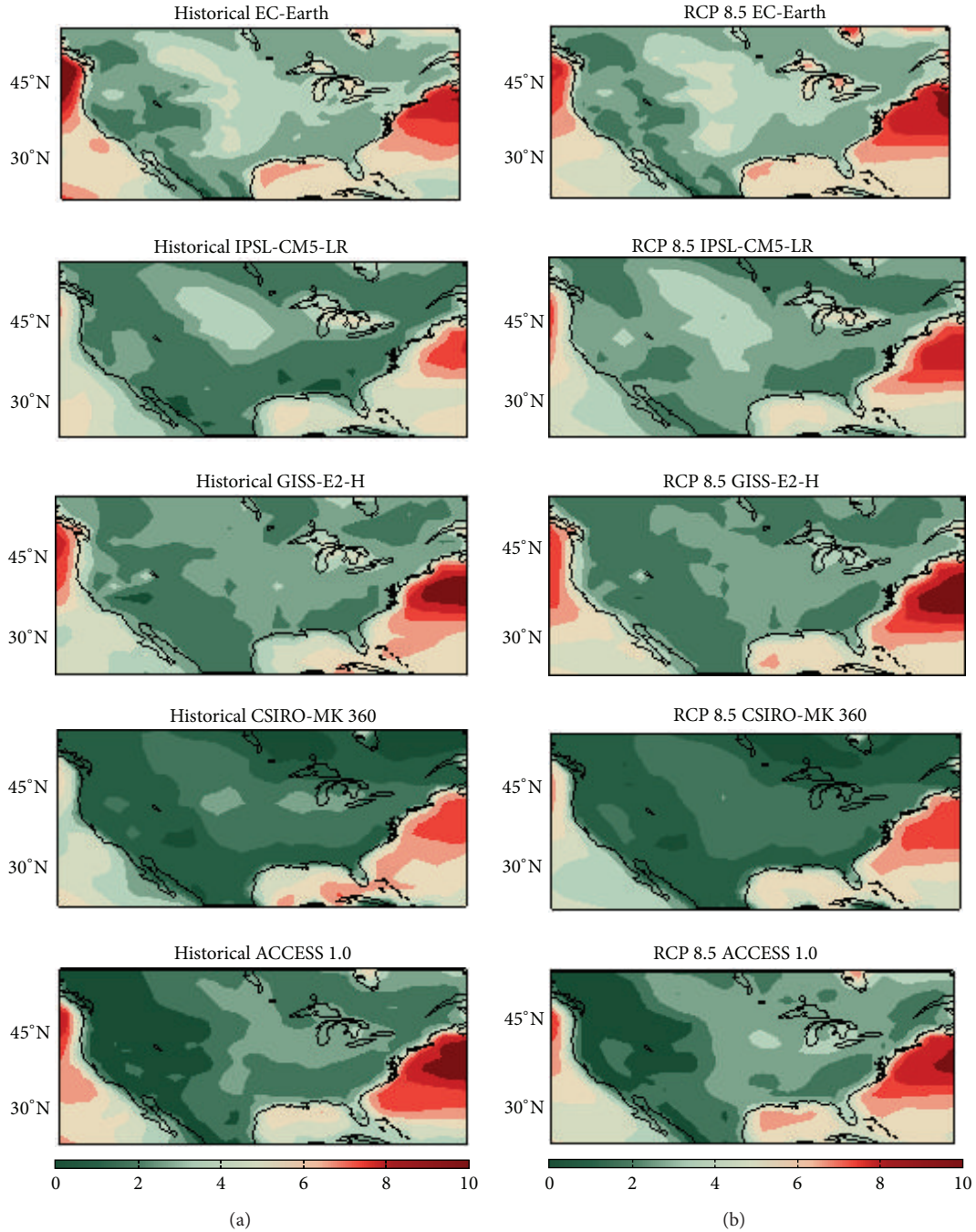


FIGURE 1: The climatology of surface wind speed over North America for winter (DJF) from the 20th century historical runs (a) and 21st century RCP 8.5 runs using five CMIP5 models as labeled at the top of each panel. The color scale, in m/s, is shown at bottom. Green and red colors represent lower and higher wind speed.

diverse responses to GHG forcing. For example, IPSL-CM5-LR produces a positive trend in winter and negative trend in summer over almost the entire North American sector, while the responses in the CSIRO-MK 3.6.0 model are muted for both seasons. Nevertheless, when averaged across the models, the GHG-induced trends in the surface wind speed are overall an increase in winter and a decrease in summer over the North American continent. The increase in the surface wind

speed in winter is broadly consistent with the enhancement of the eastward tropospheric jet stream aloft (which is a main feature in winter) found in previous analyses of the CMIP5 zonal wind data (Paek and Huang [13]).

The determination of the trends in Figure 3 is entirely based on models. As noted, if the model bias is not significantly affected by the GHG forcing in the 21st century, by taking the difference between the 21st and 20th century runs,

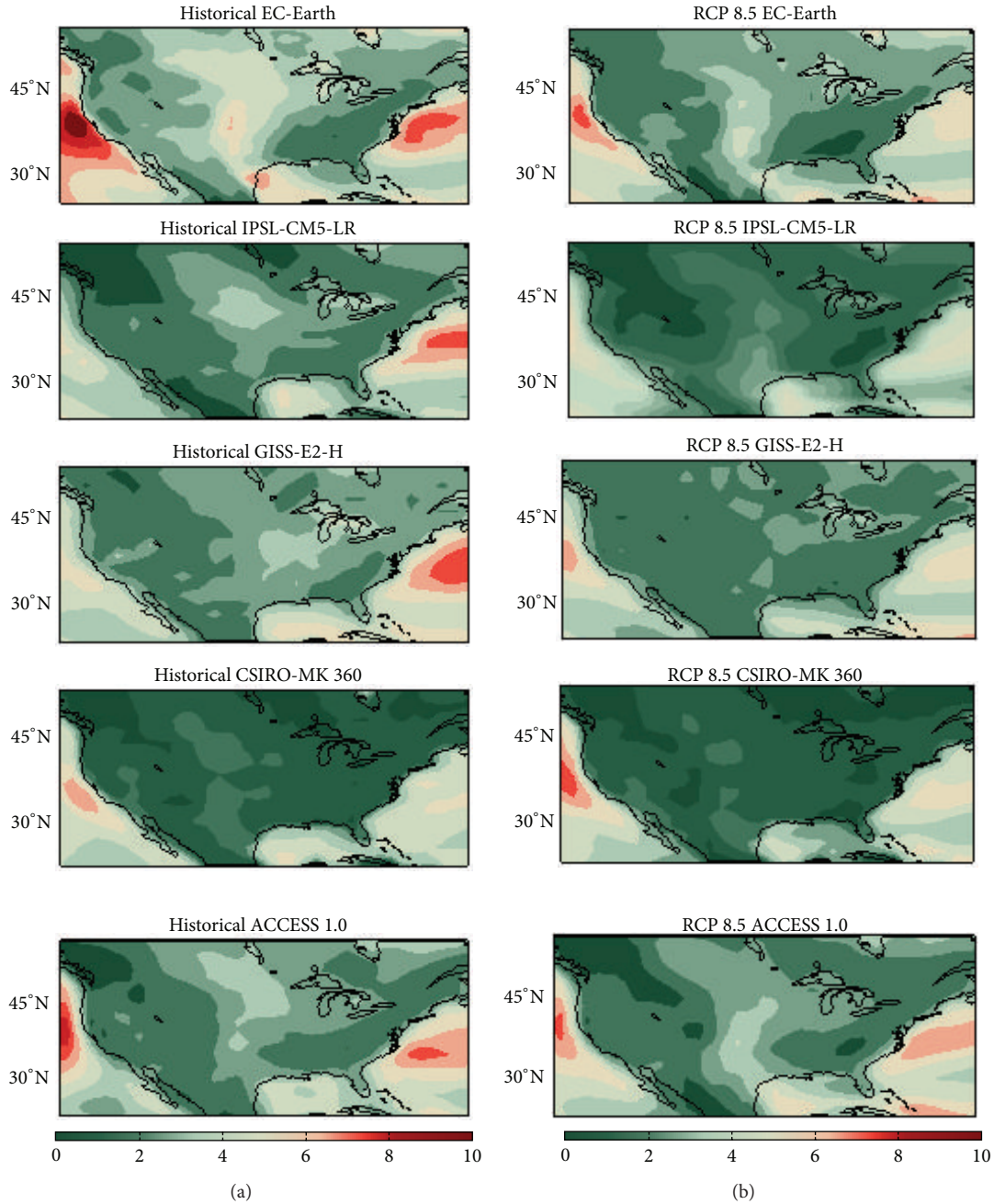


FIGURE 2: Similar to Figure 1 but for the climatology for summer (JJA). (a) and (b) are the historical and RCP 8.5 runs.

the bias would cancel itself. This philosophy is also adopted by the IPCC in its assessment reports on future climate (IPCC [5]). Nevertheless, for completeness, we should compare selected models with the 20th century reanalysis to affirm that the biases are not excessive. Figure 4 shows the 1979–1999 climatology (averaged over all seasons) of the surface wind speed from NCEP-DOE reanalysis-2 (Figure 4(a)), along with its counterparts from the historical runs using GISS-E2-H (Figure 4(b)) and EC-Earth (Figure 4(c)). The overall patterns in reanalysis and model simulations are similar, although GISS-E2-H slightly underestimates the wind speed

over West-Central US while EC-Earth overestimates it. A more complicated picture emerges if one further compares the climatology of the u - and v -components of the 10-meter wind. Figure 5(a) is similar to Figure 4 but for the v -component of surface wind and Figure 5(b) is for the u -component of it. Although EC-Earth has a larger bias in the surface wind speed, it simulates the v -component of the wind field better than GISS-E2-H. The bias in EC-Earth is mainly in the u -component. The two cases in Figures 4 and 5 suffice to illustrate that the model biases have somewhat complicated patterns but are not excessive in their magnitude. Also,

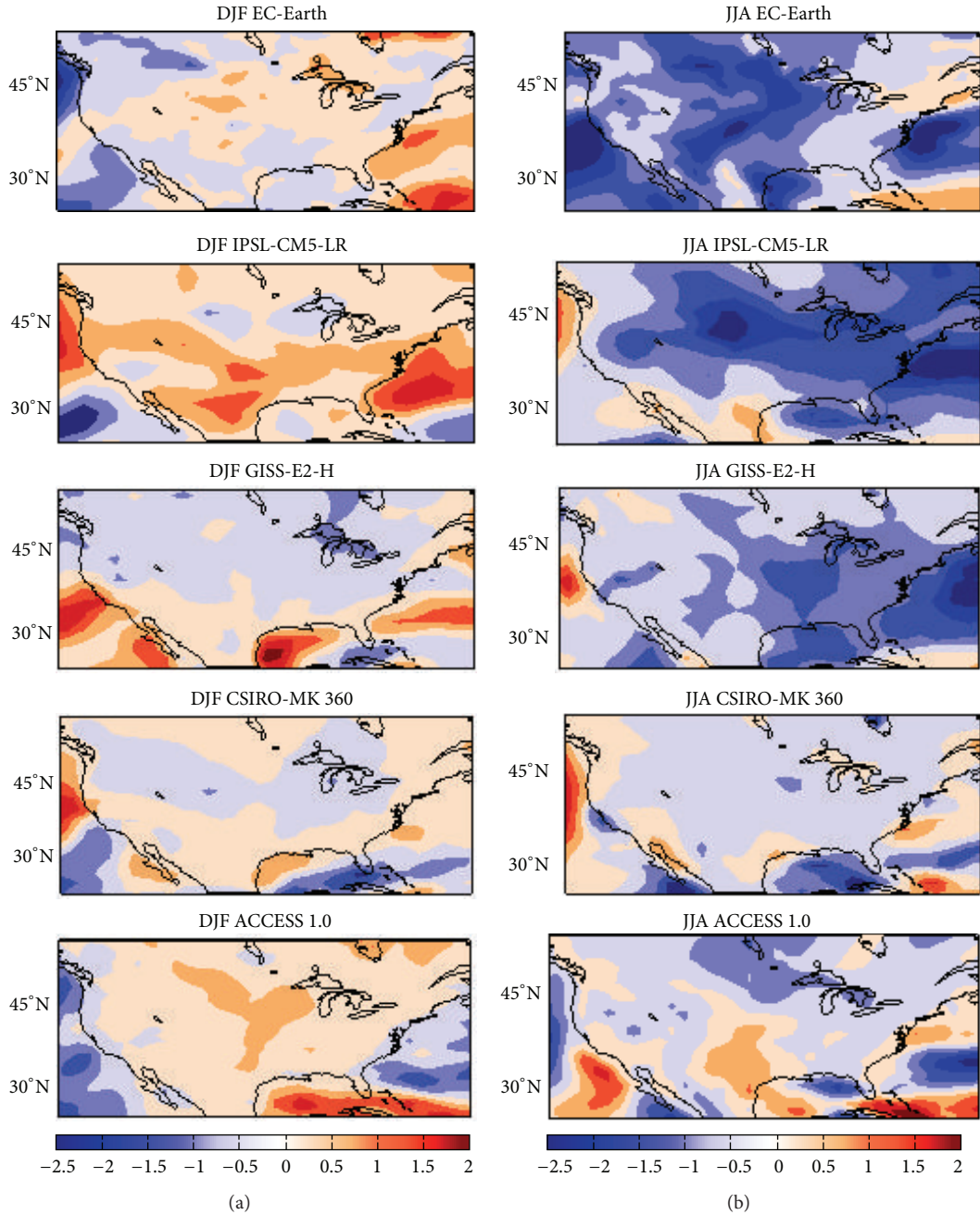


FIGURE 3: The trend [(2079–99) minus (1979–99)] in the surface wind speed over North America for winter (a) and summer (b), from five CMIP5 models as labeled at the top of each panel. The color scale, in m/s (per century), is shown at bottom. Blue and red indicate a decrease and an increase, respectively, in the surface wind speed.

a further examination did not reveal a simple correspondence between the pattern of the bias and the pattern of the trend.

4. Regional Surface Wind Fields

With the changes in the surface wind speed shown in Figure 3, one may ask if there are also changes in the wind direction. The maps of the 10-meter wind fields, for selected models and regions with notable changes in wind

speed, are shown in Figures 6 and 7. Figures 6(a) and 7(a) show the historical run and Figures 6(b) and 7(b) show the corresponding RCP 8.5 run. Wind fields are shown as the arrows, with the magnitude of the wind vector imposed in the background as the color shading. Figure 6 shows the EC-Earth simulations for Central USA (top) and the East Coast of the USA (bottom) for summer. Figure 7 shows the GISS-E2-H simulations for the Southern USA and part of Gulf of Mexico (top) and West Coast of the USA (bottom), both for

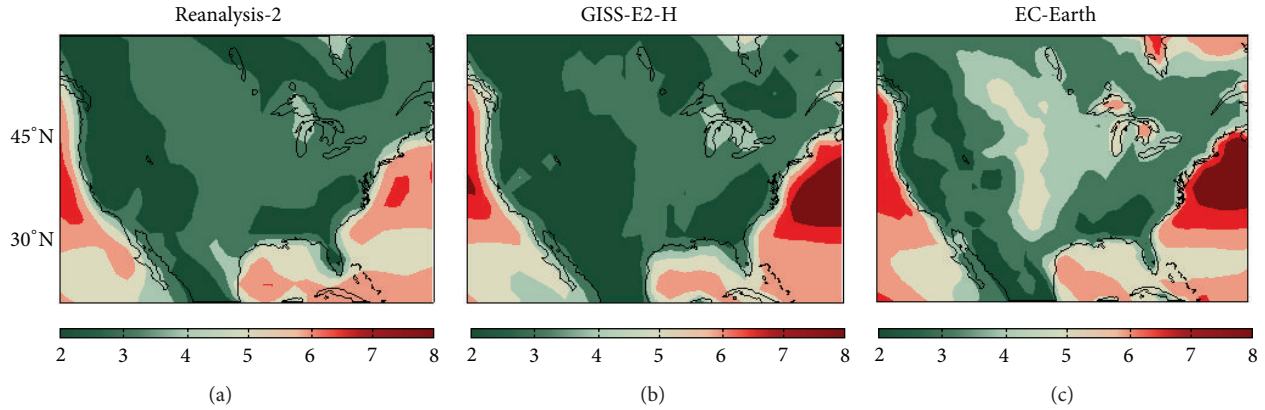


FIGURE 4: A comparison of the 1979–1999 climatology of the surface wind speed from NCEP-DOE reanalysis-2 (a) and the historical runs with two models (b) GISS-E2-H and (c) EC-Earth in CMIP5. The color scale, in m/s, is shown at bottom with red color indicating high wind speed.

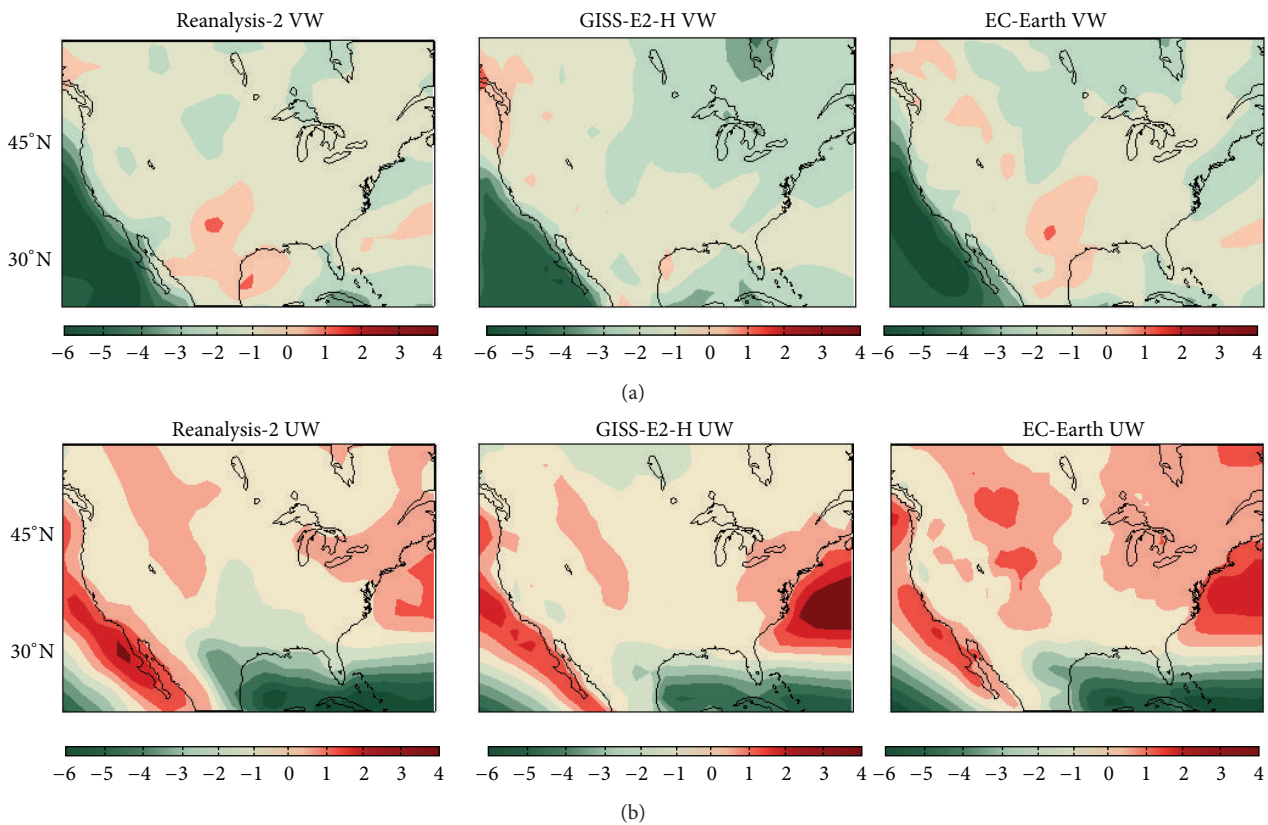


FIGURE 5: A comparison of the 1979–1999 climatology of the v -component (a) and u -component (b) of the 10 m wind over North America from reanalysis-2 (left), GISS-E2.H historical run (middle) and EC-Earth historical run (right). The color scale, in m/s, is shown at bottom. Red and green indicate positive and negative velocities.

winter. While significant changes in the wind direction are found in a few isolated places, for example, Illinois in the top row of Figure 6, and Pennsylvania and off the coast of New Jersey in the bottom row of Figure 6, for most regions shown in Figures 6 and 7 the GHG forcing does not induce major changes in the wind direction and the patterns of surface wind.

5. Discussions

Our analysis has used the wind speed and horizontal velocity field at 10-meter height that are directly available from the CMIP5 archive. It is understood that the 10 m wind is used as a proxy of the wind at the turbine height of 80–100 m, which is typically stronger than the wind at near surface. Given so,

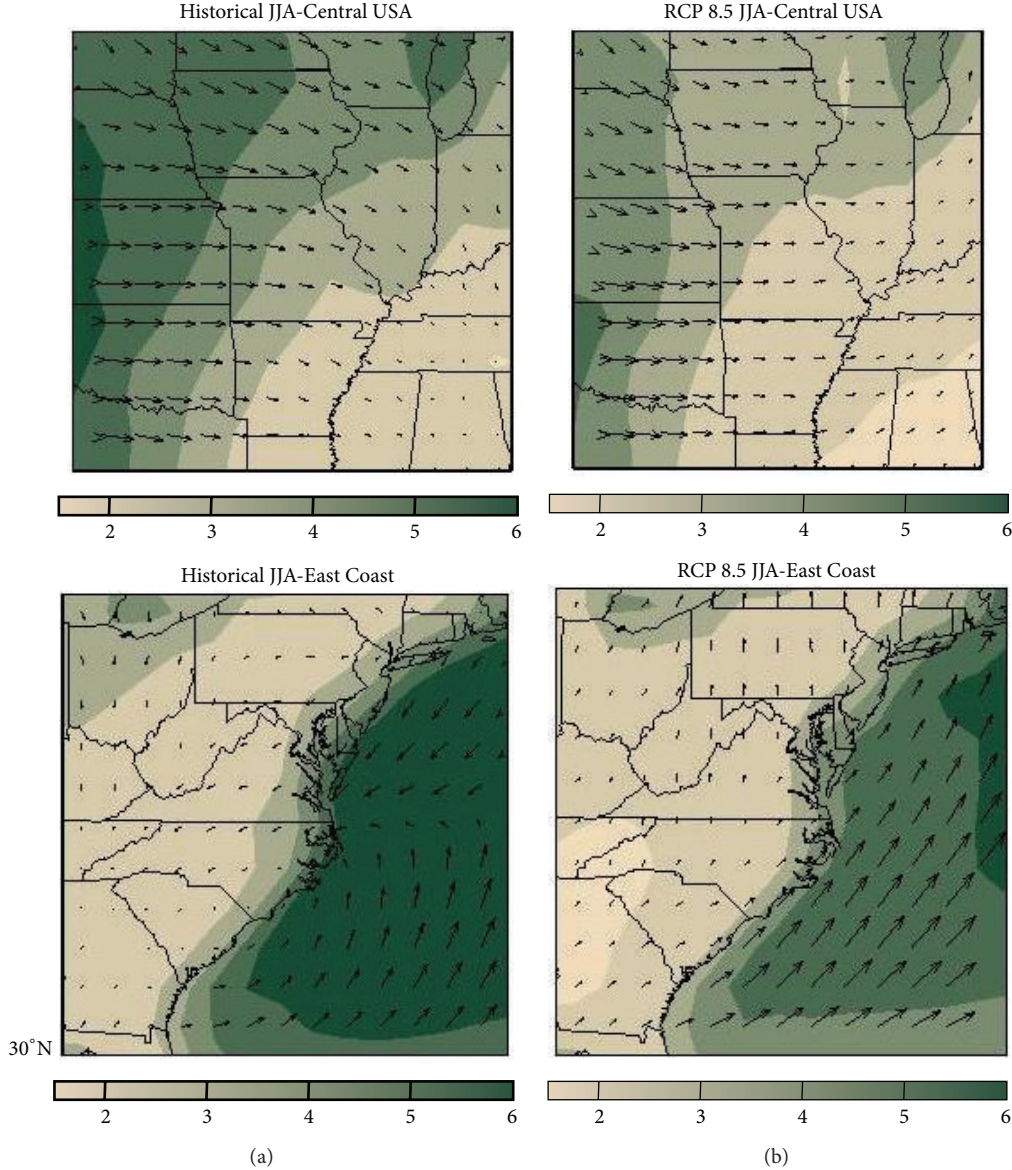


FIGURE 6: Detailed maps of the 10 m velocity fields for selected regions from the EC-Earth model simulations in CMIP5. (a) shows the 20th century historical runs and (b) the 21st century RCP 8.5 runs. Both are the average over the last two decades of the respective runs, and over summer (JJA) only. Top: Central United States. Bottom: the East Coast of the United States. The arrows indicate the climatological wind field and the color shading indicates the magnitude of the wind vectors shown. The color scale for the latter, in m/s, is shown at the bottom.

a more useful measure of the influence of the GHG forcing is perhaps the percentage change, instead of the absolute value of the change, in the 10 m wind speed. At a grid point (i, j) , where i and j are the indices for longitude and latitude, the multimodel average of the percentage change in the 10 m wind speed is defined as

$$\mu_{i,j} = \frac{1}{5} \sum_{k=1}^5 \frac{(WS21)_{k,i,j} - (WS20)_{k,i,j}}{(WS20)_{k,i,j}}, \quad (1)$$

where WS21 is the wind speed from the RCP 8.5 runs and WS20 is the wind speed from the historical runs and k is the index for the model. Since the five models have different

horizontal resolutions, the CMIP5 data were first interpolated onto the same grid (using that of the reanalysis-2) before the statistics were calculated. The calculation of $\mu_{i,j}$ would not be meaningful over the regions where the surface wind speed (WS20) is very small, where wind turbines are also less likely to be built. To exclude those regions, we consider that most of the high capacity wind turbines operate above 5 m/s for practical energy production. By Hellman exponent and wind gradient equation used for wind turbines (e.g., Kaltschmitt et al. [14]), the wind speed at 80 m is typically 1.5 to 2 times that of the wind speed at 10 m height. Thus, we will neglect the regions with the 10 m wind speed less than 2 m/s. (If at least one model meets this criterion at a given grid point, that

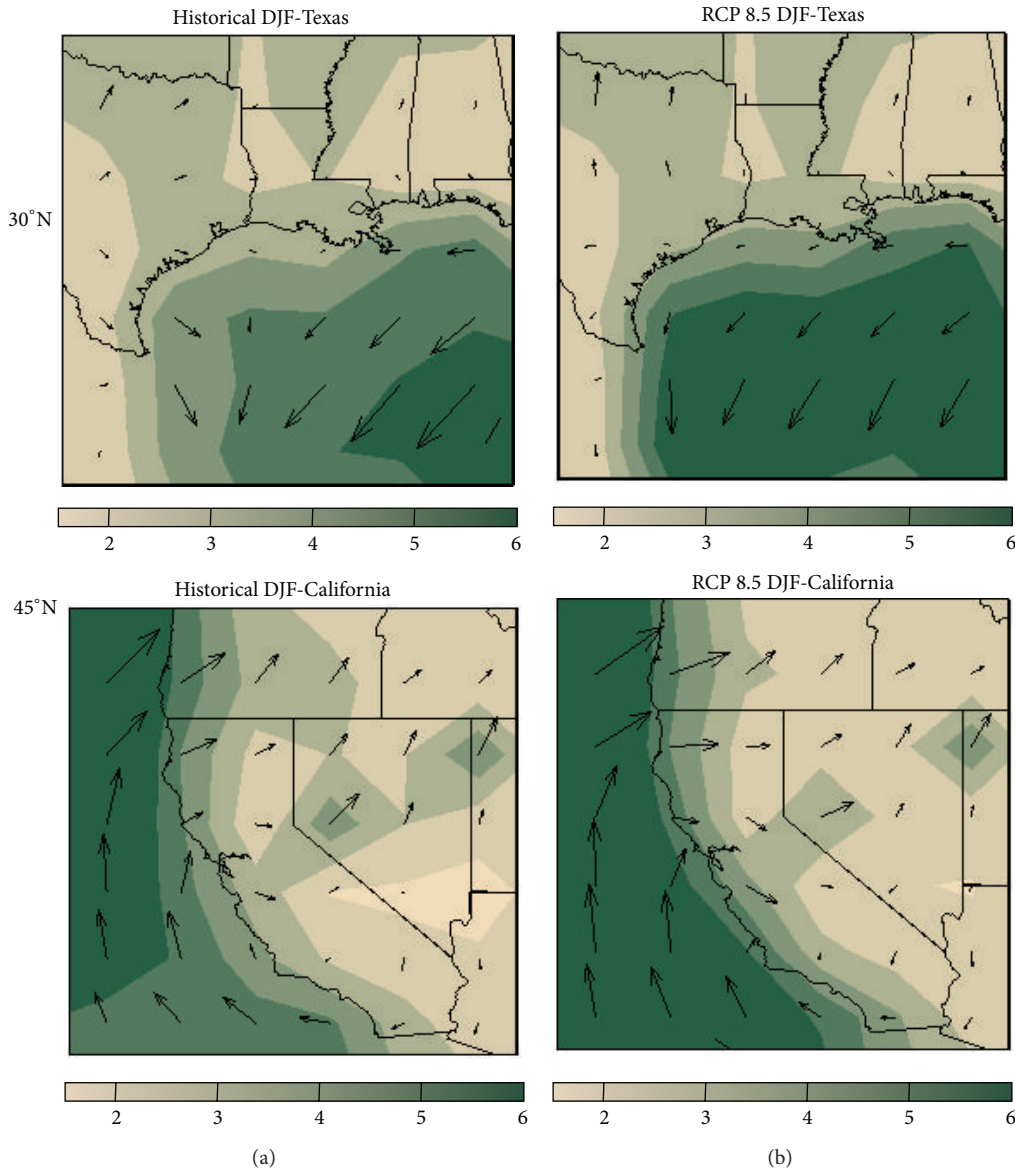


FIGURE 7: Similar to Figure 6 but for the surface wind fields from GISS-E2-H simulations for winter (DJF) and for two different regions. (a) and (b) are the historical and RCP 8.5 runs, respectively. Top: The Southern USA and part of Gulf of Mexico. Bottom: West Coast of the USA and off shore of California.

grid point is excluded from the calculation of $\mu_{i,j}$.) The maps of $\mu_{i,j}$ are shown for winter in Figure 8(a) and for summer in Figure 8(b). The white areas in Figure 8 are where either the climatology of the surface wind is small or the percentage change of the surface wind is small. The intramodel standard deviation (as a measure of the deviation from the multimodel mean, $\mu_{i,j}$) of the percentage change for the two seasons is also shown in Figure 9. The standard deviation is calculated only where the mean is calculated. For the convenience of plotting the result, in Figure 9, the standard deviation is set to zero over the areas where it is not calculated. In winter when the climatological surface wind is stronger overall, we find a moderate increase of 5–10% of the near surface wind speed over the Central and North-Central USA and the coastal regions in California and along the South and East Coasts

of the USA. Using Betz's law (wind power proportional to the cube of wind speed), the equivalent changes in wind power potential would be approximately 15–30% per century over the colored areas in Figure 8(a). In summer, a decrease in wind speed at a similar range of 5–10% is found over the aforementioned coastal regions. A greater decrease, close to 20%, is found over isolated locations in West and West-Central USA. Nevertheless, those values are less reliable since they are associated with high intramodel standard deviation (compare the Figures 8(a) and 9(a)), indicating that the higher percentage of change is contributed by one or a small number of outliers.

In the preceding analysis we converted the GHG-induced change in the 10 m wind speed to an estimate of the change in wind power potential by simply applying the cubic law to

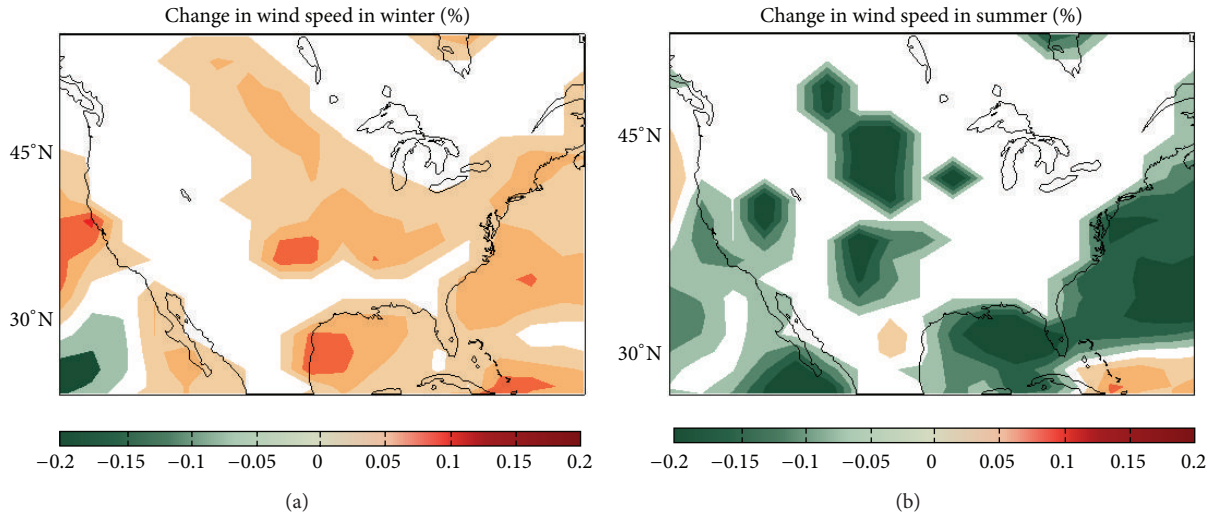


FIGURE 8: The multimodel mean of the percentage change in surface wind speed over North America for winter (a) and summer (b). See text for definition. Red indicates an increase and green indicates a decrease in wind speed. The values range from -20% to 20% , as indicated by the color scale at the bottom.

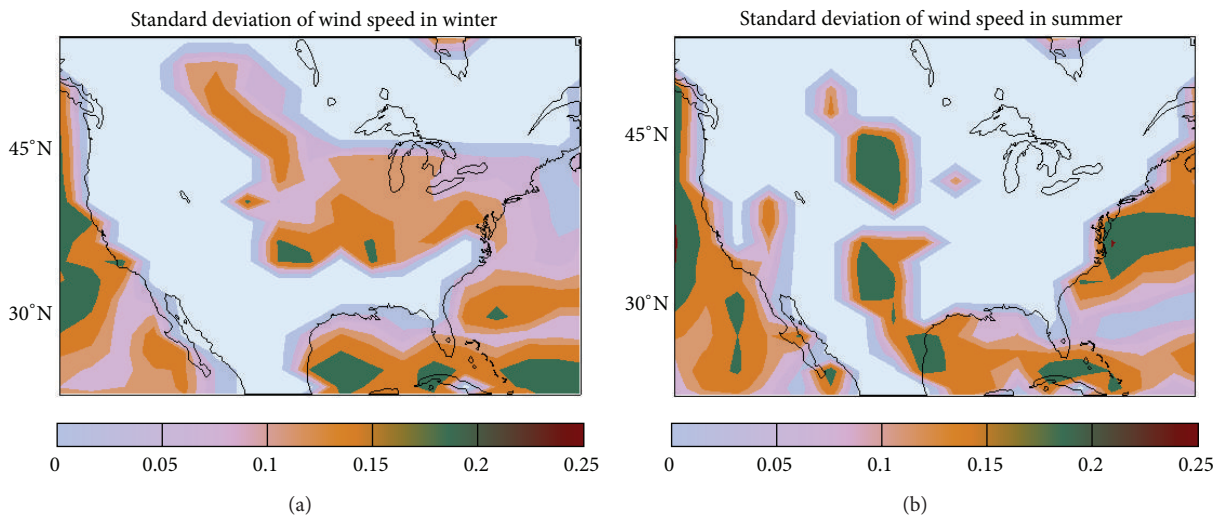


FIGURE 9: The intramodel standard deviation, with respect to the mean, as shown in Figure 8, of the percentage change in surface wind speed. (a) and (b) are for winter and summer, respectively. Where the standard deviation is not calculated (see text), it is set to zero and colored in gray. The color scale is shown at bottom.

the wind speed in the 20th and 21st century, then calculating the percentage change in “wind speed cubed.” We used this simple approach because the CMIP5 archive does not provide the detailed wind and temperature profiles in the lower boundary layer. (Air temperature is available at 2 m only.) Note that the wind speed at the turbine height, U , is approximately related to the wind speed at a reference height (10 m in our case), U_R , by the relation of $(U/U_R) = (Z/Z_R)^\alpha$, where Z and Z_R are the heights of the turbine and the reference level and α (~ 0.14 for a neutrally stable profile) is an adjustable parameter (e.g., Peterson and Hennessey Jr. [16]). Thus, we obtained the estimate of the percentage change in wind power potential by implicitly assuming that α , or the static stability profile in the lower boundary layer, is not

changed by the GHG forcing in the future. A validation of this assumption is beyond the scope of this study but will be a useful future work for climate modeling with high vertical resolutions.

Our results of the changes in surface wind speed and wind direction suggest that the GHG forcing (as used in CMIP5 simulations under the RCP 8.5 scenario) has a moderate, but not major, influence on the near-surface wind fields over North America. This broadly agrees with the conclusion of Pryor and Barthelmie [8] that the estimate of wind power potential over the USA using present-day climatology will remain useful in the coming decades. Note that the trend considered in this study is defined as the centennial change over the whole 21st century. The equivalent change over only

the next 50 years (as discussed by Pryor and Barthelmie [8]) would be smaller. The RCP 8.5 scenario chosen for our analysis is among the ones with a higher estimate of future GHG emissions. If the RCP 4.5 scenario was chosen, the projected trend would also be smaller.

6. Concluding Remarks

Using 5 models from the CMIP5 archive and comparing the RCP 8.5 runs with historical runs, moderate centennial trends in the 10 m wind speed are projected over North America. In winter, we found 5–10 percent increases per century over Central and East-Central United States, the Californian Coast, and the South and East Coasts of the USA. In summer, decreases in the wind speed ranging from 5 to 10 percent per century are found over the same coastal regions. These projected changes in the surface wind speed are moderate overall. From the global model projections, the estimate of wind power potential for North America based on present-day climatology will remain accurate in the coming decades. The relatively coarse resolutions of the global models do not allow an accurate representation of the mesoscale and submesoscale topography, which might affect the projections of the changes in the surface wind field. Our results will serve as a useful basis to guide future work on downscaling the CMIP5 model outputs to the submesoscale, which may help resolve the topographic effects. The RCP scenarios used in CMIP5 do not consider the effects of future land-use changes, including those related to the construction of large-scale wind farms. An integration of those effects into regional climate modeling, using the CMIP5 global model outputs as the boundary conditions, will help refine the conclusions of this work.

Conflict of Interests

The authors declare that there is no conflict of interests regarding the publication of this paper.

References

- [1] A. Lopez, B. D. Roberts, N. Heimiller, N. Blair, and G. Porro, "U.S Renewable Energy Technical Potential: A GIS based analysis," Tech. Rep. NREL/TP-6A20-51946, National Renewable Energy Laboratory, Golden, Colo, USA, 2012.
- [2] J. M. Freedman, K. T. Waight, and P. B. Duffy, "Does climate change threaten wind resources?" *North American Wind Power*, vol. 6, pp. 49–53, 2009.
- [3] D. Ren, "Effects of global warming on wind energy availability," *Journal of Renewable and Sustainable Energy*, vol. 2, no. 5, Article ID 052301, 2010.
- [4] K. E. Taylor, R. J. Stouffer, and G. A. Meehl, "An overview of CMIP5 and the experiment design," *Bulletin of the American Meteorological Society*, vol. 93, no. 4, pp. 485–498, 2012.
- [5] IPCC, *Climate Change 2013: The Physical Science Basis*, Working Group I Contribution to Fifth Assessment Report of Intergovernmental Panel on Climate Change, Cambridge University Press, Cambridge, UK, 2013.
- [6] R. Seager, M. Ting, I. Held et al., "Model projections of an imminent transition to a more arid climate in southwestern North America," *Science*, vol. 316, no. 5828, pp. 1181–1184, 2007.
- [7] N. C. Baker and H.-P. Huang, "A comparative study of precipitation and evaporation in semiarid regions between the CMIP3 and CMIP5 climate model ensembles," *Journal of Climate*, vol. 27, no. 10, pp. 3731–3749, 2014.
- [8] S. C. Pryor and R. J. Barthelmie, "Assessing climate change impacts on the near-term stability of the wind energy resource over the United States," *Proceedings of the National Academy of Sciences of the United States of America*, vol. 108, no. 20, pp. 8167–8171, 2011.
- [9] L. O. Mearns, R. Arritt, S. Biner et al., "The North American regional climate change assessment program: overview of phase I results," *Bulletin of the American Meteorological Society*, vol. 93, no. 9, pp. 1337–1362, 2012.
- [10] G. A. Meehl, C. Covey, T. Delworth et al., "The WCRP CMIP3 multimodel dataset: a new era in climatic change research," *Bulletin of the American Meteorological Society*, vol. 88, no. 9, pp. 1383–1394, 2007.
- [11] D. W. Keith, J. F. DeCarolis, D. C. Denkenberger et al., "The influence of large-scale wind power on global climate," *Proceedings of the National Academy of Sciences of the United States of America*, vol. 101, no. 46, pp. 16115–16120, 2004.
- [12] A. S. Adams and D. W. Keith, "Are global wind power resource estimates overstated?" *Environmental Research Letters*, vol. 8, Article ID 015021, 2013.
- [13] H. Paek and H.-P. Huang, "Centennial trend and decadal-to-interdecadal variability of atmospheric angular momentum in CMIP3 and CMIP5 simulations," *Journal of Climate*, vol. 26, no. 11, pp. 3846–3864, 2013.
- [14] M. Kaltschmitt, W. Streicher, and A. Wiese, *Renewable Energy: Technology, Econom Ics, and Environment*, Springer, New York, NY, USA, 2007.
- [15] M. Kanamitsu, W. Ebisuzaki, J. Woollen et al., "NCEP-DOE AMIP-II reanalysis (R-2)," *Bulletin of the American Meteorological Society*, vol. 83, no. 11, pp. 1631–1559, 2002.
- [16] E. W. Peterson and J. P. Hennessey Jr., "On the use of power laws for estimates of wind power potential," *Journal of Applied Meteorology*, vol. 17, no. 3, pp. 390–394, 1978.

Research Article

Generalized Scaling of Urban Heat Island Effect and Its Applications for Energy Consumption and Renewable Energy

T.-W. Lee,¹ Heung S. Choi,² and Jinh Lee¹

¹ Department of Mechanical and Aerospace Engineering, Arizona State University, Tempe, AZ 85287-6106, USA

² Department of Mechanical and Design Engineering, Hongik University, Sejong, Republic of Korea

Correspondence should be addressed to T.-W. Lee; attwl@asu.edu

Received 14 March 2014; Accepted 9 June 2014; Published 18 August 2014

Academic Editor: Huei-Ping Huang

Copyright © 2014 T.-W. Lee et al. This is an open access article distributed under the Creative Commons Attribution License, which permits unrestricted use, distribution, and reproduction in any medium, provided the original work is properly cited.

In previous work from this laboratory, it has been found that the urban heat island intensity (UHI) can be scaled with the urban length scale and the wind speed, through the time-dependent energy balance. The heating of the urban surfaces during the daytime sets the initial temperature, and this overheating is dissipated during the night-time through mean convection motion over the urban surface. This may appear to be in contrast to the classical work by Oke (1973). However, in this work, we show that if the population density is used in converting the population data into urbanized area, then a good agreement with the current theory is found. An additional parameter is the “urban flow parameter,” which depends on the urban building characteristics and affects the horizontal convection of heat due to wind. This scaling can be used to estimate the UHI intensity in any cities and therefore predict the required energy consumption during summer months. In addition, all urbanized surfaces are expected to exhibit this scaling, so that increase in the surface temperature in large energy-consumption or energy-producing facilities (e.g., solar electric or thermal power plants) can be estimated.

1. Introduction

There have been many studies on the causes and impact of the heat island effect (e.g., [1–9]). A wide range of causes have been attributed, including the land surface energy balance (or imbalance) due to urbanized land surface and built structures, anthropogenic heat release, and different atmospheric constituents over the city [10, 11]. While the significance of the urban heat island effect is universally recognized [12, 13], the approaches to its understanding and mitigation are quite varied, ranging from simple “slab” approach [14] to sophisticated models that resolve urban canopy physics [15, 16]. One of the important aspects is quantifying the magnitude of the urban heat island effect in terms of relevant variables, which again vary widely depending on the authors. A key step in this quantification is “scaling,” that is, developing a functional relationship between the urban heat island effect and causal variables.

In previous work from this laboratory, we have shown that scaling of the urban heat island effect based on time-dependent energy balance works quite well in understanding

and predicting the UHI dependence on the urban length scale and wind speeds [17]. This approach is in contrast to the scaling used by many authors [18–24], where a steady-state energy balance is used along with horizontal and vertical heat flux terms. It is clear that the urban island heating (as well as cooling) is not a steady-state effect, nor is the UHI intensity determined at some fixed time, as shown in Figure 1 where a typical time evolution of the UHI intensity is plotted. In this work, we show that if the population density is used in converting the population data into urbanized area in Oke’s work [9], then a good agreement with the current theory is found. An additional parameter is the “urban flow parameter,” which depends on the urban building characteristics and affects the horizontal convection of heat due to wind. This scaling can be used to estimate the UHI intensity in any cities and therefore predict the required energy consumption during summer months. In addition, all urbanized surfaces are expected to exhibit this scaling, so that increase in the surface temperature in large energy-consumption or energy-producing facilities (e.g., solar electric or thermal power plants) can be estimated. About one-third of the electric

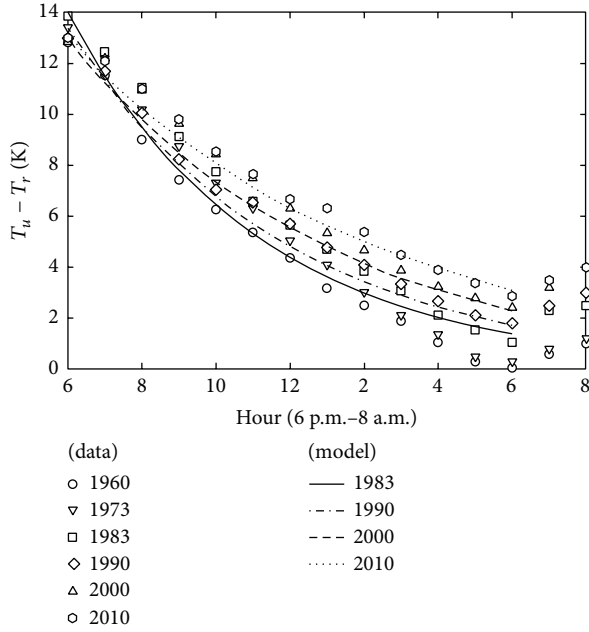


FIGURE 1: Temperature decay as a function of time, in Phoenix, AZ, for years 1960 to 2010, using (3).

power goes to satisfy the residential consumption in United States, and thus understanding of the electricity demand due to UHI increase is a key component in planning for renewable energy production.

2. Methods of Analyses

A brief summary of the scaling is given below. The starting point is the fundamental energy balance equation [17]:

$$\rho c_p \frac{\partial T_u}{\partial t} + \rho c_p U \frac{\partial T_u}{\partial x} = \dot{q}'' , \quad (1)$$

where \dot{q}'' is the divergence of the eddy-diffusive heat flux. The air density and specific heat are ρ and c_p , respectively, while U is the convection speed, often approximated as the mean wind velocity over the urban area. The spatial gradient in the temperature can be approximated and moved to the right-hand side. In our previous work [17], we considered the time evolution of the urban temperature during night hours, after the heat flux from the surface has led to some “equilibrium” temperature above the urban surface. This argument considers the heat flux term to set some initial urban temperature, prior to subsequent cooling, and thus heat flux term in (1) has been removed and absorbed into the initial temperature difference $(T_u - T_r)_o$. For now, we can retain this term, as it can have additive effect on the urban air temperature during the night hours. The temperatures, T_u and T_r , represent temperatures in the urban and rural locations, respectively, and $(T_u - T_r)$ has been used as the UHI intensity:

$$\frac{\partial T_u}{\partial t} \approx -U \frac{T_u - T_r}{L} + \frac{\dot{q}''}{\rho c_p} . \quad (2)$$

If we integrate while retaining only the first term on the right-hand side, we obtain the temporal evolution of the UHI intensity. This assumes that the convection effect is much stronger than the heat flux term:

$$\Delta T(t) = T_u - T_r = (T_u - T_r)_o \exp\left(-K \frac{U}{L} t\right), \quad (3)$$

where $K = 1$ in the limiting case of $\dot{q}'' = 0$ and $K < 1$ in general, if the diffusive heat flux retarding the night cooling process is taken into account. This exponential decay in the temperature difference is closely reflected by typical data for time evolution at night hours in Figure 1.

On the other hand, if we consider the other extreme case of zero wind speed and retain only the heat flux term, then we obtain

$$T_u - T_r = (T_u - T_r)_o + \frac{\dot{q}''}{\rho c_p} t. \quad (4)$$

From (3), we can see that the wind speed, U , has the obvious effect of enhancing the cooling of the heated air over the urban surface. The larger the urban length scale is, L , the longer it would take to cool T_u . The heat flux term, as shown in (4), adds to the urban temperature until the heat is completely dissipated. The urban-rural breeze usually results in an enhanced convection motion due to mean wind in urban areas, which dominates the heat transfer process over the heat flux term due to eddy diffusion. For compactness, we retain the solution form of (4) and use a correction factor, K , to reflect the facts that (1) the temperature decay will be delayed by the heat flux term and (2) different urban surface morphologies, aerodynamic properties, and atmospheric stability may affect the effectiveness of wind speed in cooling of the urban temperature. Thus, a large heat flux term and structural impedance to convection cooling will both result in smaller value of K . We can observe from (3) then that the cooling should undergo an exponential decay as a function of time (Figure 1), and depending on the above factors the final minimum temperature achieved will be the so-called night-time minimum temperature typically reported in meteorological data sets. In addition, the wind speed also should lead to an exponential decrease in UHI. A large set of data has been used to validate this model, and an example is shown in Figure 2 where the wind speed effect for various urban areas is shown to follow the exponential decrease according to (3).

In this work, we have used the data reported by Oke [9], along with the population and urban surface area data dated at the same time period (1968–1978), in order to offer further proof that the correct scaling for the UHI intensity should be based on time-dependent energy balance and that there is exponential dependence as a function of time, wind speed, and the urban length scale. The following Canadian cities are considered as in Oke [9]: Montreal, St. Hyacinthe, St. Hubert, Chambly, Marieville, St. Basile-Le Grand, St. Cesaire, St. Pie, Ste. Angele-de Monnoir, and Ste. Madeline.

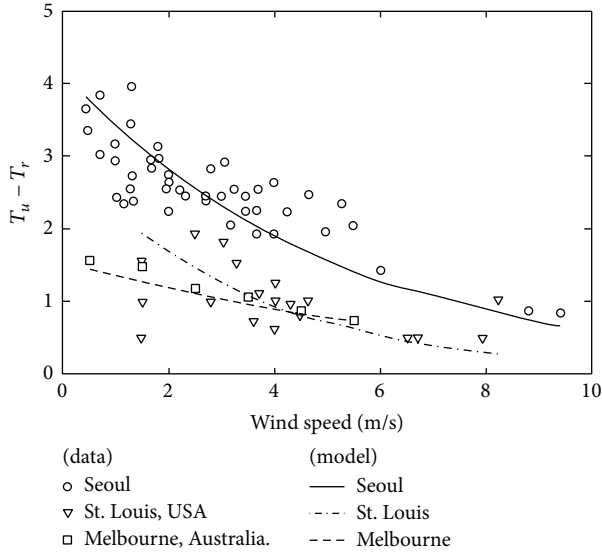


FIGURE 2: The effect of the wind speed on the UHI intensity in Seoul, Korea, St. Louis, USA, and Melbourne, Australia. The theoretical lines are obtained using (3). $(T_u - T_r)$ is the UHI intensity defined as the maximum difference in the temperatures in the urban and rural locations.

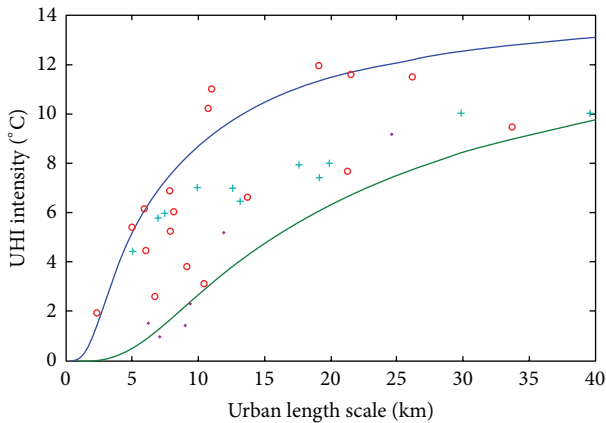


FIGURE 3: UHI intensity as a function of the urban length scale. Symbols represent data as reported by Oke [9]. The upper curve is (3) with $K = 1.0$, while the lower is for $K = 0.25$.

3. Results

Figure 3 shows the UHI intensity as a function of the urban length scale, for all of the cities reported in Oke [9]. In Oke’s work, the UHI intensity was correlated and plotted as a function of the population (“city size”), but no sound physical basis was given. Other authors have attempted a similar correlation, but different slopes were required for North American, European, Japanese, and Korean cities. Figure 3 shows that the UHI intensity for Canadian cities can be plotted using the current scaling, within the upper ($K = 1$) and lower ($K = 0.25$) bounds, using the urban area converted to the urban length scale of the identical time periods. As noted above and in our previous work, the parameter K

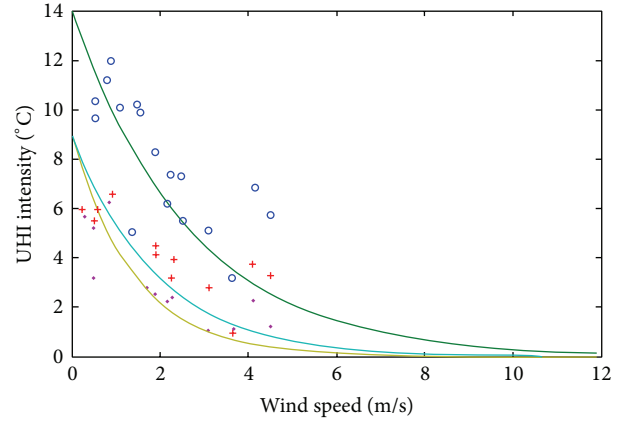


FIGURE 4: The effect of the wind speed on the UHI intensity in Chambly, Marieville, St. Basile-Le Grand, St. Cesaire, St. Pie, Ste. Angele-de Monnoir, and Ste. Madeline. Symbols represent data as reported by Oke [9], while the theoretical lines are obtained from (3).

depends on the urban morphological characteristics. Thus, there is a direct effect of increase in the urban length scale on the UHI intensity. In our previous work [17], we have investigated the growth of two cities, Phoenix and Tucson, based on the satellite image analyses, and corresponding increase in the urban length scale. Of course, the growth of urban areas depends on many economical and sociological parameters, as the expected growth of Phoenix, for example, has been halted in 2008 due to housing meltdown.

Thus far, in this and our previous work [17], we have looked at cities around the world with widely disparate population densities, urban surface morphology, and meteorological conditions. Although the general UHI characteristics are captured by (3), exact functional relationships tend to vary as shown in Figure 3 even for cities within Canada. Thus, incorporating and categorizing the effects of urban surface morphology and meteorological conditions into the parameter K in (3) remain as the next task in this formation for the UHI scaling.

Figures 4, 5, and 6 show the effects of the wind speed on the UHI intensity for the same Canadian cities as in Figure 3. It can be observed that functional relationship between the UHI intensity and the wind speed is accurately captured using (3). Hunt et al. [25] have also looked at the scaling of UHI effects for large urban areas and attempted to link the worsening of UHI effects on global warming. As shown in (3), the initial temperature difference between urban and rural areas does determine the final UHI intensity. However, the more direct factors are the urban length scale and the wind speed, since the global warming would elevate the temperatures in urban and rural areas uniformly.

4. Conclusions

Effects of the urban length scale and the wind speed on the urban heat island effect can be quantified through time-dependent energy balance. The heating of the urban surfaces

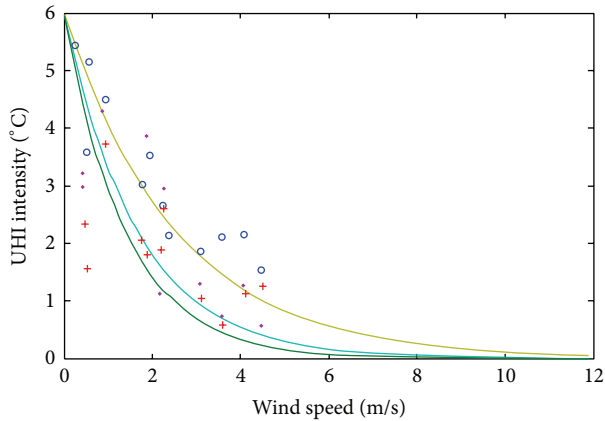


FIGURE 5: The effect of the wind speed on the UHI intensity in Chambly, Marieville, and St. Basile-Le Grand.

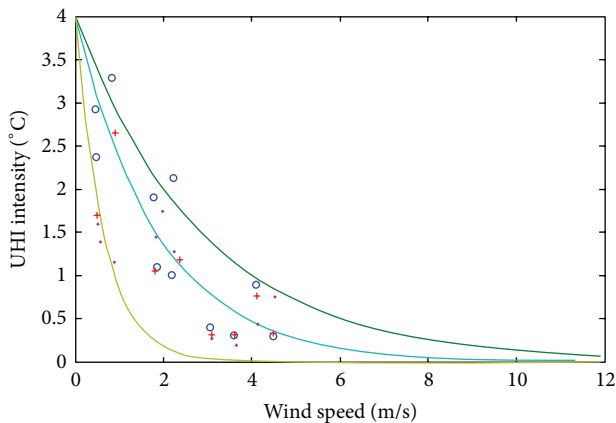


FIGURE 6: The effects of wind speed on UHI intensity for St. Cesaire, St. Pie, and Ste. Angele-de Monnoir.

during the daytime sets the initial temperature, and this overheating is cooled during the nighttime through mean convection motion over the urban surface, resulting in an exponential decay in the temperature. This overheating is cooled during the nighttime, through mean convection motion over the urban surface, resulting in an exponential decay in the temperature. The solution to the time-dependent energy balance equation reproduces this temporal decay with good accuracy, with the main factors being the length scale of the urban area and the wind speed. The minimum temperature reached at the end of night-time cooling period then corresponds to the UHI intensity, which increases with increasing urban length scale and decreasing wind speed. The wind speed effect is also accurately retraced using this method; however, different correction factors are required for different cities, indicating the effects of the urban surface heat content, structural morphology, and density. Thus, using a small number of readily available data for the urban length scale and the wind speed, the UHI intensity can be described with possible projections for future trends. This approach can be used in planning of energy resources, as well as any large areas of concrete surfaces needed for renewable or other

power generation. About one-third of the electric power goes to satisfy the residential consumption in United States, and thus understanding of the electricity demand due to UHI increase is a key component in planning for renewable energy production.

Conflict of Interests

The authors declare that there is no conflict of interests regarding the publication of this paper.

References

- [1] L. A. Baker, A. J. Brazel, N. Selover et al., "Urbanization and warming of Phoenix (Arizona, USA): impacts, feedbacks and mitigation," *Urban Ecosystems*, vol. 6, pp. 183–203, 2002.
- [2] A. Brazel, N. Selover, R. Vose, and G. Heisler, "The tale of two climates: baltimore and phoenix urban LTER sites," *Climate Research*, vol. 15, no. 2, pp. 123–135, 2000.
- [3] J. R. Christy, W. B. Norris, K. Redmond, and K. P. Gallo, "Methodology and results of calculating central California surface temperature trends: evidence of human-induced climate change?" *Journal of Climate*, vol. 19, no. 4, pp. 548–563, 2006.
- [4] A. T. J. de Laat and A. N. Maurellis, "Evidence for influence of anthropogenic surface processes on lower tropospheric and surface temperature trends," *International Journal of Climatology*, vol. 26, no. 7, pp. 897–913, 2006.
- [5] E. Kalnay and M. Cai, "Impact of urbanization and land-use change on climate," *Nature*, vol. 423, no. 6939, pp. 528–531, 2003.
- [6] D. Pearlmuter and P. Berliner, "Street canyon geometry and microclimate: designing for urban comfort under arid conditions," in *Environmentally Friendly Cities*, E. Maldonado and S. Yannas, Eds., Proceedings of PLEAS '98, pp. 165–166, Lisbon, Portugal, 1998.
- [7] Y. Rydin, "Environmental dimensions of residential development and the implications for local planning practice," *Journal of Environmental Planning & Management*, vol. 35, no. 1, pp. 43–61, 1992.
- [8] B. Stone Jr. and M. O. Rodgers, "Urban form and thermal efficiency how the design of cities influences the Urban heat island effect," *Journal of the American Planning Association*, vol. 67, no. 2, pp. 186–198, 2001.
- [9] T. R. Oke, "City size and the urban heat island," *Atmospheric Environment*, vol. 7, no. 8, pp. 769–779, 1973.
- [10] H. E. Landsberg, *Atmospheric Changes in a Growing Community*, Technical Note—Institute for Fluid Dynamics and Applied Mathematics, BN 823, Institute for Fluid Dynamics and Applied Mathematics, University of Maryland, College Park, Md, USA, 1975.
- [11] D. J. Sailor, "A review of methods for estimating anthropogenic heat and moisture emissions in the urban environment," *International Journal of Climatology*, vol. 31, no. 2, pp. 189–199, 2011.
- [12] A. J. Arnfield, "Two decades of urban climate research: a review of turbulence, exchanges of energy and water, and the urban heat island," *International Journal of Climatology*, vol. 23, no. 1, pp. 1–26, 2003.
- [13] W. T. L. Chow, D. Brennan, and A. J. Brazel, "Urban heat island research in phoenix, Arizona: Theoretical contributions and policy applications," *Bulletin of the American Meteorological Society*, vol. 93, no. 4, pp. 517–530, 2012.

- [14] C. S. B. Grimmond, H. A. Cleugh, and T. R. Oke, "An objective urban heat storage model and its comparison with other schemes," *Atmospheric Environment B: Urban Atmosphere*, vol. 25, no. 3, pp. 311–326, 1991.
- [15] F. Chen, H. Kusaka, R. Bornstein et al., "The integrated WRF/urban modelling system: development, evaluation, and applications to urban environmental problems," *International Journal of Climatology*, vol. 31, no. 2, pp. 273–288, 2011.
- [16] Z.-H. Wang, E. Bou-Zeid, and J. A. Smith, "A spatially-analytical scheme for surface temperatures and conductive heat fluxes in urban canopy models," *Boundary-Layer Meteorology*, vol. 138, no. 2, pp. 171–193, 2011.
- [17] T. W. Lee and A. Ho, "Scaling of the urban heat island effect based on the energy balance: nighttime minimum temperature increase vs. urban area length scale," *Climate Research*, vol. 42, no. 3, pp. 209–216, 2010.
- [18] P. W. Summers, *An urban ventilation model applied to Montreal [Ph.D. thesis]*, McGill University, 1964.
- [19] I. Uno, S. Wakamatsu, H. Ueda, and A. Nakamura, "An observational study of the structure of the nocturnal urban boundary layer," *Boundary-Layer Meteorology*, vol. 45, no. 1-2, pp. 59–82, 1988.
- [20] R. Richiardone and G. Brusasca, "Numerical experiments on urban heat island intensity," *Quarterly Journal of the Royal Meteorological Society*, vol. 115, no. 488, pp. 983–995, 1989.
- [21] S. S. Raman and J. E. Cermak, "Physical modeling of flow and diffusion over an urban heat island," *Advances in Geophysics*, vol. 18, pp. 223–240, 1975.
- [22] J. Lu, P. Arya, W. H. Snyder, and R. E. Lawson Jr., "A laboratory study of the urban heat island in a calm and stably stratified environment. Part I: temperature field," *Journal of Applied Meteorology*, vol. 36, no. 10, pp. 1377–1391, 1997.
- [23] J. Lu, S. P. Arya, W. H. Snyder, and R. E. Lawson Jr., "A laboratory study of the urban heat island in a calm and stably stratified environment—part II—velocity field," *Journal of Applied Meteorology*, vol. 36, no. 10, pp. 1392–1402, 1997.
- [24] A. Cenedese and P. Monti, "Interaction between an inland urban heat island and a sea-breeze flow: a laboratory study," *Journal of Applied Meteorology and Climatology*, vol. 42, pp. 1569–1583, 2003.
- [25] J. C. Hunt, Y. V. Timoshkina, S. I. Bohnenstengel, and S. Belcher, "Implications of climate change for expanding cities worldwide," *Proceedings of the ICE—Urban Design and Planning*, vol. 166, no. 4, pp. 214–254, 2012.

Research Article

Climate Change Impact on Photovoltaic Energy Output: The Case of Greece

**Ioanna S. Panagea,¹ Ioannis K. Tsanis,^{1,2}
Aristeidis G. Koutroulis,¹ and Manolis G. Grillakis¹**

¹ Department of Environmental Engineering, Technical University of Crete, GR73100 Chania, Greece

² Department of Civil Engineering, McMaster University, Hamilton, ON, Canada L8S 4L7

Correspondence should be addressed to Ioannis K. Tsanis; tsanis@hydromech.gr

Received 4 April 2014; Revised 6 June 2014; Accepted 9 June 2014; Published 2 July 2014

Academic Editor: Huei-Ping Huang

Copyright © 2014 Ioanna S. Panagea et al. This is an open access article distributed under the Creative Commons Attribution License, which permits unrestricted use, distribution, and reproduction in any medium, provided the original work is properly cited.

Solar power is the third major renewable energy, constituting an increasingly important component of global future—low carbon—energy portfolio. Accurate climate information is essential for the conditions of solar energy production, maximization, and stable regulation and planning. Climate change impacts on energy output projections are thus of crucial importance. In this study the effect of projected changes in irradiance and temperature on the performance of photovoltaic systems in Greece is examined. Climate projections were obtained from 5 regional climate models (RCMs) under the A1B emissions scenario, for two future periods. The RCM data present systematic errors against observed values, resulting in the need of bias adjustment. The projected change in photovoltaic energy output was then estimated, considering changes in temperature and insolation. The spatiotemporal analysis indicates significant increase in mean annual temperature (up to 3.5°C) and mean total radiation (up to 5 W/m²) by 2100. The performance of photovoltaic systems exhibits a negative linear dependence on the projected temperature increase which is outweighed by the expected increase of total radiation resulting in an up to 4% increase in energy output.

1. Introduction

Solar photovoltaic systems have largely penetrated the global energy market and especially Europe. According to the European Photovoltaic Industry Association [1], photovoltaics (PV) for second consecutive year is the dominant new source of electricity production installed in Europe, where 55% of the global market of new connected to the grid capacity in 2012 with 17.2 GW is installed. PV systems consist of a competitive alternative for the decarbonization of Europe's energy sector, as they cover 2.6% of the electricity demand and 5.2% of the peak electricity demand. In 2012, 912 MW of PV was installed in Greece, increasing the PV contribution to 4% of the electricity demands.

Market trends show an expected decrease in the PV system prices from up to 2.31 €/W in 2012 in the residential segment to as low as 1.30 €/W in 2022 [2]. PV market in several countries as Greece is influenced by the political decisions and financial support. Nowadays because of

the hard recession there is a decrease in large-scale PV projects installation. However, there is still potential of the Greek PV market to grow.

There is strong correlation between irradiation and temperature [3]. The downward irradiation that reaches the troposphere and the earth surface is absorbed by the atmospheric particles and the earth surface, respectively, emitting back long wave radiation (in the infrared spectrum) that increases the ambient heat and thus the temperature. However, the downward irradiation is largely affected by the cloud cover. Clouds affect the irradiation in three main ways. Firstly, they block a fraction of the direct downward irradiation (and thus affect negatively the direct radiation that reaches the earth surface) [4]. Secondly, they diffuse the already absorbed fraction of the irradiation to all directions, increasing the diffusive irradiation that reaches the earth surface. Thirdly, they block part of the long wave radiation that was supposed to be emitted from earth, back to space (greenhouse effect). The latter affects positively

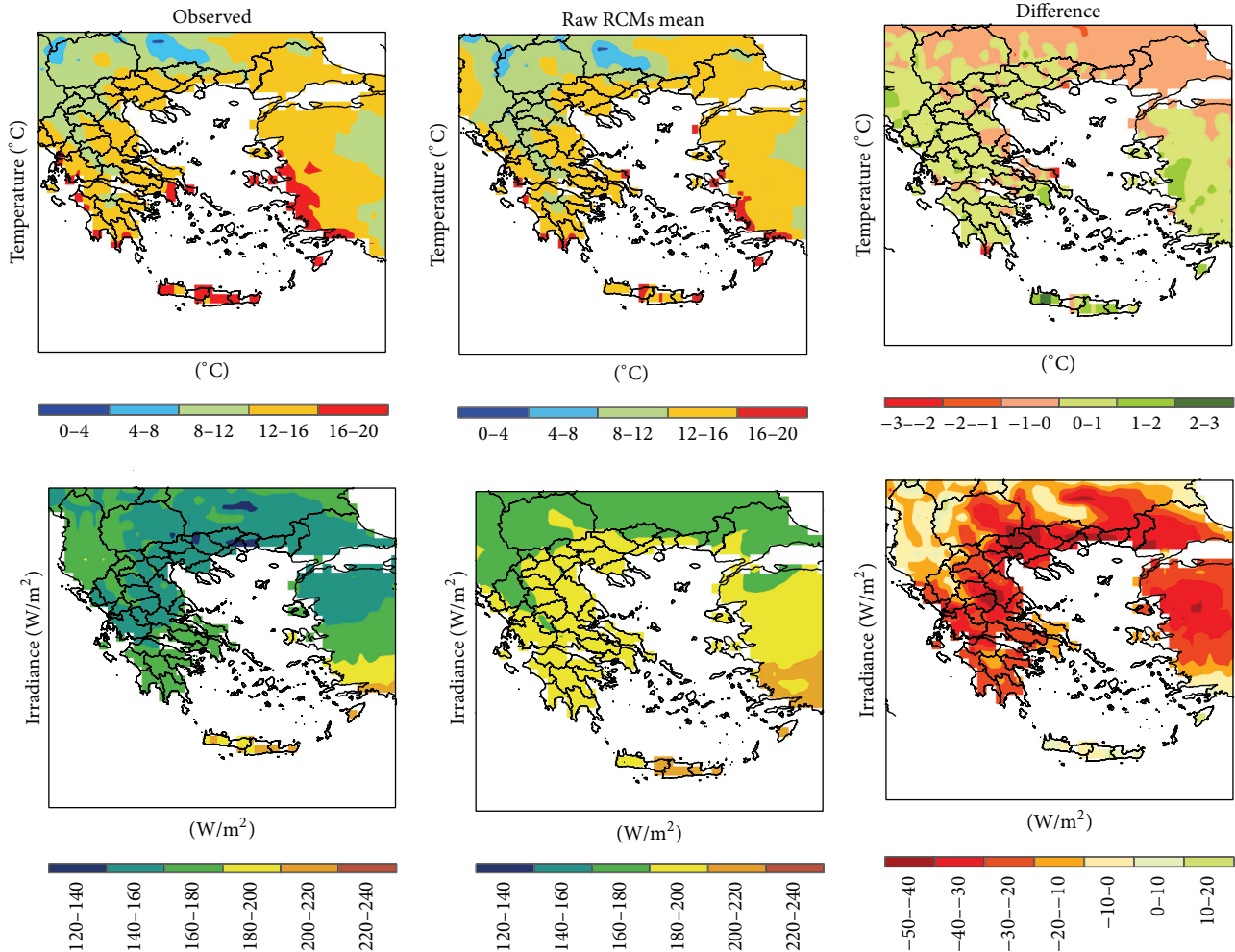


FIGURE 1: Maps of average temperature (upper) and irradiance (lower) for the control period based on observations (left panels), the ensemble mean (middle panels), and their difference (right panels).

the near surface air temperature. However, the near surface air temperature is largely affected by the air mass temperature. To account for all these interactions simultaneously, regional climate models (RCMs) are used to produce estimations of surface radiation components and temperature [5].

The performance of PV systems is largely influenced by internal and external factors such as the structural features, visual loss, aging, radiation, shading, temperature, wind, pollution, and electrical losses [6–9]. Climate change will impact temperature and irradiance and therefore will alter the output capacity of PV systems [10]. PV systems present a negative linear relationship between the energy output and the temperature change [11], while the increase of solar radiation is proportional to the PV energy output.

The use of high spatial resolution RCMs has become more common over global circulation models (GCMs), which may not be precise enough to describe local climatic processes [12]. The main disadvantage of RCMs is that model projections have considerable uncertainties. The major sources of uncertainty in climate change research lie in the techniques

used to force RCMs with boundary conditions, downscaling methods, and greenhouse gases emissions scenarios [13].

RCMs tend to simulate meteorological data with different statistical characteristics related to the observed-measured values. The time independent component of the error is the bias [14]. Studies [12] have shown that both GCMs and RCMs tend to overestimate the temperature in regions that present wet winters and dry summers and especially during the summer in south-eastern Europe [15]. The use of bias correction is thus required in order to adjust the climate models output according to the existing climate regime. Boberg and Christensen [12], Haerter et al. [14], Christensen et al. [15], and Terink et al. [16] emphasize the necessity of bias correction in order for the forced impact models to derive useful results in hydrology, water resources management, and other climate applications.

The correction methodology depends on the data type, the temporal and spatial resolution of data, and the time scale. In order to cope with the uncertainties related to the different possible detailed realizations of the climate system,

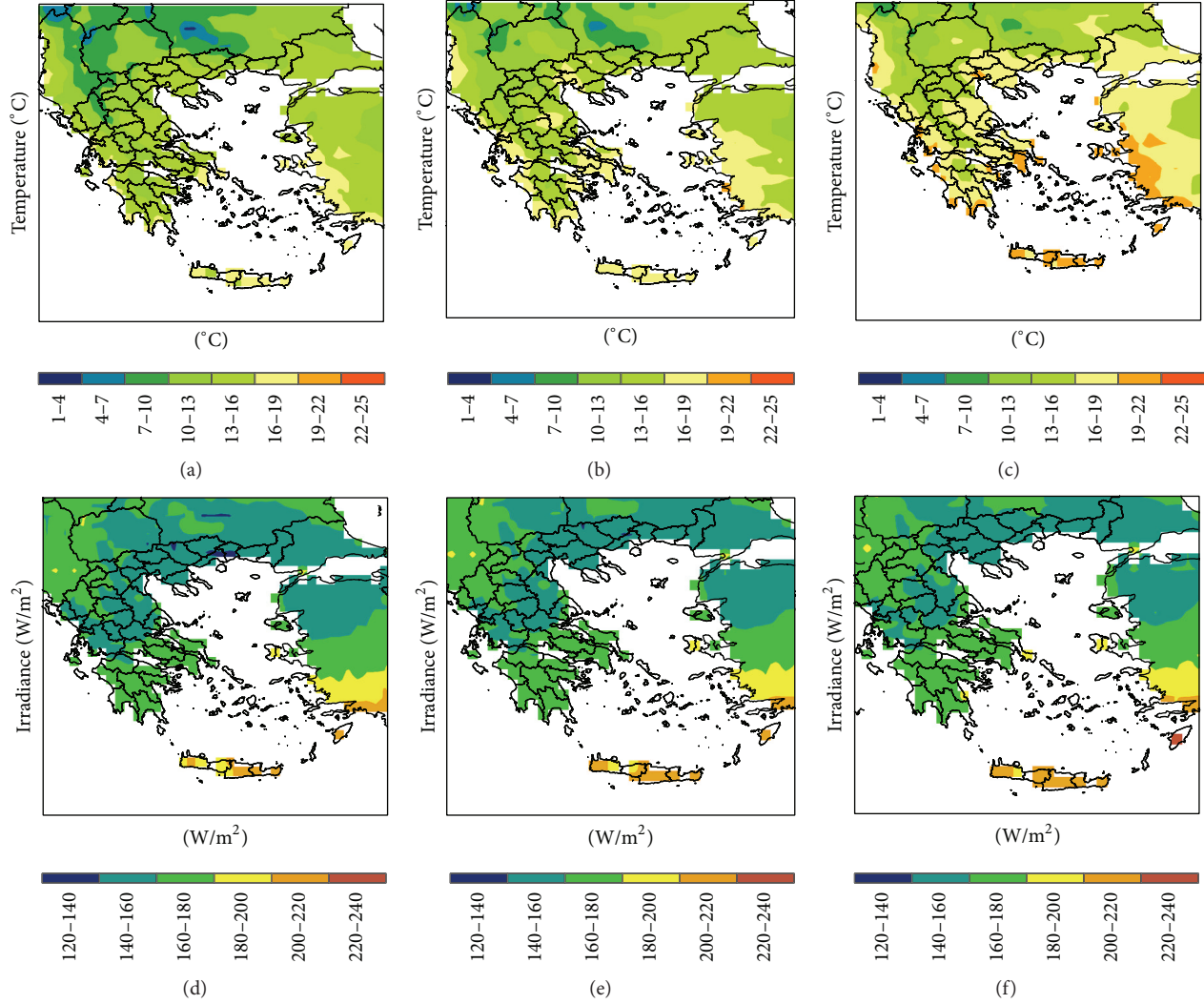


FIGURE 2: Mean temperature (upper) and irradiance (lower) fields over Greece for the reference (a, d) period, 2011–2050 period (b, e), and 2061–2100 period (c, f).

ensembles of climate models output are used. Different GCMs can be used to quantify the uncertainty related to the different physical parameterizations of the large-scale land and atmosphere processes. Moreover, different RCMs can also be used to account for the uncertainties related to the representation of smaller scale processes, such as cloud microphysics or precipitation convection.

2. Methodology

2.1. Bias Correction. RCM temperature and irradiance outputs were corrected for their biases in mean and standard deviation for each calendar month, following the methodology presented in Haerter et al. [14]. The bias in mean is corrected by subtracting the differences found between observed and modeled values and a correction to the model data is performed to conform to the variability of the historical data. This procedure takes the sequence of anomalies and scales them consistently with the observed historical variability. In

the case where data follow normal distribution the transfer function is linear and is of the form shown in the following equation:

$$\chi_{sc}^{cor} = (\chi_{mod}^{sc} - \overline{\chi_{mod}^{con}}) * \left(\frac{\sigma_{obs}^{con}}{\sigma_{mod}^{con}} \right) + \overline{\chi_{obs}^{con}}, \quad (1)$$

where χ_{sc}^{cor} is the final adjusted time series, χ_{mod}^{sc} is the raw model predictions for the scenario period, $\overline{\chi_{obs}^{con}}$ and $\overline{\chi_{mod}^{con}}$ are the mean of observed and modeled data for the control period, respectively, and σ_{obs}^{con} and σ_{mod}^{con} are the standard deviations of observed and modeled data for the control period, respectively.

The final adjusted model time series exhibits the appropriate baseline mean and standard deviation with respect to the observed data.

2.2. Estimation of PV Energy Output under Variable Conditions of Temperature and Irradiance. In order to estimate

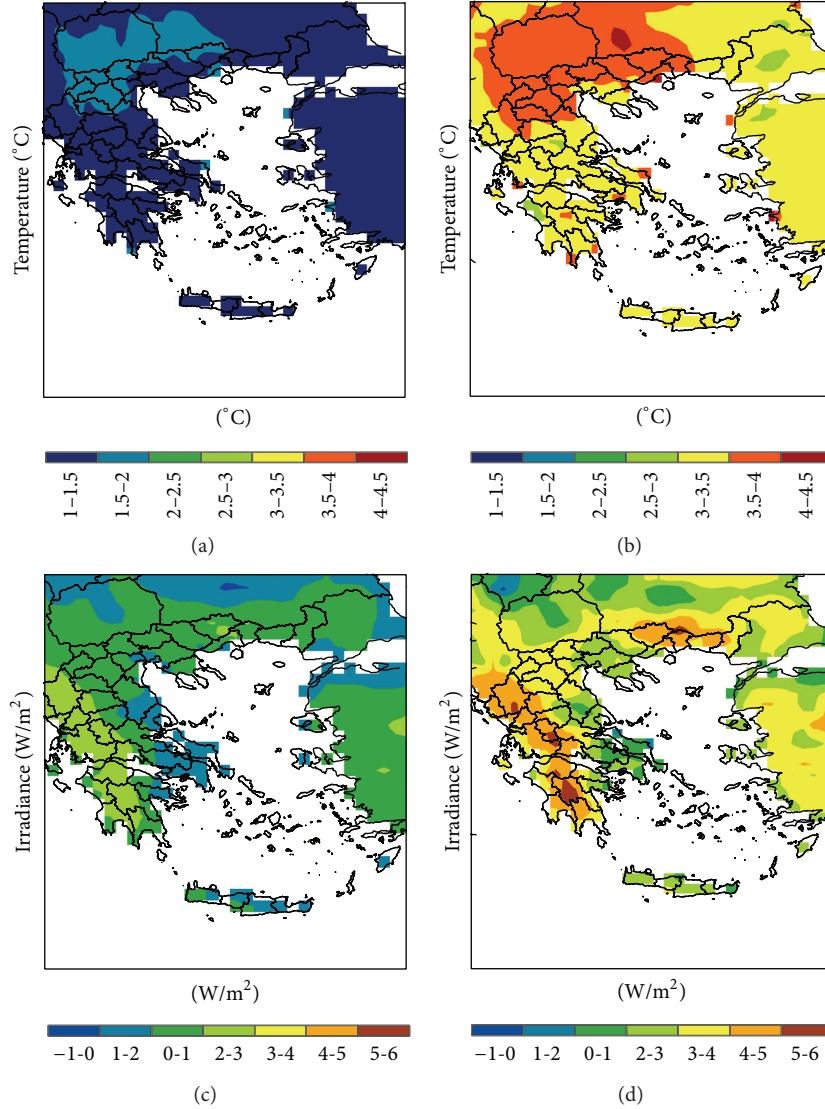


FIGURE 3: Absolute difference between reference and 2011–2050 period (a, c) and between reference and 2061–2100 (b, d) for temperature (upper) and irradiance (lower).

the potential percentage change in PV output, the fractional change $\Delta P_{PV}/P_{PV}$ is calculated from the ratio between (2) and (3) taken from Crook et al. [10]. Consider the following:

$$\begin{aligned} & \frac{\Delta P_{PV}}{\eta_{ref}} \\ &= -\Delta T G_{tot} \beta c_2 + \Delta G_{tot} (1 - \beta c_1 + \beta T_{ref} - 2\beta c_3 - T\beta c_2) \\ & \quad - \Delta G_{tot}^2 \beta c_3 - \Delta G_{tot} \Delta T \beta c_2 + \Delta G_{tot} \gamma \log_{10} (G_{tot} + \Delta G_{tot}) \\ & \quad + G_{tot} \gamma \log_{10} \left(\frac{G_{tot} + \Delta G_{tot}}{G_{tot}} \right), \end{aligned} \quad (2)$$

$$\frac{P_{PV}}{\eta_{ref}} = G_{tot} (1 - \beta (c_1 + c_2 T + c_3 G_{tot} - T_{ref}) + \gamma \log_{10} G_{tot}), \quad (3)$$

where ΔP_{PV} is the change in photovoltaic power output, η_{ref} is the reference photovoltaic efficiency, ΔT is the change in temperature between the baseline and the scenario period, ΔG is the change in irradiance between the baseline and the scenario period, T is the daytime temperature for the baseline period, estimated by (4) as it can be found in Crook et al. [10], G_{tot} is the irradiance over the daylight for the actual cloud cover for the baseline period, calculated by (5) taken from Crook et al. [10], and T_{ref} is the reference temperature in which the performance of PV cell is estimated by the manufacturer. β is the temperature coefficient set by cell

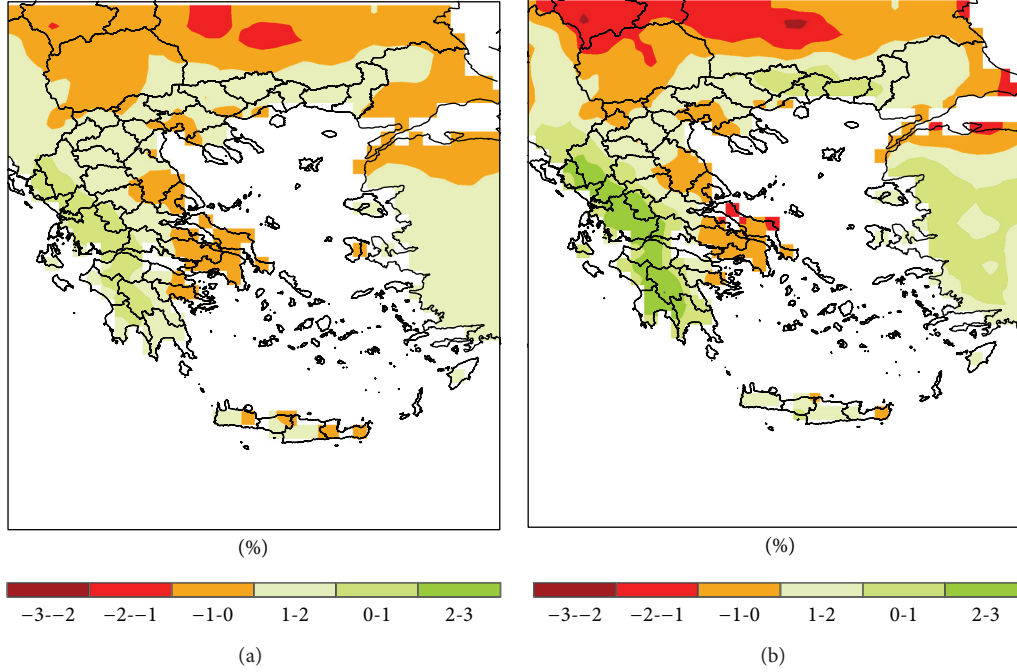


FIGURE 4: Estimated change in PV output for (a) the 2011–2050 period and (b) for the 2061–2100 period.

material and structure, γ is the irradiance coefficient set by cell material and structure, and c_1 , c_2 , and c_3 are coefficients which depend on details of the module and mounting that affect heat transfer from the cell. Consider the following:

$$T = \bar{T} + \frac{\overline{\text{DTR}}}{4}, \quad (4)$$

where DTR is the diurnal range of the temperature (difference between minimum and maximum temperature) and \bar{T} is the monthly average temperature. Consider

$$G_{\text{tot}} = \bar{G} \frac{t_{24\text{h}}}{t_{\text{daylength}}}, \quad (5)$$

where \bar{G} is the monthly average irradiance and $t_{\text{daylength}}$ is the time of the daylight, calculated as monthly average, for all latitudes of the study site every 0.25° .

3. Case Study Area and Data Used

Monthly means of surface temperature and irradiance projections were obtained for five regional climate models of the ENSEMBLES (<http://ensemblesr3.dmi.dk/>) database, under the special report on emissions scenarios (SRES) A1B emission scenario of the Intergovernmental Panel on Climate Change (IPCC). The main objectives of the ENSEMBLES project were to provide an ensemble prediction system based on the state of the art of high resolution global and regional earth system models developed in Europe. The produced simulations were validated by using high resolution gridded datasets for Europe to produce an objective probabilistic

estimate of uncertainty in future climate at the seasonal to decadal and longer timescales. More information about the ENSEMBLES project can be found in UK Met Office page <http://ensembles-eu.metoffice.com/> [21]. Detailed information about used RCMs temporal resolution is presented in Table 1. The processing of the climate data was performed in the ENSEMBLES RCMs spatial resolution which is 0.25 degrees.

The E-OBS [22] dataset provided observed minimum and maximum temperature data between 1950 and 2000. The SoDa database (<http://www.soda-is.com>) between 1985 and 2005 with spatial resolution of 20 km was used as an observational irradiance dataset. The SoDa server provides daily irradiation time series over Europe, Africa, and Atlantic Ocean, which is accessible on a free basis [23]. It supplies information of high quality, matching the actual needs of users, with improved time-space coverage and sampling [24]. The SoDa irradiance is satellite derived data of HelioClim-1 Daily Solar Irradiance v4.0 (HelioClim-1 Database of Daily Solar Irradiance v4.0 derived from satellite data, MINES ParisTech, Armines, France). HelioClim databases use the Heliosat-2 [25] method to process the Meteosat Images. The Heliosat method converts images acquired by meteorological geostationary satellites, such as Meteosat (Europe), GOES (USA) or GMS (Japan), into data and maps of solar radiation received at ground level. Mines ParisTech produced the method Heliosat-2 in November 2002, partly with the support of the European Commission (project SoDa Contract DG “INFOS” IST-1999-12245). The accuracy of the HelioClim-1 data is discussed in detail by Lefèvre et al. [26]. They assessed the accuracy of the HelioClim-1 data against ground measurements of the WMO radiometric network (55

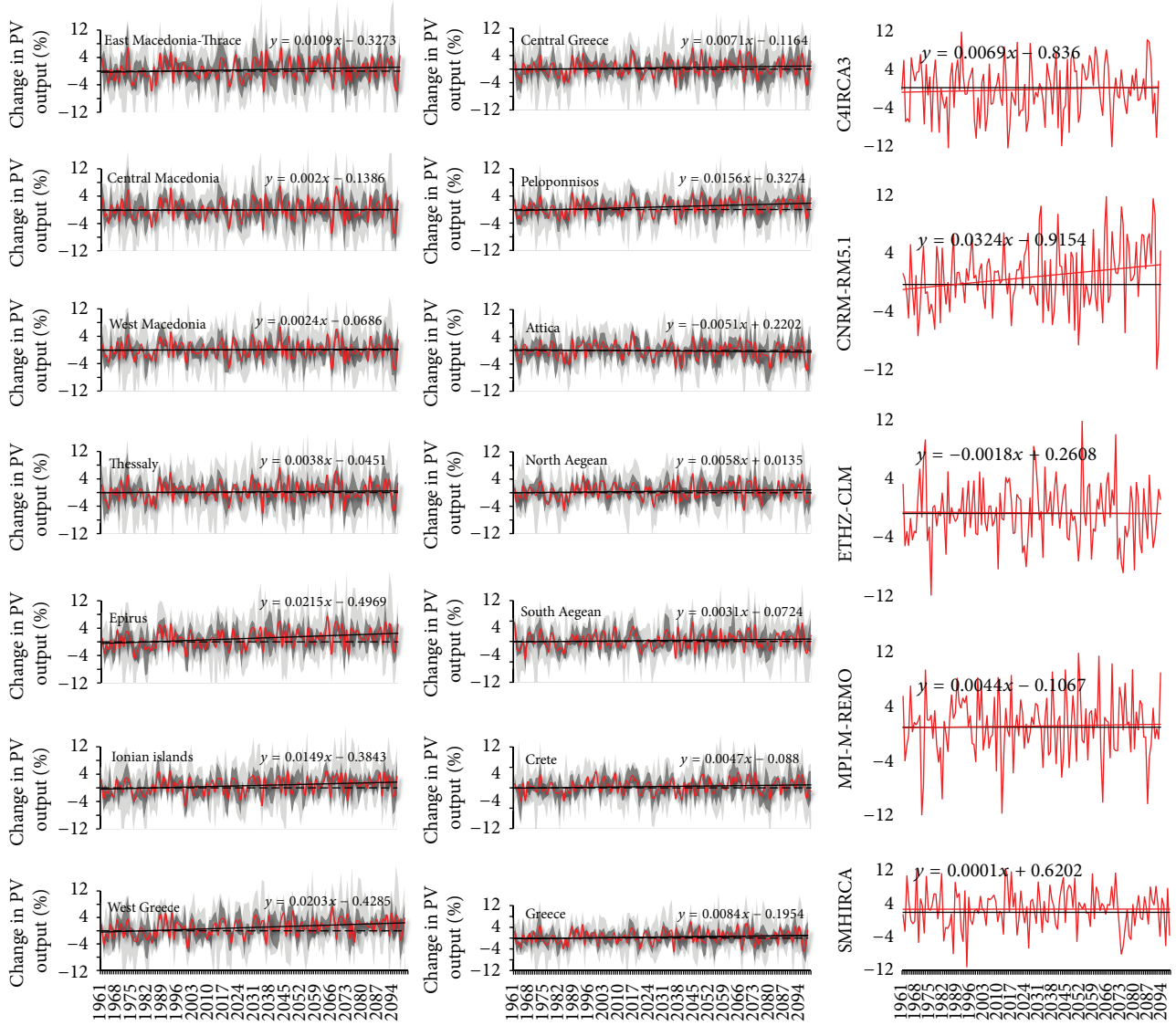


FIGURE 5: Relative change in PV output for the 13 prefectures of Greece and for the entire Greek region (left and center). Red line shows the average change of all models, dark grey represents the 50% range of the values of all RCMs, and light grey shows the 100% range of the models. Subplots in the right are the ensemble mean of each RCM for entire Greek region. The relative change is estimated using the 1960–2000 as baseline period.

TABLE 1: Name, institute, driving GCM, and transient experiment period of each ENSEMBLES RCM used.

Acronym	Institute	Driving GCM	Duration
CAIRCA3 [17]	SMHI, Sweden	HadCM3Q16	1951–2100
ETHZ-CLM [18]	ETHZ, Switzerland	HadCM3Q0	1951–2099
MPI-M-REMO [19]	MPI, Germany	ECHAM5-r3	1951–2100
SMHIRCA [17]	SMHI, Sweden	BCM	1961–2099
CNRM-RM5.1 [20]	CNRM, France	APREGE_RM5.1	1950–2100

sites in Europe and 35 in Africa) between 1994 and 1997. The RMS error was found to be 35 W/m^2 (17%) for daily mean irradiance and 25 W/m^2 (12%) for monthly mean irradiance. However, the bias of HelioClim against the observations was found to be in overall less than 1 W/m^2 for the whole dataset.

The estimation of the change in P/V potential over Greece was conducted at NUTS2 spatial discretization level (NUTS: nomenclature of units for territorial statistics). Moreover, standard coefficients of monocrystalline silicon cells were considered for (2) and (3). For a monocrystalline silicon cell

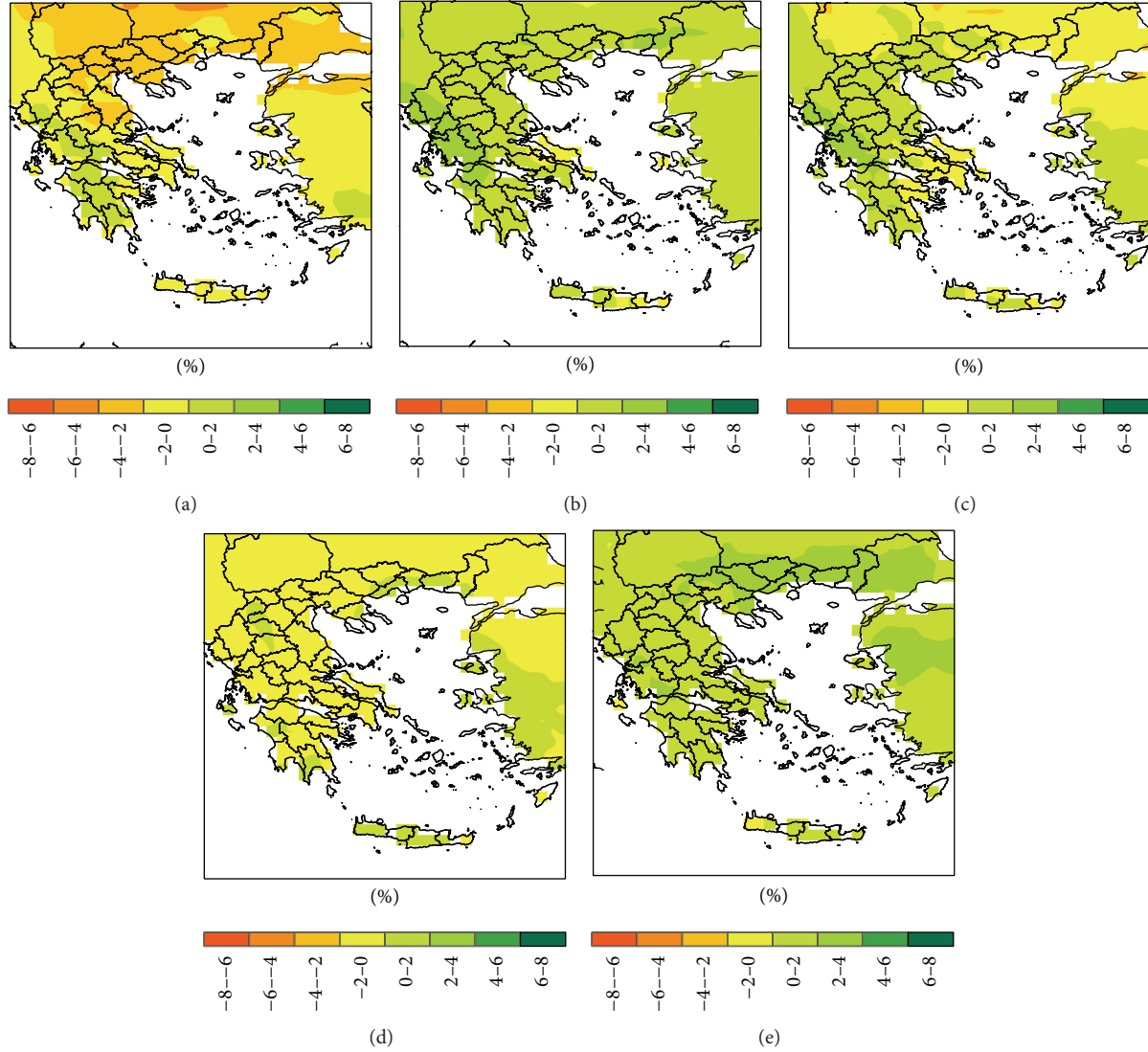


FIGURE 6: The first projection period (2011–2050) results in PV output change as it was estimated from each RCM ((a): C4I-RCA3, (b): CNRM–RM5.1, (c): ETHZ–CLM, (d): MPI-M-REMO, and (e): SMHI-RCA).

the coefficients are set according to Lasiner and Ang [27] as it is proposed in Crook et al. [10]. Thus, $\beta = 0.0045$, $\gamma = 0.1$, $c_1 = -3.75^\circ\text{C}$, $c_2 = 1.14$, and $c_3 = 0.0175^\circ\text{C m}^2 \text{W}^{-1}$. Typical value for the reference temperature is $T_{\text{ref}} = 25^\circ\text{C}$.

4. Results

4.1. Change in PV Energy Output. The change in PV energy output was estimated for two subsequent projection periods, 2011–2050 and 2061–2100. The periods 1950–2000 for temperature and 1985–2005 for irradiance were defined as control periods. Figure 1 presents the observed, the raw model ensemble mean, and the difference between them for temperature and irradiation. It was found that the RCM ensemble mean overestimates the mean temperature over Greek domain from 1°C to 3°C . This was also mentioned

in Boberg and Christensen [12]. Similarly, RCM data tend to heavily overestimate the irradiance over central parts of Greece with the overestimation to be as high as from 40 W/m^2 to 50 W/m^2 in some parts. However, over the southernmost part of Greece, RCMs represent better the mean irradiation. The difference between the observed and model values stresses the need of adjusting the bias in both the examined parameters. Figure 2 shows the change in RCM simulated mean irradiance and temperature for the three considered 40-year periods, after the adjustment of the bias. The relative change in mean for the two projected periods is also presented in Figure 3 compared to the control period. It is shown that in the first projection period (2011–2050) the mean increase ranges between 1 and 1.5°C , while by 2061–2100 period the increase range reaches up to 3 – 3.5°C for the most parts of the study area. Regarding irradiance the average increase for the first projection period ranges between 2

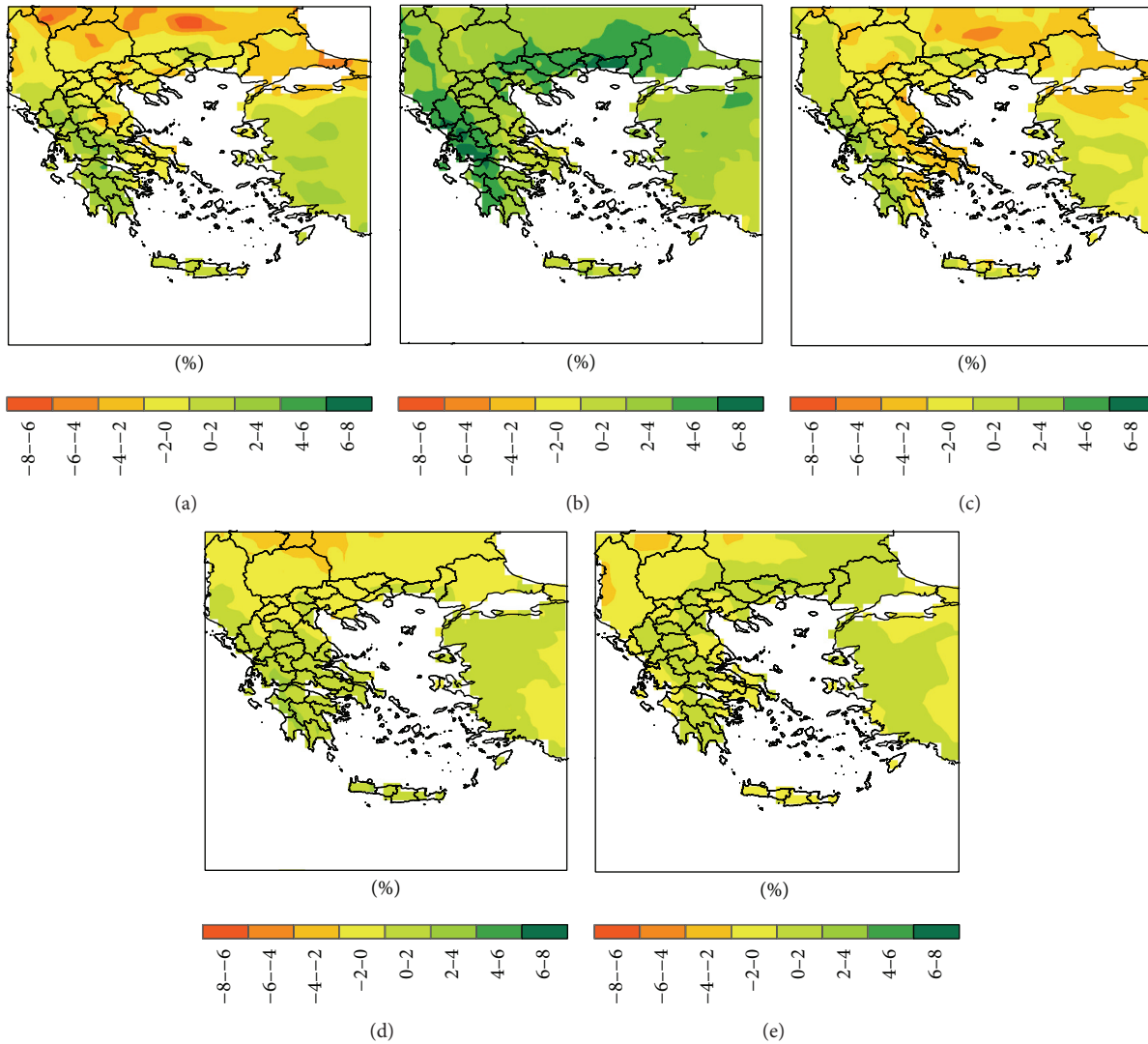


FIGURE 7: The second projection period (2061–2100) results in PV output change as it was estimated from each RCM ((a): C4I-RCA3, (b): CNRM–RM5.1, (c): ETHZ–CLM, (d) MPI-M REMO, and (e): SMHI-RCA).

and 3 W/m^2 while for the second period there is a further increase of $2\text{--}5 \text{ W/m}^2$. More specifically, the largest increase is expected over central Peloponnese and over Western Greece, in the regions of Epirus and Western Macedonia.

The change in PV energy output was then estimated for each model and projection period. Figure 4 illustrates the projected mean change in PV output derived from the ensemble of the RCMs. By 2050 the average PV energy output could increase up to 1%–2% in Western and Southwestern Greece, whereas for the regions of Attica and Thessaly a decrease of 1% is projected. However in the second period Western Greece and specifically the regions of Epirus and Peloponnese are projected to have an increase from 2% to 3%. For Thrace the respective increase is projected to be near 2%; in Northern Greece (Macedonia), Crete, and Aegean islands, the PV performance is expected to increase up to 1% while in the regions of Attica and Thessaly the projected performance decreases up from 1% to 2%.

Figure 5 illustrates the long term trend of the models ensemble relative projected change in PV energy output, for all administrative regions of Greece (NUTS 2 level) and for the entire study area. For all administrative regions, except Attica, a slight increasing trend in PV output is expected during the 21st century ranging between 0.2% and 2% in the regions of Western Greece and Epirus.

It is important to note that in Figure 5, the range of relative change from all models values is between $\pm 12\%$, which indicates the models' uncertainty. Referring to Crook et al. [10], the uncertainty in the specific research lies in the uncertainty of the projected changes in temperature and insolation. The most important source of uncertainty is the changes of cloud cover [28] and behavior as simulated in climate models, which plays an important role in climate change projections for the 21st century. For Southern Europe a decrease in cloud cover and increase in surface radiation are projected [10]. Therefore without the change in cloud cover

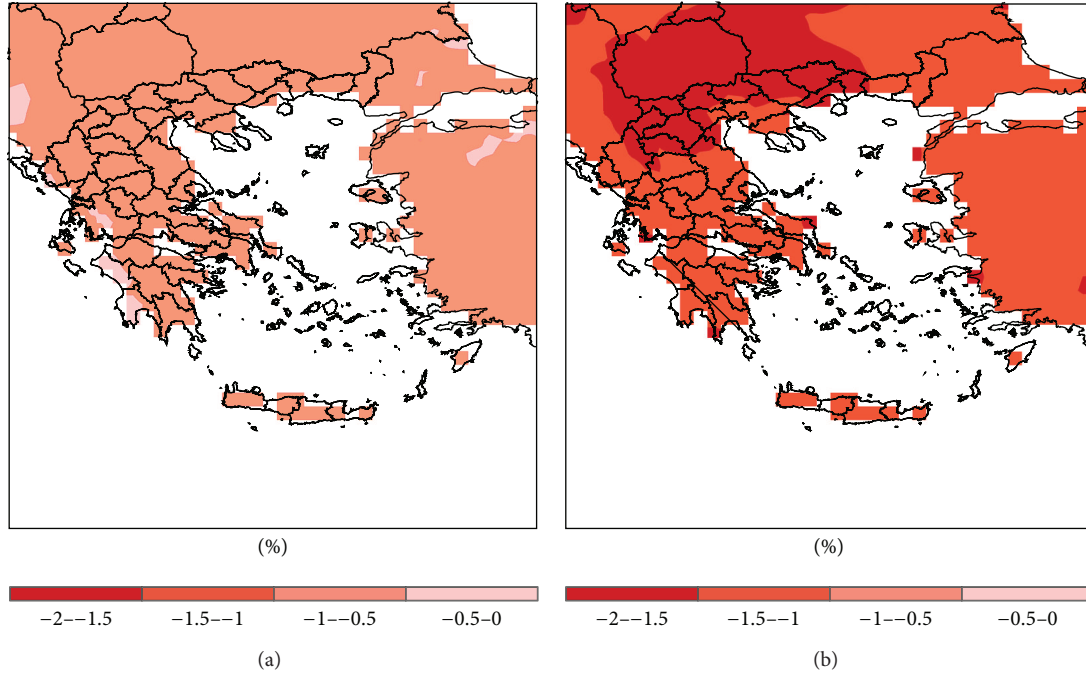


FIGURE 8: Temperature contribution to % PV output for 2011–2050 (a) and 2061–2100 (b) periods.

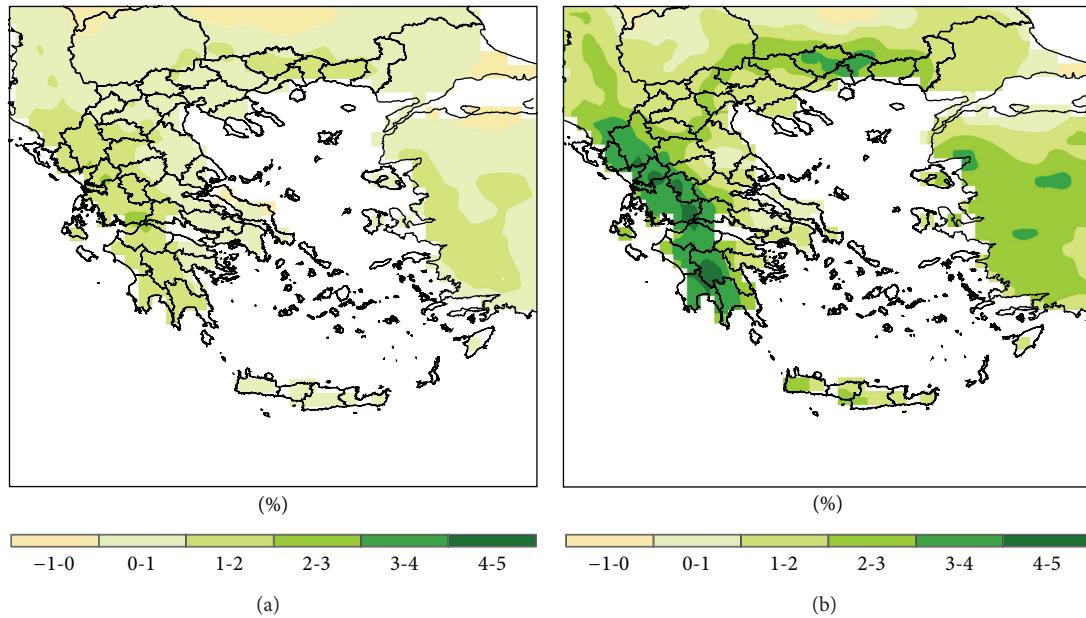


FIGURE 9: Irradiance contribution to % PV output for 2011–2050 (a) and 2061–2100 (b) periods.

the warming would still exist but not at this extent. Changes in cloud coverage influence the diurnal temperature variation [22] with greater influence on T_{max} during summer and T_{min} during winter than on the average daily temperature. This necessitates the distinctive consideration of T_{max} and T_{min} in climate change impact research. For Europe an increase in DTR (diurnal temperature range-temperature difference between maximum and minimum daily temperatures) is

projected with greater uncertainty in the local summer season variation [29].

Figures 6 and 7 present the percentage change of PV performance as derived from each RCM for 2011–2050 and 2061–2100 periods, respectively, compared to the RCMs outputs for the reference period. Results indicate that the signal of the projected change in average PV performance over Greece is robust with large spatial variability, however,

among the different RCMs. The majority of the RCMs project an increase between 1% and 2% over the most regions of the study area for the first period of study except from the RCM C4IRCA3 model which predicts a decrease up to 4% over the regions of Central and East Macedonia and the RCM MPI-M-REMO model which shows a decrease of about 2%. The projection for the second period indicates that, except for the RCM CNRM-RM 5.1 which shows a large increase, the rest of the RCM models predict an increase of the productivity of PV systems in the western mainland, Peloponnese, and Crete about 2%, while in the eastern mainland a decrease in productivity of about 2% and above is shown.

4.2. Contribution of Temperature and Insolation in the PV Output Change. The relative contributions of ΔT and ΔG are estimated by setting the projected change in irradiance and temperature, respectively, equal to zero in the calculations for the potential percentage change in the PV energy output in (2) following the methodology presented in Crook et al. [10]. In Figure 8, the ensemble mean PV output change is estimated for both projected periods, by setting the irradiance change equal to zero. In Figure 9 the respective results are presented by setting the temperature change equal to zero. The individual change in irradiance results in a significant increase on PV energy output up to 5% while the increase of temperature causes a decrease up to 2%. The relative contribution of each parameter varies from region to region. As it is expected, the two factors present different correlation signals with the PV output. In some cases the change in temperature and irradiance mutually compensates resulting in a small net change in performance. This is mostly the case in the first study period. However, there are cases such as the eastern part of Greece (Attica, Thessaly) where an increase in temperature of about 3°C–3.5°C cannot be compensated by the irradiation increase of about 1–3 W/m² and the estimation of PV energy output is negative, resulting in an overall reduction of PV output up to 3%. In contrast, over the Western Greece, despite the temperature increase at the same levels, the overall performance is expected to increase due to significant irradiation increase as a result of lower cloud coverage. Nonetheless, in some cases the large temperature increase cannot be compensated by the increase irradiance, as it can be observed in both study periods in eastern parts of the Greek mainland, some areas in Central Macedonia, and over Crete.

5. Conclusions

The projections of temperature and irradiance from 5 RCMs were analyzed for their contribution to monocrystalline PV panels' output change, over Greece. The analysis was conducted for two future periods, 2011–2050 and 2061–2100. The RCMs project an average temperature increase up to 1.5°C for the period 2011–2050 and from 3°C to 3.5°C for the period 2061–2100. Regarding the irradiance projections, an increase of 2–3 W/m² by 2011–2050 and up to 5 W/m² by 2061–2100 could be expected.

The PV output is projected to have an increasing trend for all regions of Greece during the 21st century. The region of Attica is an exemption where a reduction of 0.5% is projected. In the first period of study, an average increase between 1 and 2% in the majority of the study area is likely to occur except for the region of Attica and some areas in Thessaly and Central Macedonia. During the second period (2061–2100) a significant increase in the PV output is projected over the western mainland of Greece and Peloponnese, while a mild decrease for the eastern mainland and Central Macedonia is expected.

Examining the relative contributions of temperature and irradiance, a significant reduction due to the temperature increase is foreseen which is, however, outweighed by the irradiance increase, resulting in an overall increase in photovoltaic systems.

While the analysis shows clear increasing trends in the output of the monocrystalline PV systems over Greece, the rate of increase is small comparing to the variability amongst different RCMs. This is mainly attributed to the RCM shortcoming to robustly project the cloud cover and thus the irradiation parameter. The model's ability to capture the irradiation is expected to improve in the forthcoming Euro CORDEX [30].

Conflict of Interests

The authors declare that there is no conflict of interests regarding the publication of this paper.

Acknowledgments

The authors acknowledge the E-OBS dataset from the EU-FP6 project ENSEMBLES (<http://ensembles-eu.metoffice.com>) and the data providers in the ECA&D project (<http://www.ecad.eu>). The ENSEMBLES (<http://ensemblesrt3.dmi.dk/>) database provided the RCM data used in this study. The SoDa database (SoDa Contract DG "INFOS" IST-1999-12245) provided the observed irradiance data used. This research work was funded by the EU FP7 ECLISE project (Grant Agreement no. 265240).

References

- [1] EPIA, *Global Market Outlook for Photovoltaics 2013–2017*, European Photovoltaic Industry Association, 2013.
- [2] EPIA, *Connecting the Sun—Solar Photovoltaics on the Road to Large-Scale Grid Integration*, European Photovoltaic Industry Association, 2012.
- [3] M. Wild, A. Ohmura, and K. Makowski, "Impact of global dimming and brightening on global warming," *Geophysical Research Letters*, vol. 34, no. 4, Article ID L04702, 2007.
- [4] D. Aiguo, K. E. Trenberth, and T. R. Karl, "Effects of clouds, soil moisture, precipitation, and water vapor on diurnal temperature range," *Journal of Climate*, vol. 12, no. 8, pp. 2451–2473, 1999.
- [5] R. F. Cahalan, G. Wen, J. W. Harder, and P. Pilewskie, "Temperature responses to spectral solar variability on decadal time scales," *Geophysical Research Letters*, vol. 37, no. 7, 2010.

- [6] M. Mani and R. Pillai, "Impact of dust on solar photovoltaic (PV) performance: research status, challenges and recommendations," *Renewable and Sustainable Energy Reviews*, vol. 14, no. 9, pp. 3124–3131, 2010.
- [7] M. E. Meral and F. Diner, "A review of the factors affecting operation and efficiency of photovoltaic based electricity generation systems," *Renewable and Sustainable Energy Reviews*, vol. 15, no. 5, pp. 2176–2184, 2011.
- [8] F. Dincer and M. E. Meral, "Critical factors that affecting efficiency of solar cells," *Smart Grid and Renewable Energy*, vol. 1, pp. 47–50, 2010.
- [9] E. Skoplaki and J. A. Palyvos, "On the temperature dependence of photovoltaic module electrical performance: A review of efficiency/power correlations," *Solar Energy*, vol. 83, no. 5, pp. 614–624, 2009.
- [10] J. A. Crook, L. A. Jones, P. M. Forster, and R. Crook, "Climate change impacts on future photovoltaic and concentrated solar power energy output," *Energy and Environmental Science*, vol. 4, no. 9, pp. 3101–3109, 2011.
- [11] G. Notton, C. Cristofari, M. Mattei, and P. Poggi, "Modelling of a double-glass photovoltaic module using finite differences," *Applied Thermal Engineering*, vol. 25, no. 17–18, pp. 2854–2877, 2005.
- [12] F. Boberg and J. H. Christensen, "Overestimation of Mediterranean summer temperature projections due to model deficiencies," *Nature Climate Change*, vol. 2, no. 6, pp. 433–436, 2012.
- [13] J. Chen, F. P. Brissette, and R. Leconte, "Uncertainty of downscaling method in quantifying the impact of climate change on hydrology," *Journal of Hydrology*, vol. 401, no. 3–4, pp. 190–202, 2011.
- [14] J. O. Haerter, S. Hagemann, C. Moseley, and C. Piani, "Climate model bias correction and the role of timescales," *Hydrology and Earth System Sciences*, vol. 15, no. 3, pp. 1065–1079, 2011.
- [15] J. H. Christensen, F. Boberg, O. B. Christensen, and P. Lucas-Picher, "On the need for bias correction of regional climate change projections of temperature and precipitation," *Geophysical Research Letters*, vol. 35, no. 20, Article ID L20709, 2008.
- [16] W. Terink, R. T. W. L. Hurkmans, P. J. J. F. Torfs, and R. Uijlenhoet, "Bias correction of temperature and precipitation data for regional climate model application to the Rhine basin," *Hydrology and Earth System Sciences Discussions*, vol. 6, no. 4, pp. 5377–5413, 2009.
- [17] E. Kjellstrom, L. Barring, S. Gollvik et al., "A 140-year simulation of European climate with the new version of the Rossby Centre regional atmospheric climate model (RCA3)," SMHI Reports Meteorology and Climatology, 108, SMHI, SE-60176 Norrköping, Sweden, 2005.
- [18] U. Bohm, M. Kucken, W. Ahrens et al., "CLM—the climate version of LM: brief description and long-term applications," *COSMO Newsletter*, vol. 6, 2006.
- [19] D. Jacob, "A note to the simulation of the annual and inter-annual variability of the water budget over the Baltic Sea drainage basin," *Meteorology and Atmospheric Physics*, vol. 77, no. 1–4, pp. 61–73, 2001.
- [20] R. Radu, M. Déqué, and S. Somot, "Spectral nudging in a spectral regional climate model," *Tellus A: Dynamic Meteorology and Oceanography*, vol. 60, no. 5, pp. 898–910, 2008.
- [21] C. D. Hewitt and D. J. Griggs, "Ensembles-based predictions of climate changes and their impacts," *Eos*, vol. 85, no. 52, p. 566, 2004.
- [22] M. R. Haylock, N. Hofstra, A. M. G. Klein Tank, E. J. Klok, P. D. Jones, and M. New, "A European daily high-resolution gridded data set of surface temperature and precipitation for 1950–2006," *Journal of Geophysical Research D: Atmospheres*, vol. 113, no. 20, Article ID D20119, 2008.
- [23] S. Cros, D. Mayer, and L. Wald, "The availability of irradiation data," Report IEA-PVPS T2-04, International Energy Agency, Photovoltaic Power System Programme, Centre d'Énergetique, Ecole des Mines de Paris/Armines, Antipolis, France, 2004.
- [24] B. Gschwind, L. Ménard, M. Albuissou, and L. Wald, "Converting a successful research project into a sustainable service: the case of the SoDa Web service," *Environmental Modelling and Software*, vol. 21, no. 11, pp. 1555–1561, 2006.
- [25] C. Rigollier, M. Lefèvre, and L. Wald, "The method Heliosat-2 for deriving shortwave solar radiation from satellite images," *Solar Energy*, vol. 77, no. 2, pp. 159–169, 2004.
- [26] M. Lefèvre, L. Wald, and L. Diabaté, "Using reduced data sets ISCCP-B2 from the Meteosat satellites to assess surface solar irradiance," *Solar Energy*, vol. 81, no. 2, pp. 240–253, 2007.
- [27] F. Lasiner and T. G. Ang, *Photovoltaic Engineering Handbook*, Adam Higler, Princeton, NJ, USA, 1990.
- [28] K. E. Trenberth and J. T. Fasullo, "Global warming due to increasing absorbed solar radiation," *Geophysical Research Letters*, vol. 36, Article ID L07706, 2009.
- [29] D. B. Lobell, C. Bonfils, and P. B. Duffy, "Climate change uncertainty for daily minimum and maximum temperatures: a model inter-comparison," *Geophysical Research Letters*, vol. 34, no. 5, 2007.
- [30] D. Jacob, J. Petersen, B. Eggert et al., *EURO-CORDEX: New High-Resolution Climate Change Projections for European Impact Research Regional Environmental Change*, Springer, Berlin, Germany, 2013.

Research Article

WRF Model Methodology for Offshore Wind Energy Applications

Evangelia-Maria Giannakopoulou and Regis Nhili

EDF Energy R&D UK Centre, 52 Grosvenor Gardens, London SW1W 0AU, UK

Correspondence should be addressed to Evangelia-Maria Giannakopoulou; marilia.giannakopoulou@edfenergy.com

Received 6 February 2014; Accepted 24 March 2014; Published 23 April 2014

Academic Editor: Huei-Ping Huang

Copyright © 2014 E.-M. Giannakopoulou and R. Nhili. This is an open access article distributed under the Creative Commons Attribution License, which permits unrestricted use, distribution, and reproduction in any medium, provided the original work is properly cited.

Among the parameters that must be considered for an offshore wind farm development, the stability conditions of the marine atmospheric boundary layer (MABL) are of significant importance. Atmospheric stability is a vital parameter in wind resource assessment (WRA) due to its direct relation to wind and turbulence profiles. A better understanding of the stability conditions occurring offshore and of the interaction between MABL and wind turbines is needed. Accurate simulations of the offshore wind and stability conditions using mesoscale modelling techniques can lead to a more precise WRA. However, the use of any mesoscale model for wind energy applications requires a proper validation process to understand the accuracy and limitations of the model. For this validation process, the weather research and forecasting (WRF) model has been applied over the North Sea during March 2005. The sensitivity of the WRF model performance to the use of different horizontal resolutions, input datasets, PBL parameterisations, and nesting options was examined. Comparison of the model results with other modelling studies and with high quality observations recorded at the offshore measurement platform FINO1 showed that the ERA-Interim reanalysis data in combination with the 2.5-level MYNN PBL scheme satisfactorily simulate the MABL over the North Sea.

1. Introduction

The offshore wind energy has recently become a rapidly growing renewable energy resource worldwide, with several offshore wind projects in development in different planning stages [1, 2]. Despite this, a better understanding of the interaction between the MABL and the offshore wind turbines is needed in order to contribute to a better energy capture and cost-effectiveness [2]. The MABL is less studied than the planetary boundary layer (PBL) over land and some obvious reasons are the difficulties, scarcity, and costs of obtaining offshore observations. However, during the last years a great effort has been made in finding solutions [3]. For example, mesoscale meteorological models are increasingly considered lately for wind energy assessment and yield calculations. The advantage of the mesoscale models in WRA relies on their ability to simulate with reasonable accuracy the lower parts of the boundary layer, including important atmospheric properties such as the atmospheric energy balance and stability [4]. However, the usage of any mesoscale model

for wind energy applications requires a proper validation process to understand the accuracy and limitations of the model.

The impact of the atmospheric stability on the wind and turbulence profiles and on the wind turbine wakes raises the need to consider in the WRA of an offshore wind farm the stability conditions observed in the MABL [5, 6]. Different stability conditions result in different shear conditions which in turn lead to different wind speed distributions across the rotor swept area. The different velocity distributions can significantly affect the power production and fatigue loads on the wind turbine [7]. For example, it is well known that wind power losses, as a result of wake losses, are largest in stable atmospheric conditions and least in unstable and/or neutral conditions [6]. Therefore, a precise estimation of the wind and stability conditions of an offshore site is required. Currently, stability is not measured in traditional WRA campaigns and more accurate WRA could be obtained if the wind climate is classified not only by wind direction but also by stability classes.

In the mesoscale models the vertical stratification is inherently included and the different PBL schemes influence the accuracy of the simulated winds and atmospheric stratification in the MABL [8]. For instance, some PBL parameterisations are best in unstable/neutral stratifications, some others are best in stable atmospheric conditions, and some in both [3]. It is also widely known that the performance of the PBL schemes in the mesoscale models depends on the area of interest, the meteorological variables examined, and season and time of day considered, and one cannot identify a best model configuration in a general sense [9]. The most common approach to deal with this problem is to carry out statistical studies over a sensible set of model configurations and finally use the PBL scheme that reproduces better the observations in an average sense.

The attention of this study has been focused on the development of a mesoscale methodology by using the weather research and forecasting (WRF) model [10] so as to accurately simulate the wind conditions and to reproduce the stability effects on the wind profile over the MABL in the North Sea. The present work describes the verification of the WRF model, by comparing the model results with that of other modelling studies (e.g., [8, 11]) and with high quality observations recorded at the FINO1 offshore platform in the North Sea. For this verification process, several WRF modelling simulations have been performed during March 2005. In particular, different horizontal resolutions, PBL parameterizations, initial and boundary conditions, and nesting options were tested. The high probability (20%) of occurrence of stable to very-stable atmospheric stratification situations in the spring and early summer at the FINO1 platform and the impact of the high stability on the wind profile increases the need to focus on the stable atmospheric conditions and include them in our WRF model configuration and mesoscale methodology [3, 5]. A time period during which all the atmospheric stability conditions are observed are also investigated in this study.

A description of the verification process including information about the data sources and the statistics used for analysis is given in Section 2.1. Section 2.2 focuses on the WRF model setup and the process followed for testing its performance. Description of the synoptic conditions during the stable period in March 2005 and presentation of the WRF results for this case study with a number of key derived statistics are provided in Section 3. In the same section, presentation of the WRF results for the whole March 2005 with statistical metrics and error analysis is also given. Conclusions follow in Section 4.

2. Materials and Methods

2.1. Verification Process. Two main steps of the verification process are the definition of the data sources and the definition of the verification statistics to be produced by the analysis.

2.1.1. Observational Data: FINO1 Measurements. The FINO1 offshore platform in Southern North Sea is located 45 km north of the Borkum island (latitude: 54.0°N and longitude:

6.35°E) and performs multilevel measurements of wind speed, wind direction, air temperature, relative humidity, and air pressure since 2004. The height of the measurement mast is about 100 m above mean sea level (MSL). Three ultrasonic instruments (of 10 Hz temporal resolution) are located at 41.5 m, 61.5 m, and 81.5 m height on northwesterly oriented booms. In addition, eight cup anemometers with the lower resolution of 1 Hz are installed at different heights starting from 34 m upto about 100 m (every 10 m) on booms mounted in southeast direction of the meteorological mast (e.g., [8, 11]).

A list of parameters used for the analysis of the meteorological conditions and for the comparison with the WRF model results is shown in Table 1. In Table 1, we also provide the heights of the recorded parameters and the sensor types including their accuracy according to Cañadillas [6]. For the WRF model validation we used data from the cup anemometers in order to have the best spatial coverage to describe the vertical profiles of wind speed and wind direction. According to Deutsches Windenergie-Institut (DEWI, German Wind Energy Institute) scientists at the RAVE 2012 conference [12], the sonic anemometer data were sparse and were associated with errors especially during the period 2004–2007. In general, from 2004 to 2011 the availability of the cup anemometers at the FINO1 platform was about 98%, while the availability of the sonic anemometers was approximately 83% [12].

2.1.2. Define Verification Statistics. The following statistical metrics have been used in this study to verify the performance of the WRF model when compared with the FINO1 observations. More details on the verification statistics could be found in [13].

Bias or mean error (ME) is defined as the mean of the differences between the WRF simulated meteorological parameters and the FINO1 observations. In particular, the mean error is calculated for each hour of data and the time average (over the period we have considered to study) bias is then provided for each measuring height of the FINO1 platform.

Mean absolute error (MAE) is defined as the quantity used to measure how close the observed values are to the modelled ones. The MAE is given by

$$\text{MAE} = \frac{1}{n} \sum_{i=1}^n |x_i - y_i|, \quad (1)$$

where $|x_i - y_i|$ is the absolute error with x_i and y_i to represent the modelled and the observed values at the FINO1 met mast, respectively. n is the sample size.

Standard Deviation (STD) of the ME is defined as the dispersion of the biased values around the mean value. A low standard deviation indicates that the data points tend to be very close to the mean; high standard deviation indicates that the data points are spread out over a large range of values. The STD uses the following formula:

$$\sigma = \sqrt{\frac{\sum_{i=1}^n (x_i - \bar{x})^2}{(n - 1)}}, \quad (2)$$

where σ is the standard deviation and \bar{x} is the sample mean.

TABLE 1: Meteorological parameters with their associated heights and the sensor types including their accuracy [6] at the FINO1 offshore platform.

Variable	Heights (m) LAT	Sensor type (accuracy)
Wind speed (m/s) (cup anemometer)	34, 41.5, 51.5, 61.5, 71.5, 81.5, 91.5, 104.5	Vector A100LK-WR-PC3 (± 0.01 m/s)
Wind direction (degree)	41.5, 51.5, 61.5, 71.5, 81.5, 91.5	Thies wind vane classic ($\pm 1^\circ$)
Air temperature ($^\circ\text{C}$)	30, 41.5, 52, 72, 101	Pt-100 (± 0.1 K at 0°C)
Relative humidity (%)	34.5, 90	Hydrometer, Thies ($\pm 3\%$ RH)
Air pressure (hPa)	22.5	Barometer, Vaisala (± 0.03 hPa)

Root Mean Square Error (RMSE) is a frequently used measure of the difference between values predicted by a model and the values actually observed. It measures the average magnitude of the error and it is defined as the measure of the combined systematic error (bias) and random error (standard deviation). Therefore, the RMSE will only be small when both the variance and the bias of an estimator are small. The RMSE uses the following formula:

$$\text{RMSE} = \sqrt{\sigma^2 + \bar{x}^2}, \quad (3)$$

where \bar{x} is the sample mean and σ is the standard deviation.

Pearson correlation coefficient (R) is defined as the measure of the linear dependence between the WRF results and the FINO1 data, giving a value between +1 and -1 inclusive. It thus indicates the strength and direction of a linear relationship between these two variables. A value of 1 implies that a linear equation describes the relationship between WRF and the observations perfectly, with all data points lying on a line for which the WRF values increase as the data values increase. The correlation is -1 in case of a decreasing linear relationship and the values in between indicates the degree of linear relationship between the WRF model and the observations. The formula for the Pearson product moment correlation coefficient is

$$R = \frac{\sum_{i=1}^n (x_i - \bar{x})(y_i - \bar{y})}{\sqrt{\sum_{i=1}^n (x_i - \bar{x})^2 (y_i - \bar{y})^2}}, \quad (4)$$

where the \bar{x} and \bar{y} are, respectively, the sample means of the WRF results and the measurements.

2.2. Model and Setup. In this study, the numerical weather prediction (NWP) model of the National Centre for Atmospheric Research (NCAR): advanced WRF model, version 3.4 [10] was used. The model was run for this project on a Xeon X54 system at EDF R&D in France, with 96 CPUs. The WRF model is based on the fully compressible, nonhydrostatic Euler equations and for the purposes of this research the Lambert conformal projection was chosen. A third order Runge-Kutta (RK3) integration scheme and Arakawa C-grid staggering were used for temporal and spatial discretization, respectively. The modelling setup including the selected domains and the initial and boundary conditions as well as the physics schemes is described below. The strategy followed for the WRF modelling setup followed up to a certain point the strategy of previous WRF studies (e.g., [14, 15]).

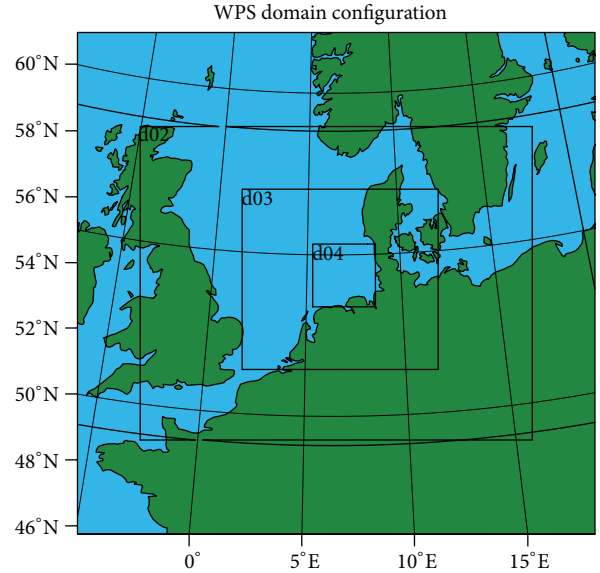


FIGURE 1: WRF modelling domain: 27 km (d01), 9 km (d02), 3 km (d03), and 1 km (d04) grid spacing.

Domain Setup. The WRF model was run in a series of two-way nested grids (centred in the FINO1 offshore platform at latitude: 54.0°N and longitude: 6.35°E). The horizontal grid spacing was refined by a factor of 3 through three nested domains until 1 km resolution. In particular, the WRF model was built over a parent domain (d01) with 67×65 horizontal grid points at 27 km, an intermediate nested domain (d02) of 9 km spatial resolution (151×121 grid points), and two innermost domain (d03) with 3 km spacing (217×205 grids) and 1 km spacing of 202×190 grids (see Figure 1). On the vertical coordinate, 88 vertical levels were used. The vertical resolution was 10 m upto 200 m height to accurately resolve the lower part of the MABL. Above 200 m, grid spacing is progressively stretched.

Initial and Boundary Conditions. The WRF model was used to refine the state of the atmosphere, especially the PBL, by downscaling both the global NCEP final analysis (FNL) data and the Era-Interim reanalysis data produced by the ECMWF. The NCEP FNL data have horizontal resolution of 1×1 degree (~ 100 km) and 52 model levels. The Era-Interim reanalysis project covers the period from 1979 to present and has a spectral T255 horizontal resolution (~ 79 km spacing on a N80 reduced Gaussian grid) and 60 vertical model levels

[16]. The time step was set equal to 120 seconds to fulfil the Courant-Friedrichs-Lewy (CFL) condition for horizontal and vertical stability and the first 24 hours were discarded as spin-up time of the model.

Topographic Inputs. For the WRF the topographic information was developed using the 20-category moderate resolution imaging spectroradiometer (MODIS) WRF terrain database. The 27 km domain was based on the 5 minutes (~9.25 km) global data, the 9 km domain was based on the 2 minutes (~3.70 km) data, and the 3 km and 1 km domains were based on the 30 seconds (~900 m) data.

Four-Dimensional Data Assimilation (FDDA). Nudging is one method of FDDA that is implemented in the WRF model. The WRF model supports three types of nudging: the three-dimensional upper-air and/or surface analysis, the observation, and the spectral nudging. Because the purpose of the stable case study was mainly to perform the sensitivity experiments rather than to keep the simulations close to the reanalysis and measurement data, the WRF model was run without analysis and observation nudging for this stable period. When the model was run for the whole March 2005, analysis nudging was configured to nudge temperature, water vapour, mixing ratio, and horizontal wind components on the outermost domain (d01) with time intervals of six hours. The strategy followed for analysis nudging was based on previous studies [17].

Physics Schemes. Microphysics was modelled using the new Thompson scheme with ice, snow, and graupel processes suitable for high-resolution simulations. The rapid radiative transfer model (RRTM) (an accurate and widely used scheme using look-up tables for efficiency) and the Dudhia (a simple downward integration allowing for efficient cloud and clear-sky absorption and scattering) schemes were used for the longwave and shortwave radiation options, respectively. The Noah land surface model (LSM) was chosen to simulate soil moisture and temperature and canopy moisture. Finally, the cumulus physics was modelled with the Grell 3D scheme, which is an improved version of the Grell-Devenyi (GD) ensemble scheme that can be used on high resolution (in addition to coarser resolutions). However, the cumulus parameterization was turned off in the fine-grid spacing of 3 km and 1 km selected for these simulations. Theoretically, it is only valid for parent grid sizes greater than 9 km [10]. Finally, four PBL schemes were selected for this study. These include two turbulent kinetic energy (TKE) closure schemes, the Mellor-Yamada-Janjic (MYJ) PBL [18] and the Mellor-Yamada Nakanishi and Niino Level 2.5 (MYNN) PBL [19] and two first-order closure schemes, the Yonsei University (YSU) PBL [20] and the asymmetric convective model version 2 (ACM2) [21]. More details of the model, of the physics schemes and references, could be found in [10].

3. Results and Discussion

3.1. Stable Period (16–18 March 2005). In this section, WRF model results are presented and compared with other modelling studies and with high quality observations recorded at

the FINO1 offshore platform in the North Sea. The model validation is for stable atmospheric conditions during March 2005. According to Krogsæter [3] and Saint-Drenan et al. [5], at the FINO1 offshore platform stable atmospheric conditions are observed 20% of the time during spring and early summer. It is well known that the mesoscale models handle both high atmospheric stability and high instability with difficulty due to their PBL schemes. The stable MABL is very complex and its structure is more complicated and variable than the structure of the unstable/neutral MABL [22]. Stable atmospheric conditions are mainly observed during the night and it is well known that the nocturnal boundary layer is driven by two distinct processes: low turbulence and radiative cooling which both are very difficult to describe and to model. Therefore, making precise offshore wind resource maps under stable conditions is a great challenge. For the representative case of the stable MABL, the period from 16 to 18 March 2005 at 00:00 UTC was selected for analysis. Similar studies have been performed in the past for this particular time period and we could therefore compare our methodologies and results with that of other researches (e.g., [8, 11]).

During the stable period, the synoptic situation over the North Sea is determined by a low-pressure system over the Atlantic and a high-pressure system over the southern Europe, which later in the examined period shifts to the north-west [11]. In Figure 2, we present the temporal variation of the wind and temperature conditions at the FINO1 offshore platform during the stable period. As can be seen in Figure 2, at the beginning of the period very strong southwesterly (~210–240°) winds dominate the area, which later become westerlies (~270°) and slow down. It can be assumed that the MABL structure over the North Sea is influenced by large scale circulations, since no diurnal variation is observed in the air temperature and wind speed. According to Sušelj and Sood [11], the MABL structure over the North Sea is primarily established by the properties of advected air masses and has small or almost no diurnal cycle. For example, at the FINO1 platform mainly during the winter, the southwesterlies to westerlies advect warm air over the cold sea, resulting in a stable MABL, while north-westerlies to north-easterlies advect cold air, resulting in an unstable MABL. In general, we could characterise the period 16–18 March 2005 as a two-day stable period with the air temperature higher than the water temperature and with high wind speeds (see Figure 2). Actually, the FINO1 recordings gave even a 5°C difference between the air and the water temperature at the night of 16 March 2005, corresponding closely to stable conditions. Considering the air-water temperature difference is a very simple and pragmatic method of describing the stability conditions. In the current study, this method was shown to be sufficiently precise. In addition, the Richardson number has been also calculated to confirm the stability conditions.

To determine the atmospheric stability, the Richardson number has been calculated using the WRF model outputs. The Richardson number quantifies the respective contribution of the wind shear and the buoyancy to the production

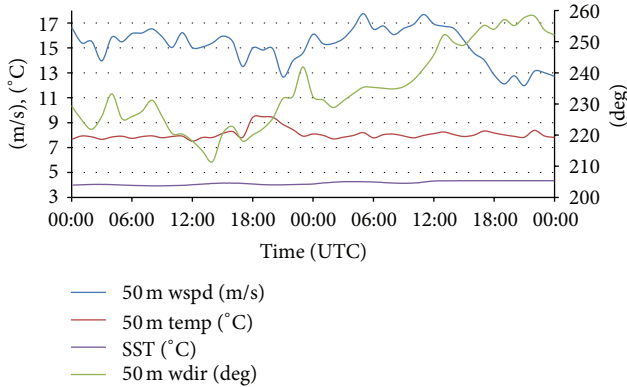


FIGURE 2: Temporal variation of the sea-surface temperature (SST), air temperature ($^{\circ}\text{C}$), wind speed (m/s), and wind direction (degree) at 50 m height, as these were recorded at the FINO1 platform for the stable period 16–18 March 2005 at 00:00 UTC. Temperature and wind speed are represented in the left y-axis and the wind direction in the right y-axis of the plot.

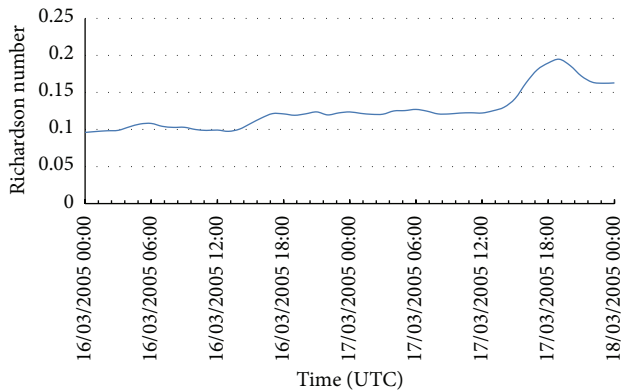


FIGURE 3: Temporal variation of the Richardson number, as this was calculated for the stable period 16–18 March 2005 at 00:00 UTC.

of turbulent kinetic energy [5] and the equation used in the computation of the Richardson number was

$$\text{Ri} = \frac{g (\theta_1 - \theta_2) (z_1 - z_2)}{\theta_1 (u_1 - u_2)^2}, \quad (5)$$

where g is the gravitational acceleration, u_1 , u_2 , θ_1 , and θ_2 are the wind speed and the virtual potential temperature at the height z_1 and z_2 , respectively [23].

It is worth noting that negative Richardson numbers indicate unstable conditions; positive values indicate statically stable flows and values close to zero or zero are indicative of neutral conditions. As an example, the Richardson number is plotted in Figure 3 for the period 16–18 March 2005. The positive values of the Richardson number (varying from 0.1 to 0.2) confirm the statically stable flows that dominated during this particular time period.

3.1.1. Sensitivity to Horizontal Resolution. Increasing the horizontal resolution in the mesoscale models increases the ability of the models to resolve major features of the topography

TABLE 2: Statistical metrics (MAE in m/s, ME in m/s, STD of the ME in m/s, and R) for the 100 m wind speed, so as to evaluate the performance of different horizontal resolutions (3 km versus 1 km).

At 100 m	MAE (m/s)	ME (m/s)	STD (m/s)	R
1 km—ERA-I	2.45	-2.31	1.58	0.62
3 km—ERA-I	2.38	-2.27	1.47	0.66

and surface characteristics, such as the coastal boundaries and therefore produces more accurate wind climatologies [4]. Generally speaking, the higher the resolution of the simulation, the better the representation of the atmospheric processes we obtain [24], especially if the terrain is complex [4]. However, it is difficult to define a priori the grid spacing needed to achieve a desired level of accuracy. The sensitivity to horizontal resolutions is thus tested in this section to define optimum grid spacing. For the runs, the ERA-Interim reanalysis was selected to initialise the model and the YSU scheme to model the MABL.

To evaluate the performance of the different horizontal resolutions, four statistical parameters were used: mean absolute error (MAE), mean error (ME), standard deviation (STD) of the ME, and correlation coefficient (R). As an example, statistical metrics for the 100 m wind speed are shown in Table 2 for the 3 km and 1 km spacing. It seems that the 3 km horizontal resolution results in a slight reduction of MAE, bias, and STD and improves correlations with the observations compared to what has been simulated at the 1 km spacing. We concluded that the 3 km is the optimal resolution and that the finest 1 km spacing does not bring improvement in the WRF results worth considering. It seems that the parameterizations used in the WRF model impose a limit to the downscaling, beyond which there is a minor or any improvement of the model performance. According to Talbot et al. [25], it is beneficial to use very fine horizontal resolution (≤ 1 km) during stable atmospheric conditions and over heterogeneous surfaces when local properties are required or when resolving small-scale surface features is desirable. In this modelling study, the North Sea can be characterised as a homogeneous surface and therefore there is no advantage of using the computationally expensive 1 km spacing (as the model resolution increases more computer processing required). It is worth noting that similar results to the one presented in this section were obtained for all the vertical levels below 100 m.

3.1.2. Sensitivity to Input Data. The impact of using different reanalysis datasets on the initialisation of the WRF model is investigated in this section. Comparing the model results when the ERA-Interim and the NCEP data were used at the 3 km horizontal resolution and with the YSU PBL scheme, it is found that the simulated winds are better correlated with the FINO1 observations and have lower STD and MAE when the ERA-Interim dataset is used (see Table 3). On average over all the vertical levels the ERA-Interim dataset yields 0.91 m/s lower wind speeds than recorded, 1.17 m/s STD, and correlation between the model and the measurements equal 0.77.

TABLE 3: Statistical metrics (MAE in m/s, ME in m/s, STD of the ME in m/s, and R) for wind speed at 8 vertical levels (30–100 m), so as to evaluate the performance of different input datasets (NCEP versus ERA-Interim) at the 3 km WRF modelling domain.

	30 m	40 m	50 m	60 m	70 m	80 m	90 m	100 m	Average
NCEP FNL and YSU PBL									
MAE (m/s)	1.09	1.09	1.06	1.23	1.44	1.94	2.20	2.40	1.56
ME (m/s)	0.51	0.44	-0.25	-0.75	-1.1	-1.8	-2.07	-2.33	-0.92
STD (m/s)	1.35	1.37	1.39	1.41	1.42	1.42	1.42	1.57	1.42
R	0.63	0.62	0.62	0.62	0.62	0.62	0.63	0.59	0.62
ERA-I and YSU PBL									
MAE (m/s)	0.89	0.90	0.88	1.07	1.29	1.84	2.10	2.38	1.42
ME (m/s)	0.46	0.39	-0.23	-0.74	-1.09	-1.75	-2.05	-2.27	-0.91
STD (m/s)	1.01	1.05	1.10	1.14	1.18	1.21	1.23	1.47	1.17
R	0.81	0.80	0.79	0.78	0.77	0.76	0.75	0.66	0.77

TABLE 4: A synopsis of the WRF model configuration used by EDF R&D for the stable period: 16–18 March 2005.

Simulation period	15–20/03/2005, 00:00 UTC
Model version	V3.4
Domains	4
Horizontal resolution	27, 9, 3 and 1 km
Grid sizes	67 × 65, 151 × 121, 217 × 205 and 202 × 190
Vertical resolution	88 (eta levels)
Input data	ERA-Interim
Time step	120 s
Outputs frequency	180, 180, 60 and 60 minutes
Gridded analysis nudging	NO
Nesting	2-way nesting
Physics schemes	
Microphysics	New Thompson
Cumulus	Grell 3D
Shortwave	Dudhia
Longwave	RRTM
LSM	Noah
PBL	YSU, MYNN, MYJ, ACM2

Note that in both experiments with different input data an increased MAE with the elevation is observed and the WRF model is found to overestimate the winds below 40 m and underestimate them above that height. It is also observed that the correlations slightly decrease and the bias continues to increase as the altitude increases; this trend in the mean error and correlation coefficient with the increasing height is an indication that the current model configuration needs further improvement. It seems that this decreasing trend is more pronounced when the ERA-Interim data were used, but the average results (considering the average statistical metrics: correlation, bias, STD, and MAE) were closer to the observations with this dataset. As will be shown later, these reduced correlations with increasing height are a result of several factors including the input data and mainly the PBL scheme.

3.1.3. Sensitivity to PBL Schemes. It is well accepted that the accuracy of the simulated, by the mesoscale models, offshore winds is strongly affected by the PBL schemes [26]. Therefore, a way to improve the WRF performance at the lower levels of the atmosphere is to try different PBL parameterisations. The behaviour of four different PBL schemes (YSU, MYJ, MYNN, and ACM2) on the stable MABL is examined and the importance of defining the appropriate model setup for studying pure offshore wind conditions is noticed in this section. The PBL experiment was run four times; one run for each PBL scheme. A synopsis of the model configuration is given in Table 4.

Statistical metrics (MAE, ME, STD, and R) for the wind speed at heights from 30 m upto 100 m are presented in Table 5. Note that the MYNN PBL scheme predicts lower values of MAE and ME in all vertical levels than the other PBL schemes. It seems that the MYNN scheme is the one that yields to the highest degree of correctness mainly above 50 m and thus showing in average the best agreement with the FINO1 observations. It is also noticed that the bias between the WRF model and the measurements is lower and close to the surface for the YSU, MYJ, and ACM2 PBL runs, whereas the bias increases with altitude. The YSU run seems to correlate better with the FINO1 measurements than the other PBL schemes below 70 m, but above that height the ME significantly increases and lower values of correlation were found. On the other hand, the MYNN scheme performs almost with the same accuracy at all heights with low values of ME and STD. In particular, the MYNN scheme resulted (in average over all the heights) in 0.01 m/s higher wind speeds than measured, STD of 1.21 m/s, and correlation coefficient equal to 0.66 (see Table 5).

It is well known that the atmospheric stability has a significant effect on the vertical wind profile and on estimates of the wind resource at a given height [4]. A detailed analysis of the offshore vertical wind profile upto hub heights and above is important for a correct estimation of the MABL wind and stability conditions, wind resource, and power forecasting.

The time-averaged vertical profiles of wind speed, temperature, and wind direction for all the PBL runs are provided in Figure 4 for comparison with the FINO1 measurements.

TABLE 5: Statistical metrics (MAE in m/s, ME in m/s, STD of the ME in m/s, and R) for the wind speed at 8 vertical levels (30–100 m), so as to evaluate the performance of four PBL schemes (YSU, MYJ, ACM2, and MYNN) at the 3 km WRF modelling domain.

	30 m	40 m	50 m	60 m	70 m	80 m	90 m	100 m	Average
YSU PBL									
MAE (m/s)	0.89	0.90	0.88	1.07	1.29	1.84	2.10	2.38	1.42
ME (m/s)	0.46	0.39	-0.23	-0.74	-1.09	-1.75	-2.05	-2.27	-0.91
STD (m/s)	1.01	1.05	1.10	1.14	1.18	1.21	1.23	1.47	1.17
R	0.81	0.80	0.79	0.78	0.77	0.76	0.75	0.66	0.77
MYJ PBL									
MAE (m/s)	1.38	1.25	1.43	1.55	1.56	1.79	1.76	1.64	1.55
ME (m/s)	-1.03	-0.84	-1.12	-1.25	-1.23	-1.52	-1.46	-1.33	-1.22
STD (m/s)	1.24	1.23	1.24	1.27	1.32	1.36	1.39	1.43	1.31
R	0.68	0.67	0.67	0.66	0.64	0.63	0.63	0.65	0.65
ACM2 PBL									
MAE (m/s)	1.08	0.97	1.20	1.38	1.46	1.77	1.79	1.86	1.44
ME (m/s)	-0.74	-0.56	-0.91	-1.15	-1.23	-1.61	-1.64	-1.59	-1.18
STD (m/s)	1.13	1.13	1.15	1.17	1.18	1.20	1.21	1.41	1.20
R	0.67	0.66	0.65	0.63	0.61	0.61	0.60	0.56	0.62
MYNN PBL									
MAE (m/s)	0.91	0.92	0.88	0.91	0.93	1.00	0.99	1.03	0.95
ME (m/s)	0.12	0.38	0.16	0.01	0.03	-0.27	-0.21	-0.12	0.01
STD (m/s)	1.22	1.21	1.20	1.21	1.23	1.23	1.26	1.28	1.23
R	0.67	0.67	0.66	0.66	0.64	0.64	0.63	0.67	0.66

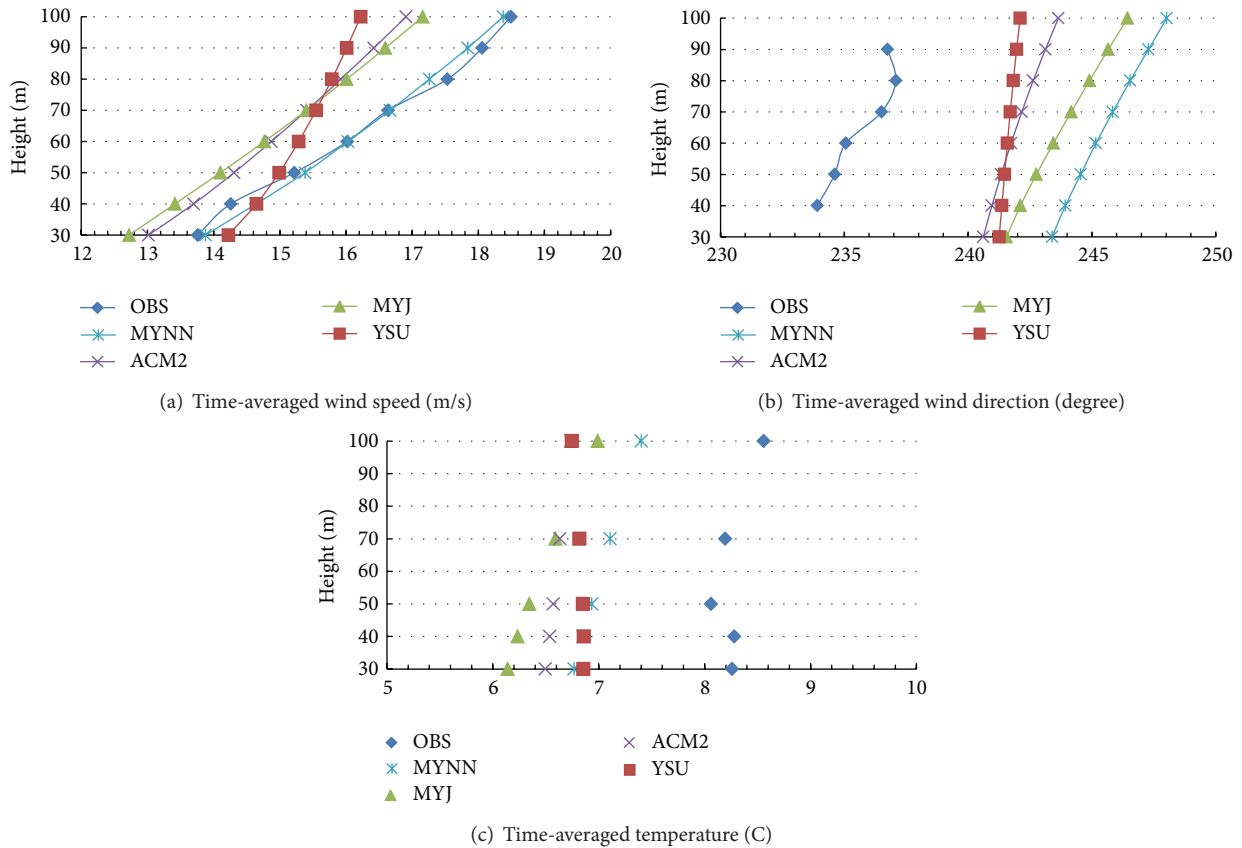


FIGURE 4: Time-averaged (16–18 March 2005) vertical profiles upto 100 m ASL for (a) wind speed (m/s), (b) wind direction (degree), and (c) temperature ($^{\circ}\text{C}$). The model results of different PBL schemes are compared with the FINO1 measurements.

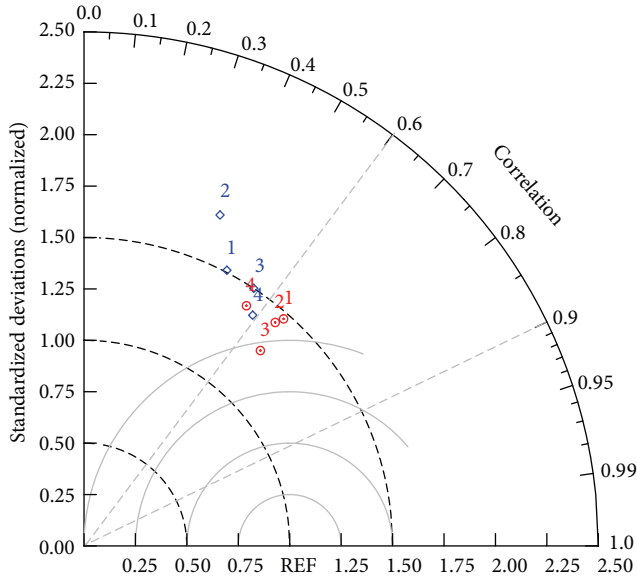


FIGURE 5: Taylor diagram displaying a statistical comparison with four WRF model estimates (YSU: 1, MYJ: 2, MYNN: 3, and ACM2: 4) of the wind speed during the stable period 16–18 March 2005. Red is the EDF statistics and blue is the Muñoz-Esparza et al. [8] statistics.

This kind of representation allows us to have some understanding about the behaviour of different PBL schemes in the lower levels of the MABL. The highly stable conditions observed during the examined period pose a particular challenge. As can be seen in Figure 4, the YSU scheme was in good agreement with the observed data at the 30 m height, but higher up underestimated the wind resource. This result highlights the importance of studying the whole MABL for offshore wind energy applications. Also, an increase in wind speed with increasing altitude is noticed at all PBL runs, but only the MYNN scheme produces wind speeds which are in exceptionally good agreement with the observations. It seems that the MYNN PBL scheme manages to model the correct amount of mixing in the boundary layer. The MYNN scheme is also shown to be the most consistent with the temperature measurements (approximately 1°C difference at 100 m height) and gives less than 10° difference in the wind direction at all vertical levels (see Figure 4).

Comparison with Other Modelling Studies. Muñoz-Esparza et al. [8] in their WRF modelling study for the stable period 16–18 March 2005 compared six different PBL schemes. Their model configuration is presented in Table 6.

Statistical metrics (ME, RMSE, and R) of the 100 m wind speed for the common PBL runs, as these were calculated by Muñoz-Esparza et al. [8] and by EDF, are shown in Table 7. Note that all PBL runs of this study result in a decreased bias and RMSE as well as in an increased correlation coefficient. The differences between EDF's and Muñoz-Esparza et al.'s [8] model setup, such as the input data, the number of the vertical levels, and in general the combination of physics schemes (e.g., microphysics and cumulus), may be a reason for the better accuracy in this study. For example, EDF initialised

TABLE 6: A synopsis of the WRF model configuration used by Muñoz-Esparza et al. [8] for the stable period: 16–18 March 2005.

Simulation period	14–18/03/2005, 00:00 UTC
Model version	V3.2
Domains	4
Horizontal resolution	27, 9, 3 and 1 km
Vertical resolution	46
Input data	NCEP
Gridded analysis nudging	NO
Nesting	2-way nesting
Physics schemes	
Microphysics	WSM3
Cumulus	Kain-Fritsch
Shortwave	Dudhia
Longwave	RRTM
LSM	Noah
PBL	YSU, MYJ, MYNN, ACM2, QNSE, BouLac

TABLE 7: Muñoz-Esparza et al. [8] versus EDF statistical metrics (ME in m/s, RMSE in m/s, and R) for the 100 m wind speed, so as to evaluate the WRF performance with different PBL schemes.

PBL schemes	[8]			EDF		
	ME (m/s)	RMSE (m/s)	R (—)	ME (m/s)	RMSE (m/s)	R (—)
YSU	−2.83	3.21	0.46	−2.27	2.70	0.66
MYJ	−1.93	2.60	0.38	−1.33	1.94	0.65
QNSE	−1.23	1.90	0.53	—	—	—
MYNN	−0.44	1.56	0.55	−0.12	1.28	0.67
ACM2	−1.61	2.13	0.59	−1.59	2.11	0.56
BouLac	−3.08	3.42	0.46	—	—	—

the model with the ERA-Interim data instead of the NCEP reanalysis and used 88 vertical levels instead of the 46 used by and Muñoz-Esparza et al. [8]. It is well expected that part of the problem with the simulation of stable conditions in the MABL is having enough vertical levels. A reason is the fact that a stable layer acts as an effective barrier to mixing and if the model layers at the lower levels of the MABL are widely spaced, the simulated barrier may be too weak [4].

Another important point seen in Table 7 is that both Muñoz-Esparza et al. [8] and EDF concluded that the best model performance was observed when the MYNN PBL scheme was selected and that the WRF model tends to underestimate the wind speed at the hub height. The similarities between the PBL experiments of Muñoz-Esparza et al. [8] and EDF are quantified in terms of their correlation, their RMSE, and their STD by using the Taylor diagram [27]. In particular, Figure 5 is a Taylor diagram which shows the relative skill with which the PBL runs of Muñoz-Esparza et al. [8] and EDF simulate the wind speeds during the stable period 16–18 March 2005. Statistics for four PBL runs (YSU: 1, MYJ: 2, MYNN: 3, and ACM2: 4) are used in the plot and the position

TABLE 8: Statistical metrics (MAE in m/s, ME in m/s, STD of the ME in m/s, and R) for the wind speed at 8 vertical levels (30–100 m), so as to evaluate the performance of one- and two-way nesting options at the 3 km WRF modelling domain.

	30 m	40 m	50 m	60 m	70 m	80 m	90 m	100 m	Average
MYNN and 2-way									
MAE (m/s)	0.91	0.92	0.88	0.91	0.93	1.00	0.99	1.03	0.95
ME (m/s)	0.12	0.38	0.16	0.01	0.03	-0.27	-0.21	-0.12	0.01
STD (m/s)	1.22	1.21	1.20	1.21	1.23	1.23	1.26	1.28	1.23
R	0.67	0.67	0.66	0.66	0.64	0.64	0.63	0.67	0.66
MYNN and 1-way									
MAE (m/s)	0.97	1.00	0.98	1.00	1.02	1.07	1.08	1.11	1.03
ME (m/s)	0.17	0.43	0.21	0.05	0.08	-0.22	-0.17	-0.07	0.06
STD (m/s)	1.28	1.28	1.28	1.30	1.33	1.34	1.36	1.40	1.32
R	0.64	0.63	0.62	0.61	0.59	0.59	0.58	0.62	0.61

of each number appearing on the plot quantifies how closely that run matches observations. If for example, run number 3 (MYNN PBL run) is considered, its pattern correlation with observations is about 0.67 for the EDF MYNN PBL experiment (red colour) and 0.55 for the Muñoz-Esparza et al. [8] MYNN PBL run (blue colour). It seems that the simulated patterns between EDF and [8] that agree well with each other are for the ACM2 PBL run (number 4) and the pattern that has relatively high correlation and low RMSE are for the EDF MYNN PBL run (red-number 3).

3.1.4. Sensitivity to Nesting Options. In the WRF model, the horizontal nesting allows resolution to be focused over a particular region by introducing a finer grid (or grids) into the simulation [10]. Therefore, a nested run can be defined as a finer grid resolution model run in which multiple domains (of different horizontal resolutions) can be run either independently as separate model simulations or simultaneously.

The WRF model supports one-way and two-way grid nesting techniques, where one-way and two-way refer to how a coarse and a fine domain interact. In both the one-way and two-way nesting options, the initial and lateral boundary conditions for the nest domain are provided by the parent domain, together with input from higher resolution terrestrial fields and masked surface fields [10]. In the one-way nesting option, information exchange between the coarse domain and the nest is strictly downscale, which means that the nest does not impact the parent domain's solution. In the two-way nest integration, the exchange of information between the coarse domain and the nest goes both ways. The nest's solution also impacts the parent's solution.

To this point, the best model performance was achieved with the following combination: Era-Interim as input and boundary data, 3 km as the optimal horizontal resolution, and the MYNN PBL scheme to simulate the MABL. In this section, both the one-way and two-way nesting options with the aforementioned model combination were tested so as to investigate how the different nesting options can affect the WRF performance.

It seems that the differences between the two-way and one-way nesting options are small. However, it can be concluded that the two-way nest integration produces on average

wind speeds closer to the FINO1 measurements (see Table 8). When the two-nesting option was selected, the average over all heights ME was 0.01 m/s and the STD of the ME was 1.23 m/s (instead of 0.06 m/s ME and 1.32 m/s STD for the one-way nesting option). As can be also seen in Table 8, the WRF model resulted in smaller MAE (averaged over all the heights) and correlated better with the observations when the two-way nesting option was selected. It is thus concluded that when the exchange of information between the coarse domain and the nest goes both ways, it results in better model performance.

3.1.5. Summary. The validation of the WRF model at the FINO1 met mast during the stable case study (16–18 March 2005) resulted in the following conclusions in terms of model configuration.

- (i) Selecting the finest horizontal resolution of 1 km instead of the 3 km does not bring improvement in the WRF results worth considering; it was very time consuming in terms of computational time.
- (ii) Using the ERA-Interim reanalysis data instead of the NCEP FNL data allows reducing the bias between simulated and measured winds.
- (iii) Changing PBL schemes has a strong impact on the model results. The MYNN PBL scheme was in the best agreement with the observations (confirmed by other modelling studies as well).
- (iv) A small improvement in the model performance was observed when the two-way nesting option was used.

3.2. March 2005. Accuracy verification at the FINO1 platform indicated that the WRF methodology developed for the stable period (16–18 March 2005) results in more accurate wind simulation than any other simulation in the study of Muñoz-Esparza et al. [8], though there are similarities between the studies in terms of findings. But, is the concluded WRF model configuration appropriate for other stability conditions (e.g., neutral and unstable) and for longer time periods during which all atmospheric stability conditions are observed?

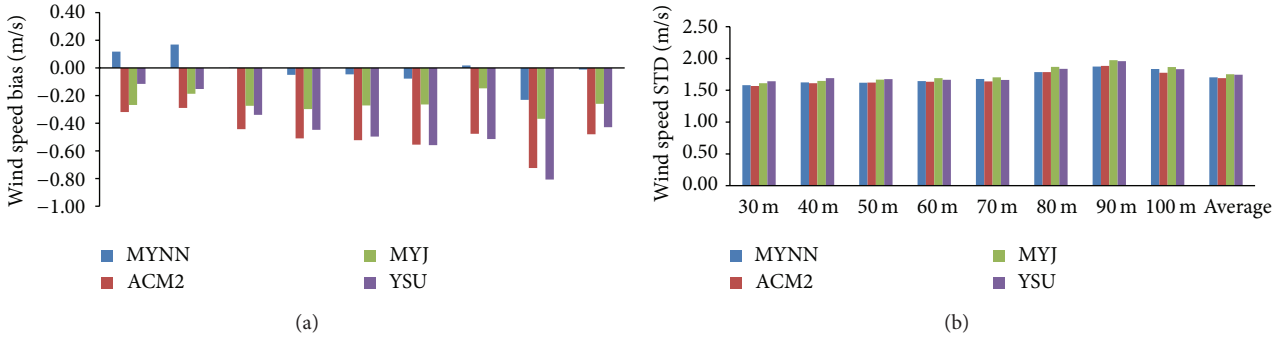


FIGURE 6: Monthly (March 2005) bias and standard deviation for wind speed at 8 vertical levels (30–100 m) and their average for the four PBL runs (YSU, MYJ, ACM2, and MYNN).

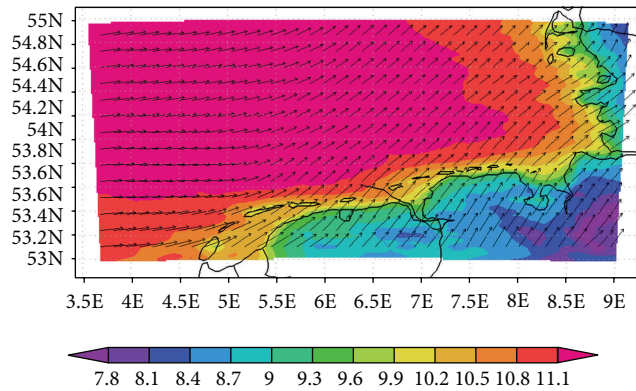


FIGURE 7: Average wind speed (m/s) and wind direction at 100 m height over the 3 km WRF modelling domain during March 2005 when the MYNN PBL scheme was selected.

To answer this question, the WRF model is validated in this section for the whole of March 2005 in which neutral, unstable, and stable atmospheric conditions are observed. To determine the atmospheric stability at the FINO1 met mast for March 2005, the Richardson number was calculated. It was found out that 35% of the time during March 2005 stable atmospheric conditions were dominant at the FINO1 offshore platform, while 65% of the time unstable and neutral conditions were observed.

3.2.1. Sensitivity to PBL Schemes. The WRF model is tested with the same four PBL schemes (YSU, MYJ, ACM2, and MYNN) used for the stable scenario. The monthly bias and standard deviation for each height of the FINO1 offshore platform is given in Figure 6 for each PBL run. In Figure 6, we can clearly observe that the MYNN PBL run gives the lowest bias at all vertical heights and the second lowest standard deviation. The biases of the YSU and ACM2 PBL schemes tend to increase as the height increases. As before for the stable case study, we concluded that the MYNN scheme is the one that yields to the highest degree of correctness with the FINO1 observational data. In particular, the MYNN scheme resulted in average over all the heights in 0.01 m/s lower wind speeds, STD of 1.71 m/s, and very high correlation coefficient equal to 0.93 (see Table 9).

TABLE 9: For March 2005, statistical metrics (ME in m/s, STD of the ME in m/s, and *R*) for wind speed [averaged over all the heights: 30 to 100 m]), so as to evaluate the performance of four PBL schemes (YSU, MYJ, ACM2, and MYNN) in the WRF model.

PBL	YSU	MYJ	ACM2	MYNN
ME (m/s)	-0.43	-0.26	-0.48	-0.01
STD (m/s)	1.75	1.75	1.69	1.71
<i>R</i>	0.92	0.92	0.92	0.93

In Figure 7, a map plot of the average 100 m wind speed and wind direction, as these were simulated during March 2005 from the MYNN PBL run over the 3 km WRF modelling domain, is provided. At the FINO1 mast (latitude: 54.0°N and longitude: 6.35°E) and the areas nearby the platform over the North Sea, the WRF model simulated hub height-wind speeds of the order of 11.2 m/s and westerly to southwesterly direction. In Figure 8, the wind roses are shown for March 2005 from both the FINO1 observations and all the WRF PBL simulations. It seems that the model in every PBL simulation overestimates the occurrence of wind speed in the range 12–16 m/s and results in a small veering of the winds in the clockwise direction between 0° and 180°.

3.2.2. Error Analysis and Q-Q Plots. In Figure 9, the Q-Q plots of the 100 m wind speed for March 2005 display a quantile-quantile plot of two samples: modelled versus observed. Each blue point in the Q-Q plots corresponds to one of the quantiles of the distribution the modelled wind follows and is plotted against the same quantile of the FINO1 observations' distribution. If the samples do come from the same distribution, the plot will be linear and the blue points will lie on the 45° line $y = x$.

As can be seen in Figure 9, the two distributions (the one modelled with the MYNN PBL scheme versus the observed one at FINO1) being compared are almost identical. The blue points in the Q-Q plot are closely following the 45° line $y = x$ with high correlation coefficient equal to 0.93 (see Table 9). The hourly observed and modelled wind speeds for March 2005 follow the Weibull distribution and upon closer inspection of Figure 10 the Weibull distribution resulted from the MYNN PBL run is the one that fits very

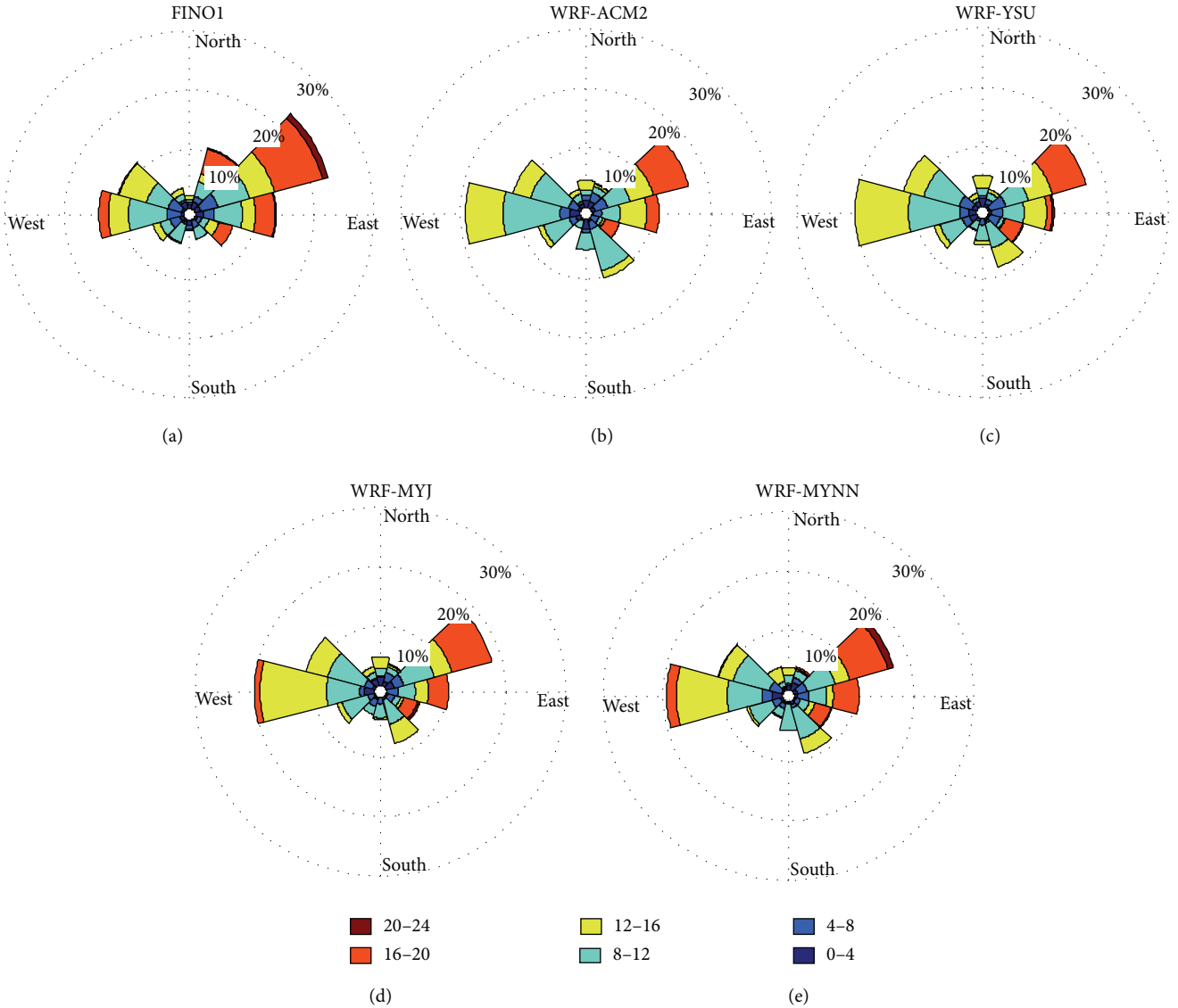


FIGURE 8: Wind roses based on March 2005 data from the FINO1 measurements and the WRF PBL runs (ACM2, YSU, MYJ, and MYNN) at 100 m height.

well with the FINO1 observed distribution at the 100 m height. In particular, the shape and scale parameters of the Weibull distribution, as these were calculated with the FINO1 measurements, were 2.51 and 12.74, respectively. The shape parameter modelled by the WRF model varied from 2.20 to 2.85 and the scale parameter ranged from 11.41 to 12.51 for the different PBL schemes used. However, only the MYNN PBL scheme resulted in shape and scale parameters closer to the one observed at the offshore platform (see Figure 10).

In order to further understand the performance of the WRF model and show the variation of the model results, in this section an error analysis is also performed. In general, the errors are assumed to follow normal distributions about their mean value and so the standard deviation is the measurement of the uncertainty. If it turns out that the random errors in the process are not normally distributed, then any inferences made about the process may be incorrect. In Figure 9, we

provide a normal probability plot of the ME of the 100 m wind speed. The plot includes a reference line indicating that the ME of the wind speed (blue points) closely follows the normal distribution. Figure 9 also shows a histogram of the wind speed mean error. In the *y*-axis of this histogram we have the number of records with a particular velocity error. The blue bars of the histogram show the relative frequency with which each wind speed error (which is shown along the *x*-axis) occurs. Clearly the ME follows the normal distribution and the mean is very close to zero, which is an indication that the mean error is unbiased.

4. Conclusions

The main goals of the present study were to achieve a better understanding of the offshore wind conditions, to accurately

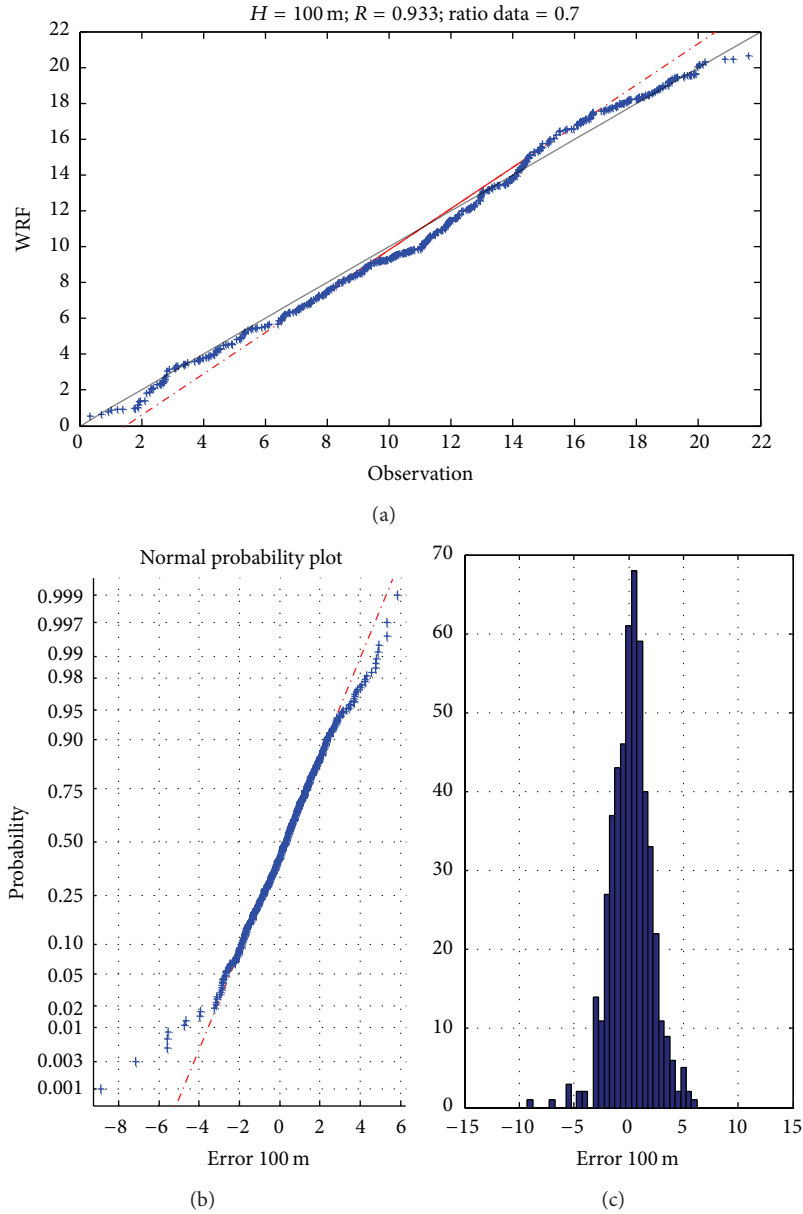


FIGURE 9: (a) Q-Q plot: the WRF MYNN PBL run (y-axis) against the FINO1 100 m wind speed distribution (x-axis). (b) Normal distribution against the 100 m wind speed ME and (c) histogram of the wind speed ME.

simulate the wind flow and atmospheric stability occurring offshore over the North Sea, and to develop a mesoscale modelling approach that could be used for more accurate WRA. In order to achieve all these goals, this paper examined the sensitivity of the performance of the WRF model to the use of different initial and boundary conditions, horizontal resolutions, and PBL schemes at the FINO1 offshore platform.

The WRF model methodology developed in this study appeared to be a very valuable tool for the determination of the offshore wind and stability conditions in the North Sea. It resulted in more accurate wind speed fields than the one simulated in previous studies, though there were similar findings. It was concluded that the mesoscale models must be adaptive in order to increase their accuracy. For example,

the atmospheric stability on the MABL (especially the stable atmospheric conditions), the topographic features in order to adjust the horizontal resolution accordingly, and the input datasets are needed to be taken into account.

It was concluded that the 3 km spacing is an optimal horizontal resolution for making precise offshore wind resource maps. Also, using the ERA-Interim reanalysis data instead of the NCEP FNL data allows us to reduce the bias between simulated and measured winds. Finally, it was found that changing PBL schemes has a strong impact on the model results. In particular, for March 2005 the MYNN PBL run yields in the best agreement with the observations with 0.01 m/s bias, standard deviation of 1.71 m/s, and correlation of 0.93 (averaged over all the vertical levels).

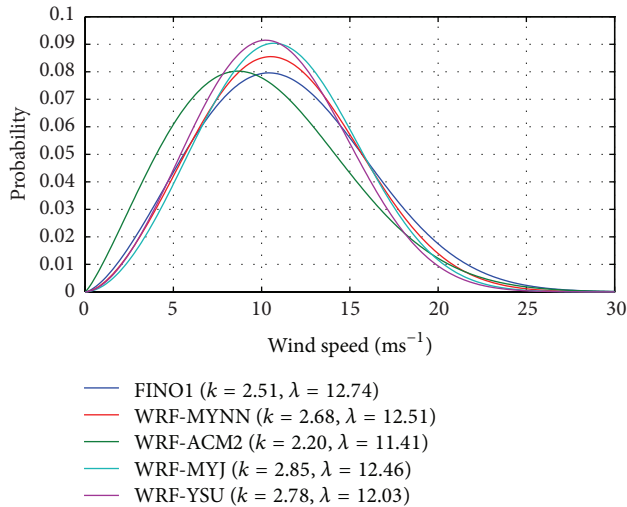


FIGURE 10: Weibull distribution based on March 2005 data from the FINO1 measurements and the WRF PBL runs (ACM2, YSU, MYJ, and MYNN) at 100 m height.

In future studies, in order to increase the reliability of the wind simulations and forecasting, it is necessary to expand the simulation period as long as possible.

Conflict of Interests

The authors declare that there is no conflict of interests regarding the publication of this paper.

References

- [1] O. Krogsæter, J. Reuder, and G. Hauge, "WRF and the marine planetary boundary layer," in *EWEA*, pp. 1–6, Brussels, Belgium, 2011.
- [2] A. C. Fitch, J. B. Olson, J. K. Lundquist et al., "Local and Mesoscale Impacts of Wind Farms as Parameterized in a Mesoscale NWP Model," *Monthly Weather Review*, vol. 140, no. 9, pp. 3017–3038, 2012.
- [3] O. Krogsæter, "One year modelling and observations of the Marine Atmospheric Boundary Layer (MABL)," in *NORCOWE*, pp. 10–13, 2011.
- [4] M. Brower, J. W. Zack, B. Bailey, M. N. Schwartz, and D. L. Elliott, "Mesoscale modelling as a tool for wind resource assessment and mapping," in *Proceedings of the 14th Conference on Applied Climatology*, pp. 1–7, American Meteorological Society, 2004.
- [5] Y.-M. Saint-Drenan, S. Hagemann, L. Bernhard, and J. Tambke, "Uncertainty in the vertical extrapolation of the wind speed due to the measurement accuracy of the temperature difference," in *European Wind Energy Conference & Exhibition (EWEC '09)*, pp. 1–5, Marseille, France, March 2009.
- [6] B. Cañadillas, D. Muñoz-esparza, and T. Neumann, "Fluxes estimation and the derivation of the atmospheric stability at the offshore mast FINO1," in *EWEA Offshore*, pp. 1–10, Amsterdam, The Netherlands, 2011.
- [7] D. Muñoz-Esparza and B. Cañadillas, "Forecasting the Diabatic Offshore Wind Profile at FINO1 with the WRF Mesoscale Model," *DEWI Magazine*, vol. 40, pp. 73–79, 2012.
- [8] D. Muñoz-Esparza, J. Beeck Van, and B. Cañadillas, "Impact of turbulence modeling on the performance of WRF model for offshore short-term wind energy applications," in *Proceedings of the 13th International Conference on Wind Engineering*, pp. 1–8, 2011.
- [9] M. Garcia-Diez, J. Fernandez, L. Fita, and C. Yague, "Seasonal dependence of WRF model biases and sensitivity to PBL schemes over Europe," *Quarterly Journal of Royal Meteorological Society*, vol. 139, pp. 501–514, 2013.
- [10] W. Skamarock, J. Klemp, J. Dudhia et al., "A description of the advanced research WRF version 3," NCAR Technical Note 475+STR, 2008.
- [11] K. Sušelj and A. Sood, "Improving the Mellor-Yamada-Janjić Parameterization for wind conditions in the marine planetary boundary layer," *Boundary-Layer Meteorology*, vol. 136, no. 2, pp. 301–324, 2010.
- [12] F. Kinder, "Meteorological conditions at FINO1 in the vicinity of Alpha Ventus," in *RAVE Conference*, Bremerhaven, Germany, 2012.
- [13] J. M. Potts, "Basic concepts," in *Forecast Verification: A Practitioner's Guide in Atmospheric Science*, I. T. Jolliffe and D. B. Stephenson, Eds., pp. 11–29, John Wiley & Sons, New York, NY, USA, 2nd edition, 2011.
- [14] E. M. Giannakopoulou and R. Toumi, "The Persian Gulf summertime low-level jet over sloping terrain," *Quarterly Journal of the Royal Meteorological Society*, vol. 138, no. 662, pp. 145–157, 2012.
- [15] E. M. Giannakopoulou and R. Toumi, "Impacts of the Nile Delta land-use on the local climate," *Atmospheric Science Letters*, vol. 13, no. 3, pp. 208–215, 2012.
- [16] D. P. Dee, S. M. Uppala, A. J. Simmons et al., "The ERA-Interim reanalysis: configuration and performance of the data assimilation system," *Quarterly Journal of the Royal Meteorological Society*, vol. 137, no. 656, pp. 553–597, 2011.
- [17] P. Liu, A. P. Tsimpidi, Y. Hu, B. Stone, A. G. Russell, and A. Nenes, "Differences between downscaling with spectral and grid nudging using WRF," *Atmospheric Chemistry and Physics*, vol. 12, no. 8, pp. 3601–3610, 2012.
- [18] G. L. Mellor and T. Yamada, "Development of a turbulence closure model for geophysical fluid problems," *Reviews of Geophysics & Space Physics*, vol. 20, no. 4, pp. 851–875, 1982.
- [19] M. Nakanishi and H. Niino, "An improved Mellor-Yamada Level-3 model with condensation physics: its design and verification," *Boundary-Layer Meteorology*, vol. 112, no. 1, pp. 1–31, 2004.
- [20] S.-Y. Hong, Y. Noh, and J. Dudhia, "A new vertical diffusion package with an explicit treatment of entrainment processes," *Monthly Weather Review*, vol. 134, no. 9, pp. 2318–2341, 2006.
- [21] J. E. Pleim, "A combined local and nonlocal closure model for the atmospheric boundary layer. Part II: application and evaluation in a mesoscale meteorological model," *Journal of Applied Meteorology and Climatology*, vol. 46, no. 9, pp. 1396–1409, 2007.
- [22] B. Storm, J. Dudhia, S. Basu, A. Swift, and I. Giammanco, "Evaluation of the weather research and forecasting model on forecasting low-level jets: implications for wind energy," *Wind Energy*, vol. 12, no. 1, pp. 81–90, 2009.
- [23] J. L. Woodward, "Appendix A: atmospheric stability classification schemes," in *Estimating the Flammable Mass of a Vapor Cloud*, pp. 209–212, American I. Wiley Online Library, 1998.

- [24] L. Fita, J. Fernández, M. García-Díez, and M. J. Gutiérrez, “SeaWind project: analysing the sensitivity on horizontal and vertical resolution on WRF simulations,” in *Proceedings of the 2nd Meeting on Meteorology and Climatology of the Western Mediterranean (JMCMO '10)*, 2010.
- [25] C. Talbot, E. Bou-Zeid, and J. Smith, “Nested mesoscale large-Eddy simulations with WRF: performance in real test cases,” *Journal of Hydrometeorology*, vol. 13, no. 5, pp. 1421–1441, 2012.
- [26] S. Shimada, T. Ohsawa, T. Kobayashi, G. Steinfeld, J. Tambke, and D. Heinemann, “Comparison of offshore wind speed profiles simulated by six PBL schemes in the WRF model,” in *Proceedings of the 1st International Conference Energy & Meteorology Weather & Climate for the Energy Industry (IECM '11)*, pp. 1–11, November 2011.
- [27] K. E. Taylor, “Summarizing multiple aspects of model performance in a single diagram,” *Journal of Geophysical Research D*, vol. 106, no. 7, pp. 7183–7192, 2001.

Research Article

A Subgrid Parameterization for Wind Turbines in Weather Prediction Models with an Application to Wind Resource Limits

B. H. Fiedler¹ and A. S. Adams²

¹ School of Meteorology, University of Oklahoma, Norman, OK 73072-7307, USA

² Department of Geography and Earth Sciences, University of North Carolina at Charlotte, Charlotte, NC 28223-0001, USA

Correspondence should be addressed to B. H. Fiedler; bfiedler@ou.edu

Received 10 September 2013; Accepted 22 December 2013; Published 9 January 2014

Academic Editor: Huei-Ping Huang

Copyright © 2014 B. H. Fiedler and A. S. Adams. This is an open access article distributed under the Creative Commons Attribution License, which permits unrestricted use, distribution, and reproduction in any medium, provided the original work is properly cited.

A subgrid parameterization is offered for representing wind turbines in weather prediction models. The parameterization models the drag and mixing the turbines cause in the atmosphere, as well as the electrical power production the wind causes in the wind turbines. The documentation of the parameterization is complete; it does not require knowledge of proprietary data of wind turbine characteristics. The parameterization is applied to a study of wind resource limits in a hypothetical giant wind farm. The simulated production density was found not to exceed 1 W m^{-2} , peaking at a deployed capacity density of 5 W m^{-2} and decreasing slightly as capacity density increased to 20 W m^{-2} .

1. Introduction

Wind power production in numerical weather prediction models can be either inert or active. In the inert type, the wind speed forecasted for a turbine location can be extracted from the model and used to calculate wind power production, with no impact of the turbines on the weather prediction [1]. In the active type, this impact is included, specifically the drag and turbulence enhancement of the wind turbine acting on the atmosphere [2]. In this paper we offer some details of a wind turbine parameterization appropriate for large wind farms, with many turbines within a grid cell. This paper refines the wind turbine parameterization in [2, 3], effectively offering a simplified and documented alternative to what appeared in WRFv3.3 [4, 5]. Being subgrid, wakes are not explicitly simulated, but rather the momentum loss is immediately diffused across the breadth of the grid cell. The parameterization is adaptable to typical wind turbine characteristics. The giant wind farm of [3] is revisited for the purpose of studying the practical limit to wind power extraction from the atmosphere. Whereas [3] examined the much more subtle effect of the wind farm on precipitation climate statistics, the current study is more straightforward and does not require multidecadal simulations. The simulations use WRFv3.1 with

the MYJ boundary layer scheme and 30 km horizontal grid spacing. The wind turbine parameterization adds elevated drag and production of turbulent kinetic energy to the MYJ scheme.

If a horizontal wind vector \vec{V} is known at the height of wind turbine (in practice, meaning that a suitable average wind vector is known), then the power produced is

$$P = C_f(V) P_{\max}, \quad (1)$$

where C_f is the capacity coefficient and P_{\max} is the rated power output for the particular wind turbine. In the simulations, we focus on $P_{\max} = 2 \text{ MW}$ and $P_{\max} = 8 \text{ MW}$, which roughly brackets the range of potential installations. C_f is constrained by both laws of nature and engineering design. For $V < V_{\text{in}}$, the turbine blades do not rotate, so $C_f = 0$. Likewise, for $V > V_{\text{out}}$ the turbine rotation is halted to avoid damage, and $C_f = 0$. As V increases past V_{in} , power production rises rapidly, but by engineering design is brought to a broad plateau of P_{\max} , by mechanical adjustment of the turbine blade pitch angle [6].

Figure 1 shows a typical $C_f(V)$ offered by this parameterization. Figure 1 also shows the two other dimensionless coefficients that must be known, if the impact of the turbine

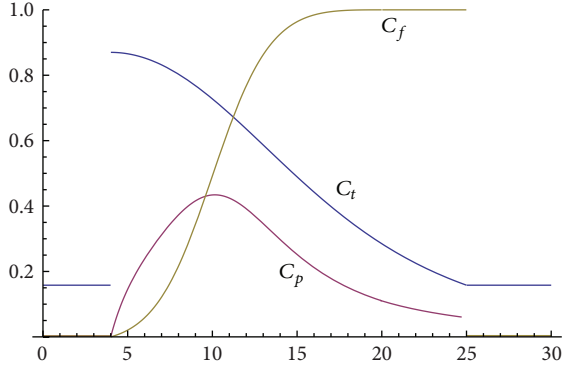


FIGURE 1: The capacity factor C_f , the thrust coefficient C_t , and power coefficient C_p for the wind turbine parameterization configured to model the Bonus Energy A/S 2 MW wind turbine. $V_{in} = 4$, $V_{out} = 25$, $\alpha = 0.3$, $\beta = 1.18 \times 10^{-5}$, $V_0 = 10$, $C_{ts} = 0.158$, and $C_{tp} = 0.87$.

on the atmosphere is to be calculated. The aerodynamical basis of (1) determines those impacts. From elementary physics, the available power of wind impinging on the rotor cross-sectional area A of the turbine is

$$\frac{1}{2}\rho V^3 A, \quad (2)$$

where ρ is the density of the air. The ratio of P to the available power is the power coefficient C_p :

$$C_p = \frac{C_f P_{max}}{(1/2)\rho V^3 A}. \quad (3)$$

So (1) can be written as

$$P = C_p(V) \frac{1}{2}\rho V^3 A. \quad (4)$$

Though (4) provides the identical calculation of power production as (1), knowledge of C_p will have another important purpose in calculating the production of turbulent kinetic energy.

The drag force \vec{F} on an object presenting cross-sectional area A to a uniform stream of fluid with velocity \vec{V} is conventionally modeled in terms of a shape-dependent drag coefficient C_d . In the language of wind turbine modeling, the drag coefficient is named the thrust coefficient C_t :

$$\vec{F} = C_t(V) \frac{1}{2}\rho V \vec{V} A. \quad (5)$$

At large Reynolds number, C_t is predominantly shape dependent. For example, there are many references giving values such as for a flat plate $C_t = 1.28$ and for a sphere $C_t = 0.47$. The drag force for rotating turbine blades is much greater than a calculation based on stationary blades and using just the area presented by the blades. The drag force of the wind turbine is characterized in terms of the disk swept out, $A = \pi R^2$, where R is blade length. For the Bonus Energy A/S 2.0 MW, C_t peaks at approximately $C_t = 0.88$ [2]. Presumably this cited value of C_t includes the drag of the tower as well,

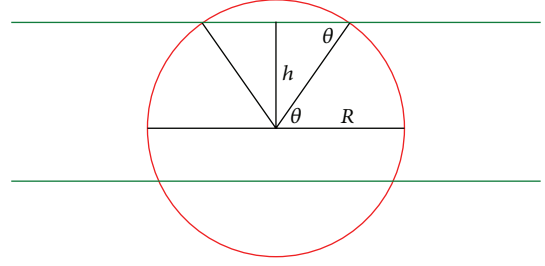


FIGURE 2: Calculating the fraction of the area of the rotor circle (red) contained between two pressure levels (green). In this example, the hub of the rotor lies between the pressure levels. The area above the hub is sum of two triangles and two sectors. The area of the triangles sum to $h\sqrt{R^2 - h^2}$. The area of the two sectors sum to $R^2 \sin^{-1}(h/R)$. In this example, the area below the hub makes a similar positive contribution. If the hub is not between the layers, the total area is given by the subtraction of two areas calculated from the hub. Likewise, if $h > R$, then h is replaced by R in the calculation.

but in this parameterization the drag force is modeled as occurring within the area of the rotor.

The drag force of the wind turbine removes momentum from the atmosphere and transfers it to the Earth. But with the Earth having a large mass, the drag force transmitted to Earth, via the tower, does not do significant work on the Earth, meaning that the loss of energy from the mean wind goes into power production and turbulent kinetic energy, rather than into kinetic energy of the Earth [4].

The force of the turbine on the atmosphere is opposite to that of (5), so the rate of work (power) P_a on the atmosphere is $-\vec{F} \cdot \vec{V}$:

$$P_a = -C_t \frac{1}{2}\rho V^3 A. \quad (6)$$

By our principle of strict energy conservation

$$P + P_a + P_{tke} = 0, \quad (7)$$

so

$$P_{tke} = \frac{1}{2}\rho V^3 A (C_t - C_p). \quad (8)$$

Most numerical weather prediction models employ a force per mass at a grid point, within a grid volume. The drag force in (5) would need to be normalized appropriately, by the total mass of air in the grid volume. Similarly, a normalization is required when (8) is used to predict turbulent kinetic energy and added to the other source terms in the prediction for turbulent kinetic energy.

Here we take A as the only portion of the multiple wind turbine areas that are within the heights bounding a grid volume (Figure 2). This introduces some unrealism, as it allows a wind turbine to be modeled as having different rotation speeds and different C_f at various heights. The normalization procedure of the previous paragraph means that the rotor area per grid volume (an area density with units of inverse length) is the quantity needed for computation. In a staggered grid model, the heights of the prediction

of horizontal wind may lie between the levels for the prediction of vertical velocity, the levels of which define the vertical bounds to the grid volume for horizontal velocity.

2. Functions for $C_f(V)$ and $C_t(V)$

For $C_f(V)$, we employ a soft-clip function, which allows $C_f(V)$ to come to a plateau without a sharp “knee point.” Note that [4] does not provide this soft-clip feature and [2, 3] do not have a monotonic C_f . The soft-clip function that we employ is computationally efficient and provides a very close approximation to $(1 + \tanh(x))/2$:

$$s(x) = \begin{cases} 0, & \text{if } x \leq -3 \\ 1, & \text{if } x \geq 3 \\ \frac{1}{2} \left(1 + \frac{27x + x^3}{27 + 9x^2} \right), & \text{otherwise.} \end{cases} \quad (9)$$

Here $x = \alpha(V - V_0)$, where V_0 controls the center point of C_f and α controls the slope of the transition. Adjusting the center point and slope to approximate the characteristics of the Bonus wind turbine is elementary. Slightly more complicated is to require C_p to be exactly zero for $V < V_{in}$, which may require employing a shift of $s(x)$ to bury part of it below the x -axis. Let

$$\delta \equiv s[\alpha(V_{in} - V_0)]. \quad (10)$$

Thus

$$C_f(V) = \begin{cases} 0, & \text{if } V \leq V_{in} \\ 0, & \text{if } V \geq V_{out} \\ \frac{1}{1-\delta} \{s[\alpha(V - V_0)] - \delta\}, & \text{otherwise.} \end{cases} \quad (11)$$

As the blades of a wind turbine are adjusted, to reduce C_p so that the maximum in C_f does not exceed 1, the thrust coefficient is also reduced. We find the following fit satisfactory:

$$C_t(V) = \begin{cases} C_{ts}, & \text{if } V \leq V_{in} \\ C_{ts}, & \text{if } V \geq V_{out} \\ C_{tp} \frac{1}{1 + .005(V - V_{in})^2 + \beta(V - V_{in})^4}, & \text{otherwise.} \end{cases} \quad (12)$$

Figure 1 lists the values of the parameters used for the Bonus 2 MW turbine. We employ a value for β that makes $C_t(V_{out}) = C_{ts}$, so there is no discontinuity in C_t at V_{out} . Other choices are possible.

3. Application to Wind Resource Limits

Textbooks in atmospheric science cite the typical midlatitude pressure gradient force (per mass) to be 10^{-3} m s^{-2} and the typical horizontal velocity scale to be 10 m s^{-1} , with about

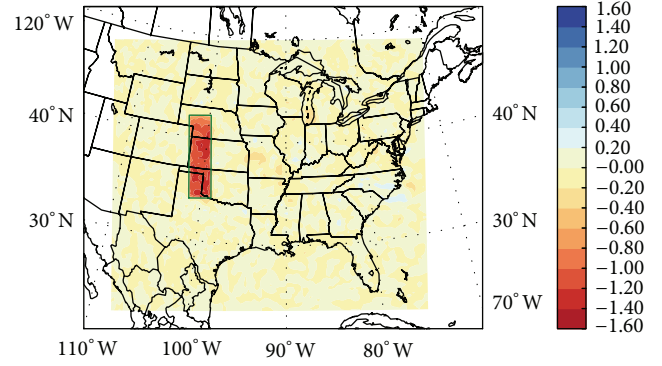


FIGURE 3: The wind farm is within the green rectangle. The average wind difference at 102 m between the simulation with 2.5 W m^{-2} of 2 MW turbines minus the simulation without turbines is shown.

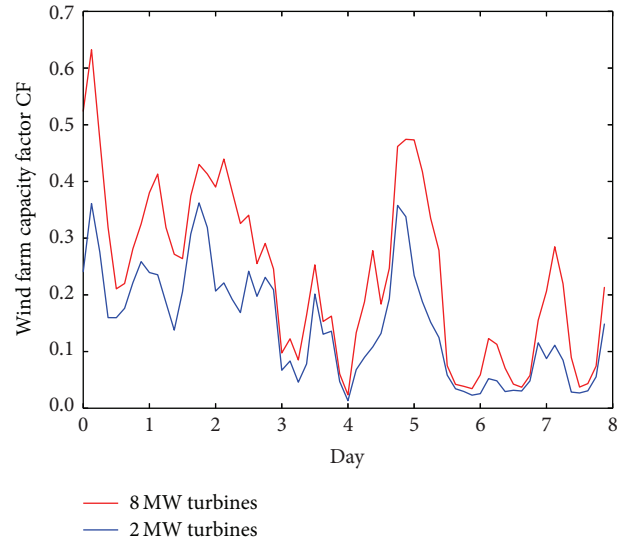


FIGURE 4: The average wind farm capacity factor CF for two particular deployments of $CD = 2.5 \text{ W m}^{-2}$, as a function of time. These plots show the details behind the points for $CD = 2.5 \text{ W m}^{-2}$ in Figures 7 and 8. The average production with 8 MW turbines is 106 GW. The average production with 2 MW turbines is 66 GW.

1/10 of that being cross-isobaric. Only the cross-isobaric component is capable of internally renewing kinetic energy that has been removed by the wind farm. In the boundary layer, a larger fraction of the wind vector could be cross-isobaric, but the magnitude of the vector could be less. So if we accept 1 m s^{-1} as the typical magnitude of cross-isobaric flow, the rate of kinetic energy production within the wind farm would be 1 W m^{-2} per kilometer of depth of the extraction (assuming a density of $\rho = 1 \text{ kg m}^{-3}$).

Kinetic energy also enters the wind farm from the side. If a giant wind farm of horizontal area $L \times L$ is extracting wind from a layer of depth H (where H could be the depth of the atmospheric boundary layer, rather than height to the top of the wind turbine), then (2) can be used to calculate the power advected into the wind farm presenting a side area of

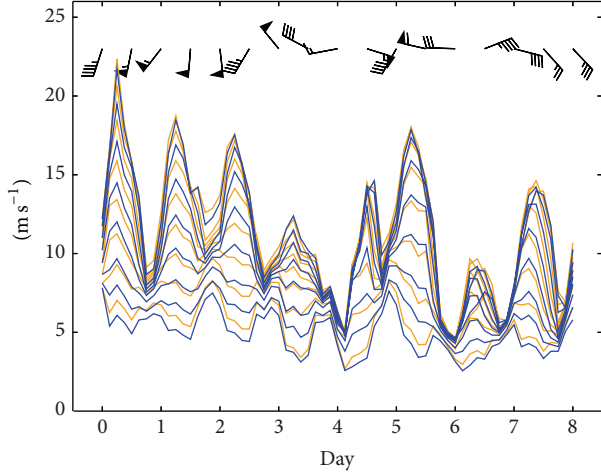


FIGURE 5: Average horizontal wind speed at the lowest 8 grid wind levels of 15, 52, 102, 165, 245, 345, 466, and 648 meters above ground. Orange is without wind turbines. Blue is with 2 MW wind turbines deployed at $CD = 2.5 \text{ W m}^{-2}$ capacity. Top of the rotor is at 98 m (careful counting shows that blue curve is below the corresponding orange curve). The wind barbs represent the horizontal wind direction and magnitude at 102 m at the center of the wind farm area, but without wind turbines. Half barbs are 1 m s^{-1} , full barbs 2 m s^{-1} , and flags 10 m s^{-1} . Days are ticked at 0 UTC, late afternoon at the wind farm, at which time the wind speed has become more well mixed across the boundary layer.

$A = H \times L$. This is power that can be potentially extracted over the area of the wind farm, giving a power density

$$\frac{1}{2}\rho V^3 \frac{HL}{L^2} = \frac{1}{2}\rho V^3 \frac{H}{L}. \quad (13)$$

For example, let us take $H = 1 \text{ km}$ and $L = 100 \text{ km}$. For $H/L = 0.01$ and $V = 5 \text{ m s}^{-1}$, that gives an upper limit to extraction of 0.625 W m^{-2} . Using $V = 10 \text{ m s}^{-1}$ instead gives 5 W m^{-2} . Note that a giant wind farm could have $H/L < 0.01$, and the bound on power that is extractable from the advection source would correspondingly be less. Thus as H/L becomes small, renewing of the wind resource by the pressure gradient becomes more important.

In the above estimates, what value should be used for H ? Also, what is the contribution of transport through the top of the wind farm? We also need to recognize that as the power extraction approaches the upper limit, that would imply that V would be decreasing as the wind farm is traversed. The continuity equation would thus require upward advection of energy out of the top of the wind farm. All these considerations imply that a more refined estimate of the limits to power extraction at a site will require details about the wind climate, including boundary layer mixing, as well as the use of a numerical weather prediction model.

Here we demonstrate an application of our wind farm parameterization with a modest extension to several such studies of limits to wind farm resources [2, 4, 7], namely, allowing for all sizes of wind turbines to have the characteristics of Figure 1. The parameterization is used to investigate

the relative effect of deploying the capacity density as 8 MW turbines, twice the size of 2 MW turbines.

The wind farm location is as in [3], with an area of $182,700 \text{ km}^2$ (Figure 3). In [3], 2 MW wind turbines were situated with turbine density of 1.25 km^{-2} , giving the giant wind farm a capacity of 457 GW and a capacity density of 2.5 W m^{-2} . The 2 MW wind turbines had a hub height of 60 m and a rotor radius of 38 m. Here we experiment with both 2 MW and 8 MW turbines, deployed with capacity density ranging from 0.625 W m^{-2} to 20 W m^{-2} . The 8 MW wind turbines are simply double in height and radius of the 2 MW turbines. The C_f , C_t , and C_p curves for both models are as in Figure 1. The study shown here is much simpler than [3], and examines only the effect of the wind farm on wind characteristics within the wind farm, as well as the power production by the wind farm.

The 8 days from 0 UTC April 23, 1948 to 0 UTC May 1, 1948 were convenient for this study. The National Renewable Energy Laboratory displays the annual average wind speed at 80 m to range between 7.0 m s^{-1} and 9.0 m s^{-1} in the modeled wind farm area. The model, without wind turbines, has an average wind speed of 7.0 m s^{-1} and 8.1 m s^{-1} at 52 m and 102 m, respectively, during the 8 days of the simulation.

3.1. 8 MW versus 2 MW Deployment. Here we highlight a particular comparison between deploying the 457 GW as either 228,375 2 MW turbines or as 58,656 8 MW turbines. In the analysis of power production, the average C_f experienced over the entire farm is denoted by CF (C_f is an engineering design parameter and CF is an experimental result). Though the capacity density (CD) is the same, the production density (PD) with the 8 MW deployment is 60% greater (Figure 4). A naive estimate might have anticipated an increase greater than 100%, using reasoning that the layer being mined for power is twice as deep, with the upper part having stronger winds. That sort of estimate is not realized.

Figures 5 and 6 show that the extraction (as indicated by wind speed reduction) has become rather insignificant at height 648 m. But both the 8 MW and 2 MW turbines discernibly remove energy below 648 m. As expected, the taller 8 MW turbines extract more energy in the layer above the height of the smaller turbine. Estimating how much more effective the extraction is with taller turbines has required the benefit of a numerical simulation. The ability to make such an estimation is one of the main practical benefits of the parameterization.

3.2. Production Saturation. Here we summarize the investigation into power production across a broad range of wind farm characteristics. Conclusions are similar to [2, 4, 7, 8]: Figure 7 shows a limit to power extraction to be on the order of 1 W m^{-2} . Such knowledge obviously influences design characteristics of wind farms: whether to add more wind turbines to a farm, acquire more land and develop a larger farm, or develop another farm in a distant location. In our simulations, the drop in CF proceeds immediately from the lowest CD. This is because power production is very sensitive to changes in V in the vicinity of V_{in} , with C_f rising faster

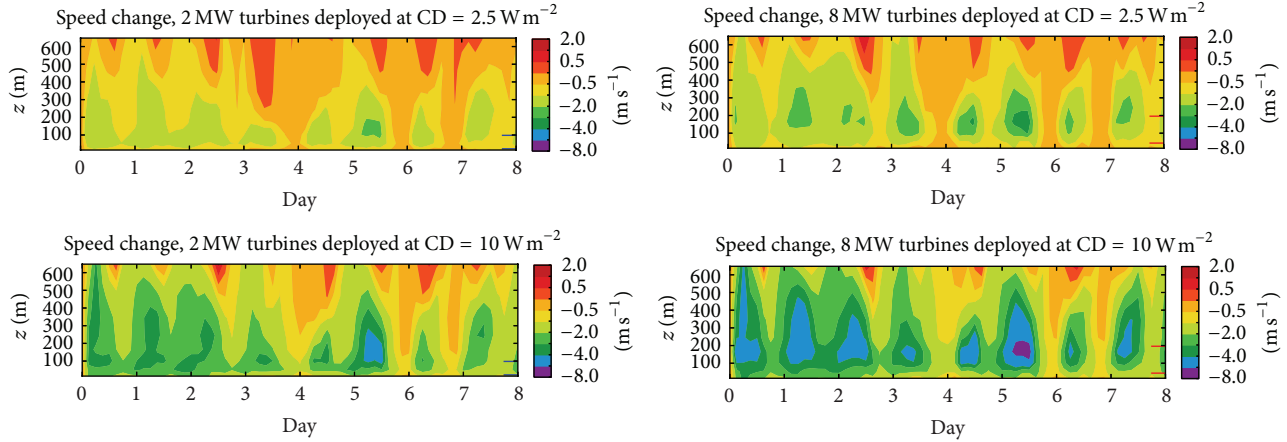


FIGURE 6: Area-averaged wind speed change that results from deploying wind turbines, as a function of height and time. The height of the top and bottom of the rotor are indicated by longer tick marks at the extreme right. The extent of the wind reduction above the tops of the turbines is indicative of power extraction from those layers, a complicated prediction requiring a numerical weather prediction model.

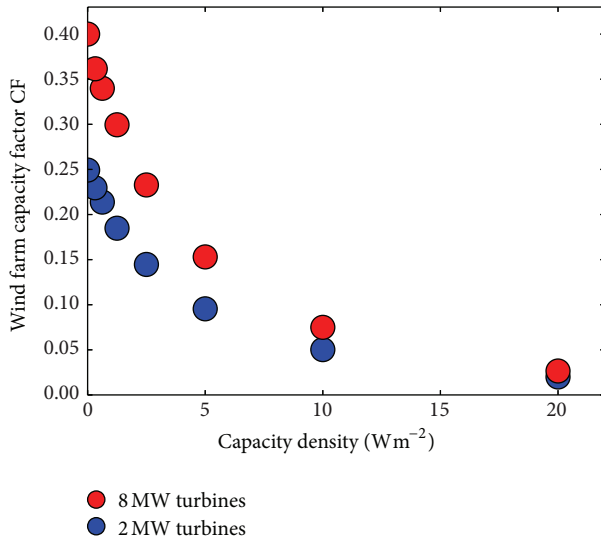


FIGURE 7: As in Figure 8, but average wind farm capacity factor CF for various deployments.

than V^3 wherever C_p is increasing with V . The opposite scenario could happen in a different wind climate. If V is consistently well into the range that produces $C_f(V) = 1$, there might be a significant decrease in V , but no drop in CF until CD exceeds a value greater than 1 W m^{-2} .

Consider increasing CD from 2.5 W m^{-2} , with 2 MW turbines, to 10 W m^{-2} by either quadrupling the area of the rotors or quadrupling the number of turbines. The two scenarios can be found within Figure 8. Increasing the rotor area density by a factor of 4 (redeploying as 8 MW turbines) increased PD by 2.07. Quadrupling the number of 2 MW turbines increased PD by a factor of 1.38. Since the increase in PD was significantly less than 4, we would say that the collective impact of the turbines on the power productivity of the winds is significant. Inspection of the wind difference

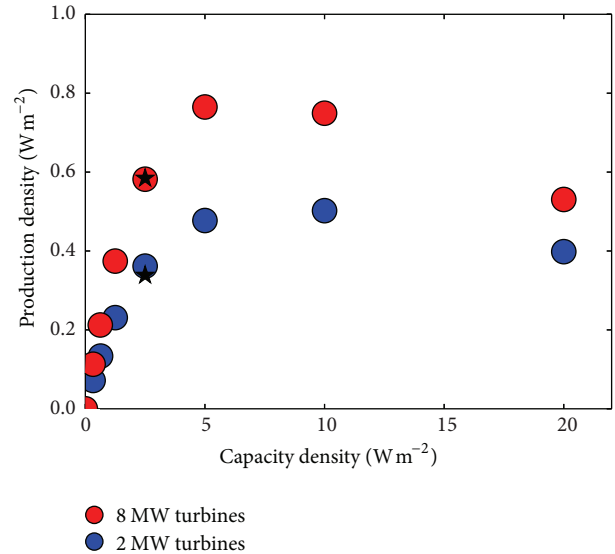


FIGURE 8: Average wind farm production density PD for various deployments. The two points marked with a star are for simulations repeated using twice the number of grid points within the depth of the boundary layer, as compared with the standard resolution. The simulations with standard resolution are indicated with a circle. The vertical positions of the grid points in the standard resolution are listed in Figure 5.

plots in Figure 6 shows wind being reduced above the tops of the turbines, evidently the effect of turbulent transport of momentum vertically in the atmosphere. This transport may be hard to estimate by means other than a detailed numerical model.

We note that Horns Rev 1, an established 20 km^2 wind farm in the North Sea, has been averaging $\text{PD} = 3.98 \text{ W m}^{-2}$ in the last 5 years [9]. This illustrates the importance of scale in understanding the production limitations of wind energy. As discussed in Section 3, the larger the horizontal extent of

the wind farm is, the less important the advection of kinetic energy is and the more important the pressure gradient force becomes in sustaining energy producing wind speeds within the wind farm. The Horns Rev 1 wind farm is small enough that H/L is approximately 0.2, thus explaining the observed PD.

4. Conclusions

When considering national and international energy portfolios, wind energy continues to become an important part of diversified energy portfolios. Though current wind farms are small enough in scale to have H/L ratios that allow advection of kinetic energy into the side of a wind farm to be an important power source, it is important to discern how that wind resource diminishes with larger wind farms. Future power needs could force the development of giant wind farms, with areas that are orders of magnitude larger than current farms. Furthermore, the development of many small wind farms in close proximity could have a resource limit similar to a giant wind farm.

Giant wind farms will need to be planned with an active type numerical weather prediction model, so as to get an accurate estimate of the wind power resource. For example, in our study, larger (taller) wind turbines produce a larger CF. The cost-effectiveness of deploying larger turbines will require an accurate prediction of this CF before a financial decision can be made.

Conflict of Interests

The authors declare that there is no conflict of interests regarding the publication of this paper.

References

- [1] J. S. Greene, M. Chatelain, M. Morrissey, and S. Stadler, "Projected future wind speed and wind power density trends over the western us high plains," *Atmospheric and Climate Sciences*, vol. 2, no. 1, pp. 32–40, 2012.
- [2] A. S. Adams and D. W. Keith, "Are global wind power resource estimates overstated?" *Environmental Research Letters*, vol. 8, no. 1, Article ID 015021, 2013.
- [3] B. H. Fiedler and M. S. Bukovsky, "The effect of a giant wind farm on precipitation in a regional climate model," *Environmental Research Letters*, vol. 6, no. 4, Article ID 045101, 2011.
- [4] A. C. Fitch, J. B. Olson, J. K. Lundquist et al., "Local and mesoscale impacts of wind farms as parameterized in a mesoscale nwp model," *Monthly Weather Review*, vol. 140, no. 9, pp. 3017–3038, 2012.
- [5] W. C. Skamarock and A. Coauthors, "description of the advanced research WRF version 3," Tech. Rep. NCAR/TN-4751STR, National Center for Atmospheric Research, 2008.
- [6] P. W. Carlin, A. S. Laxson, and E. B. Muljadi, "The history and state of the art of variable-speed wind turbine technology," *Wind Energy*, vol. 6, no. 2, pp. 129–159, 2003.
- [7] D. W. Keith, J. F. DeCarolis, D. C. Denkenberger et al., "The influence of large-scale wind power on global climate," *Proceedings of the National Academy of Sciences of the United States of America*, vol. 101, no. 46, pp. 16115–16120, 2004.
- [8] M. Z. Jacobson and C. L. Archer, "Saturation wind power potential and its implications for wind energy," *Proceedings of the National Academy of Sciences*, vol. 109, no. 39, pp. 15679–15684, 2012.
- [9] E. L. Petersen, I. Troen, H. E. Jrgensen, and J. Mann, "Are local wind power resources well estimated?" *Environmental Research Letters*, vol. 8, no. 1, Article ID 011005, 2013.